Spinterface in Metal/Organic Semiconductor Thin Films

By

PURBASHA SHARANGI

Enrolment No. PHYS11201604004

National Institute of Science Education and Research, Bhubaneswar

A thesis submitted to the

Board of Studies in Physical Sciences

In partial fulfillment of requirementsfor the Degree of

DOCTOR OF PHILOSOPHY

of

HOMI BHABHA NATIONAL INSTITUTE

November, 2021

Homi Bhaba National Institute

Recommendations of the Viva Voce Committee

As members of the Viva Voce Committee, we certify that we have read the dissertation prepared by Ms. Purbasha Sharangi entitled 'Spinterface in metal/organic semiconductor thin films' and recommend that it may be accepted as fulfilling the thesis requirement for the award of Degree of Doctor of Philosophy.

Chairman – Prof. Bedangadas Mohanty	28/03/2022
Guide / Convener – Dr. Subhankar Bedanta	28/03/2022
Examiner – Prof. Sourav Giri	28/03/2022
Member 1 – Dr. Ajaya Kumar Nayak	28/03/2022
Member 2 – Dr. Anamitra Mukherjee	28/03/2022
Member 3 – Dr. Debakanta Samal	28/03.22

Final approval and acceptance of this thesis is contingent upon the candidate's submission of the final copies of the thesis to HBNI.

I/We hereby certify that I/we have read this thesis prepared under my/our direction and recommend that it may be accepted as fulfilling the thesis requirement.

Date : 28.03.2022

Place : SPS, NISER, Jatni

28/03/2022

Guide

Dr. Subhankar Bedanta

STATEMENT BY AUTHOR

This dissertation has been submitted in partial fulfillment of requirements for an advanced degree at Homi Bhabha National Institute (HBNI) and is deposited in the Library to be made available to borrowers under rules of the HBNI.

Brief quotations from this dissertation are allowable without special permission, provided that accurate acknowledgement of source is made. Requests for permission for extended quotation from or reproduction of this manuscript in whole or in part may be granted by the Competent Authority of HBNI when in his or her judgment the proposed use of the material is in the interests of scholarship. In all other instances, however, permission must be obtained from the author.

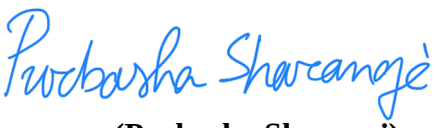

(Purbasha Sharangi)

DECLARATION

I, hereby declare that the investigation presented in the thesis has been carried out by me. The work is original and has not been submitted earlier as a whole or in part for a degree /diploma at this or any other Institution / University.

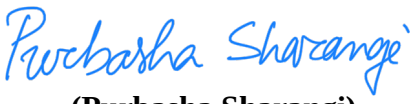

(Purbasha Sharangi)

List of Publications arising from the thesis

Journal

1. *****Magnetism at the interface of non-magnetic Cu and C_{60}, **P. Sharangi**, P. Gargiani, M. Valvidares and S. Bedanta, *Phys. Chem. Chem. Phys.* **23**, 6490-6495 (2021)

2. *Spinterface induced modification in magnetic properties in $Co_{40}Fe_{40}B_{20}$/Fullerene bilayers, P. Sharangi, E. Pandey, S. Mohanty, S. Nayak, and S. Bedanta, J. Phys. Chem. C 125, 45 (2021)

Communicated:

1. *Effect of Fullerene on anisotropy, domain size and relaxation in a perpendicularly magnetized Pt/Co/C_{60}/Pt system, **P. Sharangi**, A. Mukhopadhyaya, S. Mallika, Md. E. Ali and S. Bedanta (*arXiv:2012.12777*)
2. *Spin pumping and inverse spin Hall effect in CoFeB/C_{60} interface, **P. Sharangi,** B. B. Singh, S. Nayak, and S. Bedanta (*arXiv:2106.06829*)

Manuscript under preparation:

1. *Effect of spinterface on magnetization reversal and magnetic anisotropy in Co/Rubrene system **P. Sharangi,** S. Nayak, Md. Azharuddin, and S. Bedanta (*under preparation*)

***** : Publications related to the thesis

Others

1. Enhanced anisotropy and study of magnetization reversal in bilayer thin film, S. Mallik, **P. Sharangi**, B. Sahoo, S. Mattauch, T. Brückel, and S. Bedanta, Appl. Phys. Lett. **115**, 242405 (2019)
2. Strain engineered domain structure and their relaxation in perpendicularly magnetized Co/Pt deposited on flexible polyimide, E. Pandey, B. B. Singh, **P. Sharangi** and S. Bedanta, *Nano Express* **1**, 010037 (2020)
3. Electrodeposited Heusler alloy films with enhanced magneto-optical property, Md. R. Karim, D. Panda, A. Adhikari, **P. Sharangi**, P. Mandal, S. Ghosh, S. Bedanta, A. Barman, and I. Sarkar, *Mater. Today Commun*. **25**, 101678 (2020)
4. Ultrafast Spin Dynamics of Electrochemically Grown Heusler Alloy Films, Md. R. Karim, A. Adhikari, S. N. Panda, **P. Sharangi**, S. Kayal, G. Manna, P. S. A. Kumar, S. Bedanta, A. Barman, and I. Sarkar, *J. Phys. Chem. C* **125**, 10483–1049 (2021)

Purbasha Sharangi

(**Purbasha Sharangi**)

Dedicated to my beloved family

ACKNOWLEDGEMENTS

In this long journey of the PhD program the success and outcomes of this thesis work cannot be achieved without the fruitful help from many people. Firstly, I would like to express my sincere gratitude to my supervisor Dr. Subhankar Bedanta for his continuous help, support, guidance and encouragement throughout my PhD studies. I am extremely thankful to him for giving me the opportunity to work in an interesting topic and helping me to grow as a researcher. I would like to thank you from the bottom of my heart for your patience and remarkable suggestions on my manuscripts and thesis. I did learn a lot about the topic and developed my research thinking pattern from the fruitful discussions with him.

I would also like to thank the chairman of my thesis monitoring committee (TMC) Prof. Bedangadas Mohanty and rest of my TMC members Dr. Anamitra Mukherjee, Dr. Ajaya Kumar Nayak and Dr. Debakanta Samal for their constant evaluation, support and suggestions which helped me to have a better understanding about my research topic.

I would like to acknowledge NISER, DAE, DST Govt. of India and CIS, NISER for providing me the financial support and infrastructure to carry out my research work. I would also like to thank NFFA Europe for funding the synchrotron and neutron measurements.

I would like to thank all my lab members for their valuable discussion and constant cooperation. I am always be indebted to my dada Dr. Sougata Mallik and didi Dr. Srijani Mallik for their constant support and helping me in learning different instruments. My special thanks to Srijani di for her help to learn the basics of organic spintronics. I would like to thank Dr. Thiruvengadam Vijayabaskaran for helping me in learning cryogenic systems. I would also like to thank Sagarika di, Esita, brindaban, Pushpendra, Koustuv, Shakti and Abhisek for their help during measurements. My sincere thanks to Shakti, Dr. Tapas Ghosh and Pushpendra for their help in TEM measurements. I would also sincerely thank Dr. Braj Bhusan Singh, INSPIRE

faculty, NISER, Bhubaneswar for his fruitful discussions. I would like to thank Niru di, Antarjami bhaiya Minaxi di, Azhar, Swayang, Swapna, Bikash, Biswajit, Aroop and Anupama for their humble scientific nature.

I would sincerely thank our collaborator Dr. Ehesan Ali and Mr. Aritra Mukhopadhyay from INST, Mohali for their help in DFT calculations in Pt/Co/C_{60}/Pt perpendicularly magnetized system. I am grateful to Dr. Pierluigi Gargiani and Prof. Manuel Valvidares for their help in XMCD experiments. I would also like to acknowledge Dr. Amir Syed Mohd. and Dr. Alexandrous Koutsioubas for helping in neutron experiment.

I am thankful and fortunate enough to get constant encouragement and support from my teachers Dr. Pradipta Panchadhyayee and Dr. Dwijendra Nath Sain. I would also like to thank all my family members for their unconditional love. I also thank my friends Atanu, Arka, Mukaddar, Paramita, Sudeshna, Dibyendu, Maheswar, Bikash, Rik, Abhilash bhaiya, Samir, Tanim, Prince, Rashmi for their unconditional help and support towards me.

I heartily thank Anupa for her constant support. I am fortunate enough to get constant support and cooperation from Gajanan. Your love, care and encouragement help me to overcome the hurdles and complete the journey.

Last but definitely not the least, I would like to take the opportunity to express my gratitude and love towards my parents for their unconditional love, support, and encouragement to fulfil my dream. I would like express my love towards my loving Bonu and Bhai. I cannot forget to mention about my loving grandma, Masi and kakumoni. My sincere gratitude to my late grandfather who always want to see my achievements. It was quite impossible to complete this journey without your support, encouragement and blessings.

Contents

Content Details **Page No.**

Summary

The main motivation of thesis work is to study the spinterface physics in metal (M)/ organic semiconductor (OSC) heterostructures where the metal is a non-ferromagnetic (NM) or ferromagnetic (FM) material. Our focus has been to control the magnetic properties of such heterostructures by formation of spinterface. To the date, the focus in the field of organic spintronic is mostly on the organic spin valves, organic light emitting diode and spin-transistor etc. Recently, fabricating such magnetic interfaces at M/OSC heterostructures and study the spinterface properties have become the major focus of the researchers for both fundamental as well as application point of view. However, the systematic study of the effect of spinterface on global magnetic properties are very few.

We have reported that ferromagnetism can be induced in a non-FM/OSC system e.g., Cu/C_{60}. To quantify the induced magnetic moment, we have performed X-ray magnetic circular dichroism (XMCD) measurements which revealed ~ 0.01 μ_B/atom magnetic moment in Cu at the Cu/C_{60} interface.

Further we focus on FM/OSC heterostructures because here spinterface state is very much crucial which may help to inject the spin into the OSC layer. In this context we wanted to understand the effect of spinterface on the global anisotropy, magnetic domains and damping. First, we considered in-plane magnetized films viz. CoFeB/C_{60} and Co/Rubrene. Further, we considered a perpendicularly magnetic anisotropic (PMA) based Pt/Co/C_{60}/Pt and Pd/Co/C_{60}/Pd systems because PMA systems are the most suitable candidates for data storage devices due to their high intrinsic anisotropy. We have observed significant enhancement in anisotropy in both in-plane and PMA systems. However, in Pt/Co/C_{60}/Pt and Pd/Co/C_{60}/Pd systems the domain size got reduced and the relaxation became fast due to the presence of Co-C_{60} spinterface, which is appealing for future data storage applications.

Although OSCs have very low spin-orbit coupling (SOC), it has been reported that due to the curvature the SOC may get enhanced in C_{60}. Spin pumping is a very efficient way of creation of pure spin current in FM/NM (here NM is a material exhibiting high SOC) system by microwave excitation which can be converted into a voltage by inverse spin Hall effect (ISHE). In this context, we have performed ISHE in CoFeB/C_{60} system and found clear evidence of spin pumping. We have calculated the spin mixing conductance and spin hall angle which are desired parameters for spin-to-charge conversion based spintronic devices.

List of Figures

3.7: Polarized neutron reflectivity (PNR) data measured at 3 K and remanence for sample SPC2 (a) and SPC3 (b).

3.8: XAS and XMCD spectra of the sample SPC2 measured at (a) 6T, (b) -6T and (c) 0T magnetic field at Cu $L_{2,3}$ edges. Similar for the SPC3 at (d) 6T, (e) -6T and (f) 0T. All the measurements were performed at 1.7 K.

3.9: $L_{2,3}$ edge XAS and XMCD spectra: The summed XAS and XMCD spectra and their integrations calculated from the spectra are shown for sample SPC2 (a), (b) and for sample SPC3 (c), (d), respectively. The dotted lines are the integral of the XAS spectra after subtracting two-step-like function from XAS spectra. The p, q and r are the three integrals needed in the sum-rule analysis.

4.1: (a) High resolution cross-sectional TEM image of SPI4. (b) SAED image of SPI4.

4.2: (a) The region of the sample SPI4 where the STEM-EDS has been performed. (b) Element specific mapping for each layer. (c) EDS line profile of each element present in the system. (d) EDS spectrum of sample SPI4 showing the presence of different elements.

4.3: XRR data and the best fits for samples SPI1, SPI2, SPI3, SPI4 and SPI5 are shown in (a), (b), (c), (d) and (e), respectively. The red open circles are experimental data, and the blue solid lines represent the best fits.

4.4: (a) Hysteresis loop measured along EA for sample SPI1. (b-f) Domain images captured at different field values, as marked in (a). Scale bar and the magnetic field direction are shown in (b) and same for all the images.

4.5: Hysteresis loops measured along ϕ = 0°, 30°, 45° and 60° for sample SPI1 (a), SPI2 (b), SPI4 (c) and SPI5 (d). (e) Hysteresis loop along HA (ϕ = 90°) for sample SPI1 (red), SPI2 (green), SPI4 (blue) and SPI5 (pink).

4.6: Domain images near H_C for samples SPI1, SPI2, SPI4 and SPI5 are shown in (1-5), (6-10), (11-15) and (16-20), respectively. Scale bar and the magnetic field direction are shown

6.1.6: Thickness dependence ($t_{C_{60}}$) of effective anisotropy (K_{eff}) (red solid circles), HA saturation field ($\mu_0 H_K$) (green stars) and saturation magnetization (M_S) (blue pentagon).

6.1.7: (a) Relaxation data for all the samples measured at H_M=0.93 H_C, where the red, blue, pink and green solid circles represent the raw data for SPP1, SPP2, SPP3 and SPP4, respectively, and solid lines are the best fits using equation (6.1.1). (b - e), (f - i), (j - m) and (n - q) show the domain images for the samples SPP1, SPP2, SPP3 and SPP4, captured at 0, 10, 15 and 20 seconds, respectively. Scale bar and the applied field direction are shown in (b) and same for all the images.

6.1.8: (a) Relaxation data for all the samples measured at H_M=0.95 H_C, where the red, blue, pink and green solid circles represent the raw data for SPP1, SPP2, SPP3 and SPP4, respectively, and solid lines are the best fits using equation (6.1.1). (b - e), (f - i), (j - m) and (n - q) show the domain images for the samples SPP1, SPP2, SPP3 and SPP4, respectively, which have been captured at 0, 5, 10 and 15 seconds. Scale bar and the applied field direction are shown in (b) and same for all the images.

6.1.9: (a) Relaxation data for all the samples measured at H_M=0.97 H_C, where the red, blue, pink and green solid circles represent the raw data for SPP1, SPP2, SPP3 and SPP4, respectively, and solid lines are the best fits using equation (6.1.1). (b - d), (e - g), (h- j) and (k - m) show the domain images for the samples SPP1, SPP2, SPP3 and SPP4, respectively, which have been captured at 0, 5 and 10 seconds. Scale bar and the applied field direction are shown in (b) and same for all the images.

6.1.10: Chemisorption of C_{60} molecule with a pentagonal-hexagonal adsorption geometry on HCP-Co(0001) substrate. (a) The top view of extended simulation supercell. The circled areas on the Co layer surfce represent different adsorption sites where T, H and B stands for Top, Hollow and Bridged adsorption sites on the Co substrate. Co1 and C1 are the free Co and C atoms. (b) Formation of spinterface on a single C_{60} unit. The bigger tan-coloured balls and

grey balls represent Co and C atoms, respectively. Cyan balls represent the C atoms (lebelled as C2) which participate in chemical bond formation with the Co (lebelled as Co2) atoms.

6.2.1: (a) Hysteresis loops of the samples SPP9 (blue) and SPP10 (red). (b-e) and (f-i) are the domain images for SPP9 and SPP10, respectively. Domain images corresponding to the points A-D of the hysteresis loops shown in (a). Scale bar and the applied field direction are shown in (b) and same for all the images.

6.2.2: (a) Relaxation data for all the samples measured at H_M=0.97 H_C, where the blue and red solid circles represent the raw data for SPP9 and SPP10, respectively, and solid lines are the best fits using equation (6.1.1). (b - e) and (f - i) show the domain images for the samples SPP9 and SPP10, repectively, which have been captured at 0, 10, 20 and 30 seconds, respectively. Scale bar and the applied field direction are shown in (b) and same for all the images.

7.1: Schematic of FMR and ISHE set-up and the sample structure. During the measurement we kept the sample upside down on top of CPW.

7.2: FMR signal (red circles with line) and V_{meas} (blue solid circles) vs applied DC magnetic field (H) plot for SPI1 (single layer CoFeB).

7.3: FMR signal (black circles with line) and V_{meas} (blue solid circles) vs applied DC magnetic field (H) for the sample SPI2 at (a) 0°, (b) 30°, (c) 90° and (d) 180° angles. Red solid line is the best fit to the equation, while red open squares and green open circles are the V_{sym} and V_{asym} contributions, respectively.

7.4: Angle dependence of V_{sym} (a) and V_{asym} (b) for samples SPI2. Black solid circles are the experimental data and red solid lines are the best fits using equations 7.3 and 7.4.

7.5: FMR signal (black circles with line) and V_{meas} (blue solid circles) vs applied DC magnetic field (H) for the sample SPI3 at (a) 0°, (b) 30°, (c) 90° and (d) 180° angles. Solid red line is

List of Tables

List of Abbreviations

AC	Alternating Current
AHE	Anomalous Hall effect
AMR	Anisotropic magnetoresistance
Ar	Argon
C	Carbon
CPW	Coplanar Waveguide
CVD	Chemical Vapour Deposition
DC	Direct Current
DFT	Density Functional Theory
DOS	Density of State
DW	Domain Wall
δ^{Bloch}	Bloch wall width
EA	Easy Axis
EDS	Energy Dispersive X-Ray Spectroscopy
FM	Ferromagnetic
FMR	Ferromagnetic Resonance
$g_{eff}^{\uparrow\downarrow}$	Spin mixing conductance
GGA	Generalized Gradient Approximations
GMR	Giant Magnetoresistance
H	Hydrogen
H_C	Coercive field
H_K	Anisotropy field for hard axis

H_N	Nucleation field
H_S	Saturation field
HA	Hard Axis
HFI	Hyperfine Interaction
HRTEM	High resolution transmission electron microscopy
ISHE	Inverse Spin Hall Effect
K_{eff}	Effective anisotropy constant
K_V	Volume dependent magneto crystalline anisotropy constant
K_S	Surface dependent magneto crystalline anisotropy constant
LL	Landau-Lifshitz
LLG	Landau-Lifshiftz-Gilbert
L_z	Orbital angular momentum
M_R	Remanent magnetization
M_S	Saturation magnetization
MAE	Magnetic anisotropy energy
MOKE	Magneto Optics Kerr Microscopy
MR	Magnetoresistance
MTJ	Magnetic Tunnel Junctions
N	Nitrogen
NM	Non-Magnetic
$N(E_F)$	Fermi level
O	Oxygen
OLED	Organic Light Emitting Diode
OMAR	Organic Magnetoresistance
OSC	Organic Semiconductor

OSV	Organic Spin Valve
PAW	Projected Augmented Wave
PBE	Perdew, Bruke, and Ernzerof
PMA	Perpendicularly Magnetic Anisotropy
PNR	Polarized Neutron Reflectivity
PVD	Physical Vapour Deposition
QCM	Quartz Crystal Monitor
RF	Radio Frequency
SAED	Selected Area Electron Diffraction
λ_s	Spin diffusion length
SHA	Spin Hall Angle
SHE	Spin Hall Effect
SO	Spin Orbit
SOC	Spin Orbit Coupling
SOT	Spin-orbit torque
SQUID	Superconducting Quantum Interference Device
SRT	Spin reorientation transition
STEM	Scanning Transmission Electron Microscopy
SV	Spin Valve
S_z	Spin angular momentum
τ_s	Spin relaxation time
TBS	Thermal Boat Supply
TEM	Transmission Electron Microscopy
TEY	Total Electron Yield
TFY	Total Fluorescence Yield

TMR	Tunnelling Magnetoresistance
UMA	Uniaxial Magnetic Anisotropy
VSM	Vibrating Sample Magnetometer
VASP	Vienna Ab-initio Simulation Package
XMCD	X-Ray Magnetic Circular Dichroism
XRR	X-Ray Reflectivity
Z	Atomic Number

CHAPTER 1: Introduction and Fundamentals

1.1: Introduction

Spintronics is known as spin-based electronics which explore both the spin and the charge state of an electron to transport the information. The new state of electrons (spin degrees of freedom) was introduced by Pauli in 1924. In 1975, Jullière first used the intrinsic spin of electrons in electronic devices by discovering the tunnelling magnetoresistance (TMR) in magnetic tunnel junctions (MTJ).[1] Fert and Grünberg independently discovered giant magnetoresistance (GMR) in 1988, which open a new path in the field of spintronics. [2,3] In the current generation, we are using GMR and TMR based spintronics data storage and sensing devices. All these GMR and TMR based devices have been prepared on ferromagnetic (FM)/non-magnetic (NM)/ferromagnetic (FM) metallic systems.[4–6] However, the metallic spintronics devices are limited by their short spin diffusion length and spin relaxation time (10^{-10} s).[4,5,7] To overcome this restriction upon applications immense research interest came towards the semiconductor-based devices sandwiched between two FMs. In the last few decades extensive studies have been done using non-magnetic metals, oxides and inorganic semiconductors as spacer layers.[5,8–10] In organic spintronics, organic semiconductors (OSCs) are utilized to transport the spin polarized signals. OSCs are basically composed of carbon (C) and hydrogen (H) atoms. Due to low atomic number (Z), spin orbit coupling (SOC) is low in these materials. In addition, OSCs exhibit less hyperfine interaction (HFI). Because of the low SOC and less HFI, spin scattering is less in the organic environment, hence spin relaxation time is larger in OSCs (10^{-7} to 10^{-5} s) and spin information is carried for a long time.[7,11] OSCs has gained attention in spintronics research not only for their large spin relaxation time but also low production cost, versatility of chemical synthesis and mechanical flexibility. Several works have been done on organic spin valve (OSV), organic solar cells, spin optical devices and organic magnetoresistance (OMAR) in the last two decades.[12–15] The most widespread application of

organic semiconductor is the organic light emitting diode (OLED), which is used in displays in monitors and smartphones.[16–20] The direct evidence of spin injection in sexithienyl (T_6) organic material from LSMO has been shown by Dediu et al., for the first time in 2002. They have observed a strong magnetoresistance (MR) at room temperature in LSMO/T_6/LSMO planar hybrid junction.[8] Xiong et al., have observed inverse spin valve effect (SV) in vertical OSV structure where two FM LSMO and Co have been separated by tris (8-hydroxyquinolinato) aluminium (Alq_3).[9] A 300% MR has been observed at 2K in LSMO/Alq_3/Co MTJ devices and 400% MR at 10 K in LPCMO/Alq_3/Co devices.[21,22] After these inventions researchers focused on preparing OSV using different OSCs to improve the GMR and TMR ratio. So far at room temperature, ~ 6% MR has been found in Fe_3O_4/AlO/Rubrene/Co structure and ~9% MR has been observed in Co/AlO_x/C_{60}/$Ni_{80}Fe_{20}$ stack.[23,24] In vertical OSV there is a significant intermixing between top FM/OSC interfaces. Therefore, to overcome this issue several works have been performed on lateral OSV.[25] The application of lateral OSVs is in organic field effect transistors (OFETs). A. Ozbay et al., have observed ~20% MR at low temperature in thick polymer P3HT having LSMO electrodes.[26] Later, S. W. Jiang et al., have fabricated LSMO/ pentacene/ LSMO lateral OSV and observed that the spin diffusion length of pentacene is less than 100 nm.[25] Recently, instead of using metallic FM, several OSV have been performed using molecular magnets.[27–29] The nature of the FM electrode and the OSC interface plays a crucial role in spin injection which affects the magnitude of MR. Therefore, in addition to these spin valve effects it is also important to understand the basic underlying physics behind the spin injection/transport in the devices. It has been observed that when an OSC comes into contact with a FM, at the interface the density of state (DOS) of the OSC is modified and becomes magnetic. This magnetic interface of the FM/OSC is known as spinterface.[30] Moorsom et al. have been shown that 1.2 μ_B magnetic moment can be induced per cage of C_{60} in Co/C_{60} multi-layered system. They have also

observed suppression of magnetic moment of Co up to 21%. [31] Similarly, due to the hybridization between C_{60} and Fe orbitals, magnetic polarization of C_{60} has been observed in C_{60} monolayers on Fe (001) substrate[32]. Mallik et al. have shown that crystallinity of the FM material affects the spinterface properties[33–35]. They have observed that ~2 nm of C_{60} became magnetic at epitaxial Fe/C_{60} interface and exhibits ~ 2.95 μ_B/cage magnetic moment.[33] For the polycrystalline Fe/C_{60} case the induced moment in C_{60} is reduced to ~1.5 μ_B/cage.[34] Spinterface can also modify the anisotropy, magnetization reversal and domain structure of an in-plane magnetic system.[33–35] It has been demonstrated by Bairagi et al. that the C_{60} layer can change the anisotropy of an ultrathin Co layer from in-plane to out of plane.[36] However, the effect of spinterface on magnetic domain, magnetization reversal and relaxation in an out-of-plane system has not been performed yet. Recently, Ma Mari et al., have shown that OSC/metal interface can alter the electronic state of non-magnetic (NM) metal (Cu, Pt, Mn, Sc etc.) and they have observed ferromagnetism at NM metal/C_{60} interface.[37,38] They have found that due to charge transfer and interface reconstruction Cu/C_{60} and Mn/C_{60} multilayers thin films exhibit ferromagnetism at room temperature.[37] The quantification of the induced moment at metal still has not been reported yet.

Although OSCs exhibit low SOC, it has been reported that SOC can be enhanced in C_{60} when deposited on top of a ferromagnet.[39]

Usually high SOC materials (Pt, W, Ta, IrMn, Bi_2Se_3 etc) are used for spin to charge conversion[40–42]. But these are limited by their small spin diffusion length (λ_s). In this context, OSCs (e.g., C_{60}) are the potential candidates due to their large λ_s.[43] The study of the spin to charge conversion in OSCs has not been explored much.

In this thesis, we focus on spinterface physics in M/OSC thin films where M is a non-ferromagnetic or ferromagnetic (FM) metallic material. The objectives are divided into five parts depending on the metal and the OSC.

(i) First, we have studied the non-magnetic Cu and C_{60} interface and observed ferromagnetism at room temperature in the sample stack. Using X-ray magnetic circular dichroism (XMCD) we have quantified the magnetic moment induced in Cu at Cu/C_{60} interface.

(ii) Afterwards, we have focused on the FM/OSC interface. We considered in-plane anisotropic CoFeB/C_{60} systems and studied the effect of spinterface on the magnetic properties of the system such as magnetic anisotropy, domains and damping.

(iii) Next, considering a different OSC i.e., Rubrene we have studied the spinterface effect in Co/Rubrene in-plane anisotropic system.

(iv) Further, we focused on perpendicularly magnetic anisotropic (PMA) based systems (Pt/Co/Pt and Pd/Co/Pd). We have investigated the effect of C_{60} on the magnetic anisotropy, domains and magnetization relaxation.

(v) Although OSCs like C_{60} has low SOC, enhancement of SOC has been reported for C_{60} when it is deposited on a FM substrate. In this context, we have performed inverse spin Hall effect (ISHE) measurements and observed spin pumping in CoFeB/C_{60}bilayer system.

The thesis is organized in the following manner. In **Chapter 1**, the state of art of the research field and the motivation behind the thesis work have been discussed. Further, some fundamentals which are relevant to understand the results have been discussed. The working principle and details of the experimental techniques used to prepare and characterize the samples have been explained in **Chapter 2**. Observation of ferromagnetism at room-temperature in non-magnetic Cu/C_{60} sample stack and the quantification of magnetic moment induced in Cu at Cu/C_{60} interface via XMCD has been discussed in **Chapter 3**. **Chapter 4** describes how the spinterface affects the magnetic anisotropy, domain and damping in an in-plane anisotropic CoFeB/C_{60} system. In **Chapter 5**, similar kinds of studies have been

performed in a different FM/OSC system i.e., Co/Rubene system. In **Chapter 6**, we have shown that C_{60} has significant effect on magnetic anisotropy, domains and magnetization relaxation in PMA based Pt/Co/C_{60}/Pt and Pd/Co/C_{60}/Pd systems. Further, using density functional theory (DFT) calculations, the nature of Co-C_{60} spinterface has been investigated. Observation of spin pumping and ISHE in CoFeB/C_{60} bilayer systems have been described in **Chapter 7**. We also calculated the spin mixing conductance and spin Hall angle (SHA) for C_{60}. In **Chapter 8**, summary of all the work done in this thesis and the future outlook has been discussed.

1.2: Fundamentals

1.2.1: Ferromagnetism:

Ferromagnetism is defined by the concept of occurrence of spontaneous magnetization even if no external magnetic field is applied to the system. In the periodic table, only a few 3*d* metals like Fe, Ni and Co exhibit ferromagnetism at room temperature. The DOS of a FM and a NM metal at Fermi level is different from each other (shown in figure 1.1). There are different mechanisms (band split mechanism, different exchange interaction etc.) which can describe the ferromagnetic state. The origin of ferromagnetism can be described via the well-known Stoner criterion.[44,45]

1.2.1.1: Stoner criterion:

A non-magnetic system consists of equal number of 'spin up' and 'spin down' electrons ($n_{\uparrow} = n_{\downarrow} = n$). In case of ferromagnetic system, there must be an imbalance in the spin states as magnetization $(M) = (n^{\uparrow} - n^{\downarrow})\mu_B$. 3*d*-transition ferromagnetic metals such as Fe, Ni and Co have narrow bandwidth and large DOS at Fermi level ($N(E_F)$) leading to large Pauli susceptibility $\chi_P = 2\mu_0 N(E_F)\mu_B^2$. Stoner applied Pierre Weiss's molecular field idea to the free electron model and it induces an enhancement in Pauli susceptibility. The total field acting in the system is $\boldsymbol{H} + n_W \boldsymbol{M}$, where n_W is the Wiess constant. The enhanced magnetic susceptibility

is expressed as $\chi = \frac{M}{H} = \frac{\chi_P}{(1-n_W\chi_P)}$. When $n_W\chi_P > 1$, the susceptibility diverges and spin up and spin down bands split separately which leads to ferromagnetism (figure 1.1 (b)). We can write the exchange energy per unit volume as $-\frac{1}{2}\mu_0 H^i M = -\frac{1}{2}\mu_0 n_s M^2 = -\frac{1}{2}\mu_0 n_s (n^{\uparrow} - n^{\downarrow})^2 \mu_B^2$. By equating this to the stoner expression $-\frac{I_0}{4}(n^{\uparrow} - n^{\downarrow})^2$ one can get $I_0 = 2\mu_0 n_W \mu_B^2$. Therefore, the criterion for ferromagnetism $n_W\chi_P > 1$ can be expressed as $I_0 N(E_F) > 1$.[45]

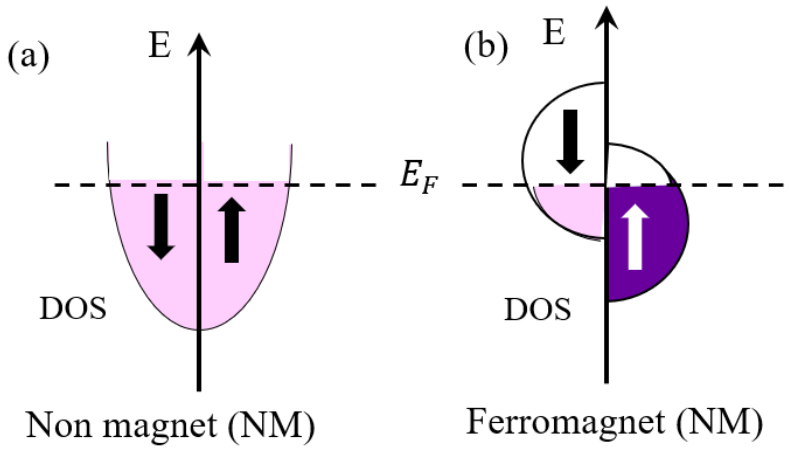

Figure 1.1: DOS at Fermi level for (a) non-magnetic and (b) ferromagnetic metal.

1.2.2: Magnetic anisotropy

Magnetic anisotropy is defined as how the magnetic properties of a system depend on the direction of an applied magnetic field. For an isotropic ferromagnetic system, the energy levels do not depend on the spatial direction of the magnetic field. It is known that, for a magnetic system the Heisenberg Hamiltonian is completely isotropic in nature and the magnetization would vanish at zero field if no other energy is associated with the system. However, in reality the magnetic materials are not isotropic in nature. The magnetic moments in a ferromagnetic material cannot be rotated to any direction by applying an infinitesimally small energy. This is due to the presence of anisotropy energy which helps in keeping the spins in a particular direction[46]. For a magnetically anisotropic system there is a preferred direction in which it is easy to magnetize the material and it is known as easy axis (EA). Similarly, for the non-

preferential direction of magnetization in which maximum field is required to saturate the material is known as hard axis (HA). Magnetic anisotropy can be classified into four parts[46]:

Magneto crystalline anisotropy: Magnetization direction is oriented along specific crystalline axes. The spin orbit (SO) interaction gives rise to this anisotropy.[46]

Shape anisotropy: The magnetization of the material is affected due to the shape of the material. The long-range dipolar interaction is responsible for this anisotropy.[46]

Surface anisotropy: For ultrathin ferromagnetic films, the surface anisotropy plays a relevant role over the volume anisotropy as the surfaces and the interfaces exhibit different magnetic properties in comparison to the bulk due to their asymmetric environment.[46]

Stress (magnetostriction) anisotropy: Due to the occurrence of stress induced anisotropy, magnetization leads to a spontaneous deformation and vice-versa. SO interaction is responsible for this anisotropy contribution.[46]

In the following, we have discussed the origin and the different components of the magneto crystalline anisotropy and surface anisotropy.

1.2.2.1: Magneto crystalline anisotropy:

Magneto crystalline anisotropy has the most important contribution in magnetic anisotropy of a system. This anisotropy arises due to the SO interaction of the electrons. Each of the electron orbitals are associated to the specific crystallographic axes. Due to the interaction between the orbitals and spins of electrons, the spins favour to align in a certain crystallographic axis. As compared to the exchange energy, the strength of the magneto crystalline anisotropy is usually small. However, the magnetization direction is only determined by this anisotropy as the exchange interaction tries to align the magnetic moments parallel or antiparallel irrespective to their directions. The direction of magnetization ($\boldsymbol{m} = \frac{\boldsymbol{M}}{|\boldsymbol{M}|}$) relative to the coordinate axes can be expressed using direction cosine m_i as $\boldsymbol{m} = (m_x, m_y, m_z)$ with $m_x = \sin\theta\, cos\phi$, $m_y = \sin\theta \sin\phi$ and $m_z = \cos\theta$ (shown in figure 1.3) where $m_x^2 + m_y^2 + m_z^2 = 1$.

The magneto crystalline energy per unit volume can be given by a power series of the components of the magnetization[46]:

$$E_{crystal} = E_0 + \sum_i b_i m_i + \sum_{ij} b_{ij} m_i m_j + \sum_{ijk} b_{ijk} m_i m_j m_k + \sum_{ijkl} b_{ijk} m_i m_j m_k m_l + T(m^5) \quad (1.1)$$

where, b is the coefficient of the anisotropy energy. The term $T(m^5)$ is very small and hence can be neglected.

The energy of the oppositely magnetized system is equal in magnitude and $E(m_i) = E(-m_i)$. Thus, the odd terms of m_i will cancel out and the expansion can be written as[46]:

$$E_{crystal} = E_0 + \sum_{ij} b_{ij} m_i m_j + \sum_{ijkl} b_{ijk} m_i m_j m_k m_l \quad (1.2)$$

Depending on the crystallographic orientation, magneto crystalline anisotropy can be divided into several parts viz. uniaxial anisotropy, cubic anisotropy, six-fold anisotropy etc.

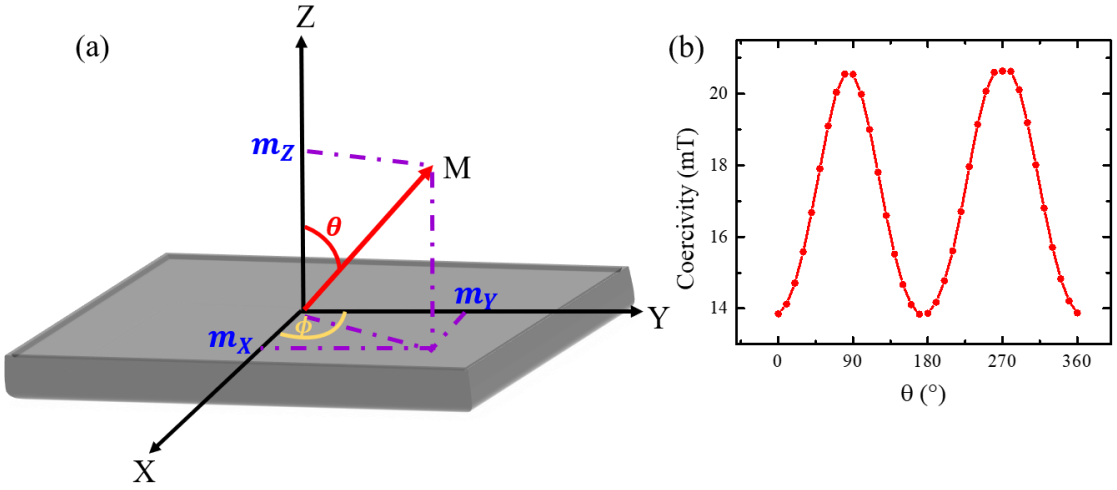

Figure 1.2: (a) Schematic representation of the magnetization vector w.r.t the direction cosine. (b) Angle dependence of coercivity plot with two-fold symmetry over 360° interval.

1.2.2.1.1: Uniaxial magnetic anisotropy**:**

The name indicates that the system having uniaxial magnetic anisotropy (UMA) has only one preferred direction of EA over 180° interval. Due to $E(m_i) = E(-m_i)$, all the cross terms $m_i m_j$ will cancel out each other, i.e., $b_{ij} = 0$ for $i \neq j$.

Now, if we consider the EA is aligned along z axis, the energy associated to the system can be described as:

$$E_{crystal} = E_0 + b_{xx}m_x^2 + b_{yy}m_y^2 = E_0 + b_{xx}\left(m_x^2 + m_y^2\right);\ as\ b_{xx} = b_{yy} \qquad (1.3)$$

Hence, the energy per unit volume for uniaxial anisotropy is $E_{crystal} = E_0 + b_{xx}\sin^2\theta$, where E_0 is the zeroth coefficient and b_{xx} is the uniaxial anisotropy constant. Due to the two-fold symmetry over the 360° interval, in this thesis the uniaxial anisotropy constant has been denoted by K_2 (shown in figure 1.2 (b)).

1.2.2.2: Shape anisotropy:

The shape of the material also contributes in magnetic anisotropy. The long-range dipolar interaction is responsible for this anisotropy. If the material is spherical in shape the same energy is needed to magnetize the sample in any direction. However, if the material is non spherical, there is a particular direction along which it can be easily magnetized. As the demagnetized field along the short axis is stronger than the long axis, it is easy to magnetize the sample along a long axis. The stray field energy of a system is given by: $E_{str} = -\frac{1}{2}\int \mu_0 M.H_{demag}dV$, where H_{demag} is the demagnetizing field inside the sample. In an ellipsoid $H_{demag} = NM$, where N is the demagnetizing tensor and if the semiaxes of the ellipsoid represent the axes of the coordinate system then N (trace = 1) is given as:[46]

$$N = \begin{pmatrix} N_x & 0 & 0 \\ 0 & N_y & 0 \\ 0 & 0 & N_z \end{pmatrix}.$$

Thus, the stray field energy can be written as:[46]

$$E_{str} = -\frac{1}{2}\mu_0 VM.NM = -\frac{1}{2}\mu_0 V\left(N_x m_x^2 + N_y m_y^2 + + N_z m_z^2\right) \qquad (1.4)$$

$N_x = N_y$ along the equatorial axis of an ellipsoid of revolution. In a simple form E_{str} can be written as:

$$E_{str} = -\frac{1}{2}\mu_0 V(N_x m_x^2 \sin^2\theta + N_z m_z^2 \cos^2\theta) = -\frac{1}{2}\mu_0 V M^2 (N_x - N_z)\sin^2\theta = K_{shape} V \sin^2\theta \quad (1.5)$$

Therefore, shape anisotropy constant (K_{shape}) can be expressed as:

$$K_{shape} = \frac{1}{2}\mu_0 (N_x - N_z) M^2 \quad (1.6)$$

When the material is spherical i.e., $x = z$, the shape anisotropy become zero.[46,47]

1.2.2.3: Surface anisotropy:

Due to the broken symmetry at the interface, the contribution of surface anisotropy plays an important role along with the volume anisotropy in ultra-thin magnetic films. Thus, the effective anisotropy constant K_{eff} contains both the volume and surface contribution and can be written as[46]:

$$K_{eff} = K_V + {}^{2K_S}/_{t} \quad (1.7)$$

Where, K_V and K_S are the volume and surface dependent magneto crystalline anisotropy constants, respectively. In the second term, a factor of two is multiplied because of the creation of two surfaces in the film. The thickness (t) of the film is only important for ultra-thin films as it inversely proportional to K_{eff}. We can rewrite the equation (1.4) as following:[46]

$$tK_{eff} = tK_V + 2K_S \quad (1.8)$$

The surface and volume contributions become equal at critical thickness $t = t_C$, where $t_C = {}^{-2K_S}/_{K_V}$. For $t < t_C$, the system exhibits perpendicular magnetization and for $t > t_C$ magnetization is in the plane of the film. With increasing the thickness of the film magnetization of the system rotates from out-of-plane to in-plane, which is known as spin reorientation transition (SRT). Thus, thick films are having in-plane magnetization, volume contribution always dominates in this case. Lowering the thickness, surface contribution increases which leads to the SRT and magnetization is preferred along perpendicular to the film plane.[48–51]

1.2.3: Magnetic domains and domain walls:

In 1907, P. Weiss stated that inside a ferromagnetic material there are several small regions (called "magnetic" domains) inside which all the spins are aligned along a particular direction.[52] However, the magnetization direction of each domain is not necessarily to be aligned along the EA of the material. To minimize the magnetostatic energy the direction of spontaneous magnetization varies from domain to domain in the absence of any external magnetic field. Domains are small in size (1-100 micron) but much larger than atomic distance.[53] Individual domains are separated by domain boundaries, known as 'domain walls' (DWs). The magnetization must change its direction at or within the wall.[54] DWs have a finite width which is determined by magneto crystalline and exchange energy.

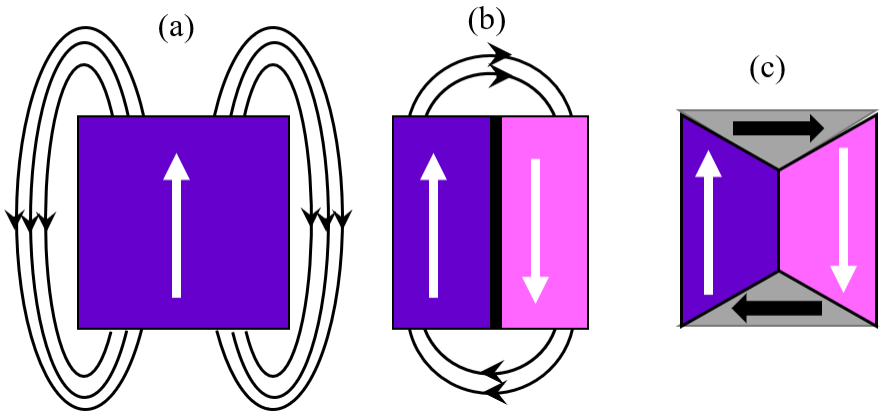

Figure 1.3: Schematic representation of formation of magnetic domains to reduce the magnetic stray field energy. Different domains are represented in different colours. The black line separating the two domains is known as a domain wall.

Due to presence of exchange and anisotropy energy, all the spins inside a magnetic material try to align themselves towards the easy direction of magnetization and leading to the formation of a single domain state (figure 1.3 (a)) as the exchange energy of the system is minimum when the spins are either parallel or antiparallel to each other. Depending on the shape of the material, the orientation of all the spins along a particular direction will generate demagnetizing field. If the demagnetization energy of a uniformly magnetized single crystal is larger than the

anisotropic energy, the magnetic moments will split into multiple domains (figure 1.3 (b), (c)) to minimize the total energy of the system. This splitting of more domains cannot be continued indefinitely because a finite energy is also required to form a DW. Therefore, a competition between the DW energy and stray field energy determines the ground state of the system. Landau and Liftshitz proposed that the stray field energy of a system can be reduced to zero by flux closure domain type (figure 1.3 (c)). Due to the Heisenberg exchange interaction, the direction of the magnetic moments inside a DW changes continuously to minimize the energy of the system. The exchange energy between two neighbouring spins (at an angle φ with respect to each other) is expressed as[46]:

$$E_{exch} = -2J\boldsymbol{S_1}.\boldsymbol{S_2} = -2JS^2\cos\varphi \tag{1.9}$$

The energy required to flip the spin from one direction to the opposite direction (i.e., $\varphi = \pi$) is $2JS^2$. For an ensemble of spins, the total exchange energy of every spin rotation axis for N lattice spacing can be written as[46]:

$$\Delta E_{exch}^{Total} = E_{exch} - E_{exch}^{\varphi=0} = N.JS^2\,(\cos\frac{\varphi}{N} - 1) = -N.JS^2(1 - \frac{\varphi^2}{N^2} - 1) = \frac{JS^2\pi^2}{N} \tag{1.10}$$

If a is the lattice constant of a material, then the Bloch wall experiences $1/a^2$ spin rotation which leads to an exchange energy of

$$E_{exch}^{Bloch} = \frac{JS^2\pi^2}{Na^2} \tag{1.11}$$

The above equation shows that the exchange energy will decrease with increasing N which leads to increase in the width of the DW. However, the anisotropy energy favours short DW width. Hence, to stabilize the width of the DW both energy contributions try to align the DW width into the opposite direction. For the Bloch wall, the anisotropy energy is given by[46]:

$$E_{ani}^{Bloch} = \sum_{i=1}^{N} K\sin^2\varphi_i \cong \frac{NKa}{2} \tag{1.12}$$

Therefore, the total energy of the Bloch wall can be written as:

$$E^{Bloch} = \frac{JS^2\pi^2}{Na^2} + \frac{NKa}{2} \tag{1.13}$$

The domain wall width of Bloch wall is defined as[46,53]: $\delta^{Bloch} = \pi\sqrt{A/K}$, where $A = \frac{2JS^2}{a}$.

Figure 1.4 shows two different types of magnetic DWs named as (a) Bloch wall and (b) Néel wall. In Bloch wall, spin rotation inside the DW happens in out-of-plane direction (i.e, the rotation of magnetization is parallel to the plane of the DW). In Néel wall, the rotation of spin takes place in in-plane direction (i.e., the magnetization rotation is perpendicular to the plane of the DW). Formation of Bloch walls are usually obtained in bulk ferromagnetic materials/ thick films. Whereas, Néel wall occurs in ultrathin films where the thickness of the film is comparable to the DW width.

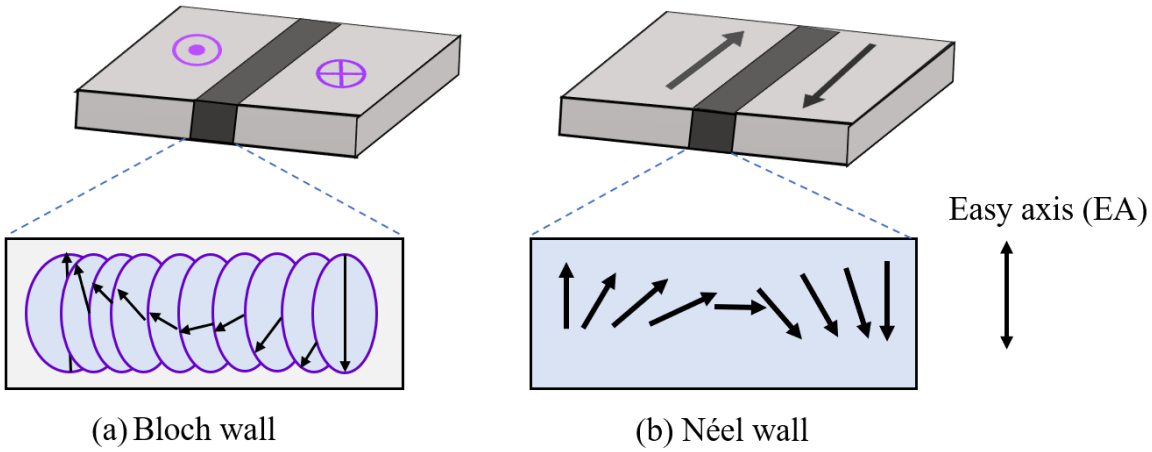

Figure 1.4: Schematic representation of (a) Bloch wall and (b) Néel wall representing the magnetization rotation.

Depending on the angle of magnetization between two neighbouring domains, there can be several types of DWs *viz*.: 90°, 180°, and 360° DWs. The schematic representation of these DWs are shown in figure 1.5. Systems having cubic anisotropy lead to the formation of 90° DW (figure 1.5 (a)) as the EA directions of magnetization are 90° away from each other[55]. Hence, the magnetization switching from positive to negative direction happens via 90° DW under application of an external magnetic field. 180° DWs (figure 1.5 (b)) are observed in the

systems having uniaxial anisotropy.[56] For a few special cases 109°, 71° and 360° DWs (figure 1.5 (c)) have also been obtained.[57,58]

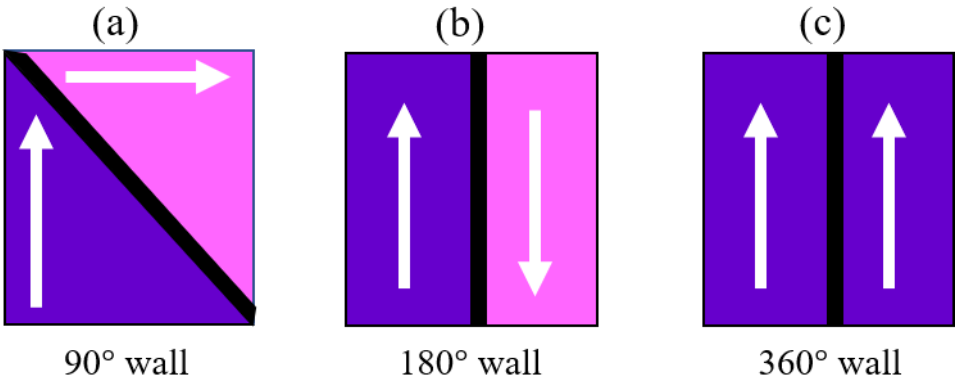

Figure 1.5: Schematic representation of (a) 90°, (b) 180°, and (c) 360° domain walls. The black lines between the domains of different magnetization represent the domain wall.

1.2.4: Magnetization reversal:

Magnetization reversal is a phenomenon where under the influence of an external magnetic field the spontaneous magnetization of a ferromagnet reverses/switches from one saturated state to another saturated state. When a magnetic field is applied to a ferromagnetic sample, a torque ($\boldsymbol{\tau} = \boldsymbol{M} \times \boldsymbol{H}$) acts on the spins which changes magnetic state to minimize the energy of the system. The magnetization reversal can happen via two methods: domain wall motion (magnetization changes from one state to another by movement of DWs) and coherent rotation (all the spins coherently rotate from one stable state to another in a coherent manner). The reversal process depends on the initial distribution of magnetization in the sample as well as the speed of the reversal field.

The magnetization of a ferromagnet does not reacts to the change in applied magnetic field linearly, gives rise to the hysteresis loop. Hysteresis is a nonlinear, non-equilibrium first order phase transition.[59] A typical hysteresis loop in a ferromagnetic sample is shown in figure 1.6. When a sufficiently large magnetic field is applied to ferromagnetic material, all the spins inside the material align along the applied field direction. The magnetization of the material at this state is known as saturation magnetization (M_S) and the required field to obtain this state

is called saturation field (H_S). Now if we start decreasing the field, at zero field the magnetization does not become zero. This non-zero magnetization at zero applied field is known as remanent magnetization (M_R). A finite magnetic field is needed in the reverse direction to reduce the magnetization to zero. This required field is called coercive field (H_C). The squareness of a hysteresis loop is defined as $S = \frac{M_R}{M_S}$. For an ideal ferromagnet S is 1 along EA and 0 along HA. In the following we will discuss the mechanism involved in this magnetization reversal.

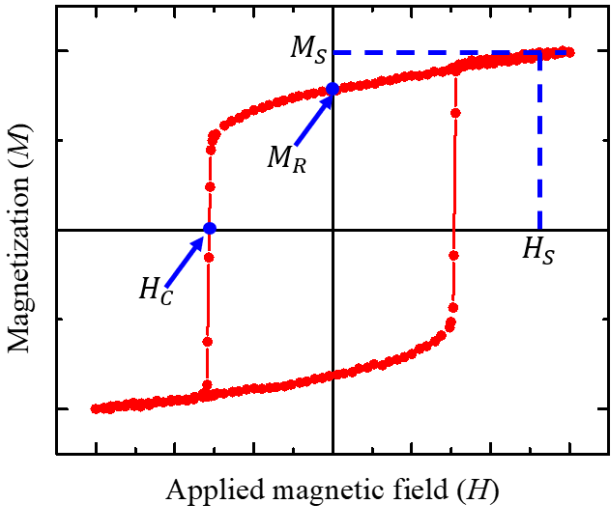

Figure 1.6: Hysteresis loop showing magnetization (M) vs applied magnetic field (H) behaviour in a ferromagnetic material.

1.2.4.1: Coherent rotation:

The magnetization reversal of a single domain nanoparticle occurs via coherent rotation which can be described via Stoner Wohlfarth model. Magnetization reversal for a thin film along HA can be explained via this mechanism. Along HA of a thin film all the spins coherently rotate from one saturated state to another to complete the reversal. The energy required for DW formation is significantly high when the dimension of the ferromagnetic particle is very low and in this condition the exchange energy of the system becomes minimum due to the parallel

alignment of the atomic spins. Therefore, the magnetic free energy under the application of a magnetic field can be described as the sum of anisotropy and Zeeman energy:

$$E = K \sin^2 \theta - \mu_0 H M_S \cos(\phi - \theta) \tag{1.14}$$

where, the orientation of ϕ and θ with respect to H, M and EA is shown in figure 1.7.

The equilibrium of magnetization $\frac{dE}{d\theta} = 0$. i.e.,

$$2K \sin\theta \cos\theta - \mu_0 H M_S \sin(\phi - \theta) = 0 \tag{1.15}$$

Along HA the applied magnetic field is normal to the EA and $\phi = 90°$. Therefore, the anisotropy field can be achieved by solving the eqn. 1.14 for HA which is given by:

$$H_K = \frac{2K}{\mu_0 M_S} \tag{1.16}$$

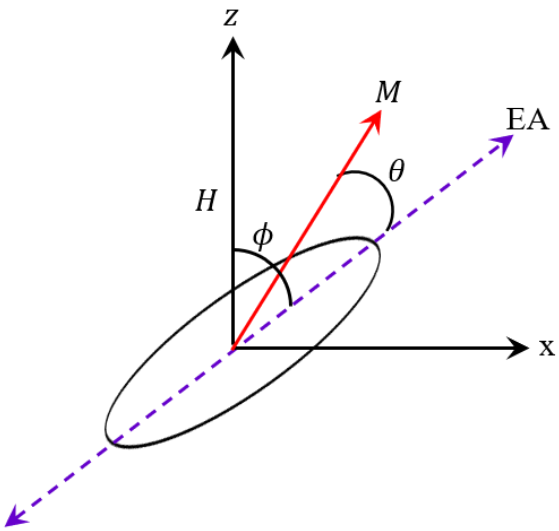

Figure 1.7: Orientation of ϕ and θ with respect to H, M and EA for Stoner Wohlfarth model.

When the applied magnetic field is along EA ($\phi = 0°$) the orientation of magnetization remains unaffected until the applied field reaches to H_K. Now if the field is further applied along the direction $\phi = 180°$, both the field and M_S are antiparallel to each other and no torque on M_S. However, the magnetization will become unstable at $\phi = 0°$ and will flip to $\phi = 180°$. When the direction of applied field is away from EA ($0° < \phi < 90°$), the magnetization reversal initially starts via reversal rotation of spins. When the field is applied in a reverse direction

along HA ($\phi = 90°$), all the spins rotate coherently which leads to a 'S' shape hysteresis loop (figure1.8 (b)).

1.2.4.2: Domain wall motion:

Another process involved in magnetization reversal is DW motion. In a ferromagnetic sample the formation of a domain arises in order to reduce the magnetic stray field energy of the system. When a magnetic field is applied on a demagnetized sample, domains which are oriented in the applied field direction start to grow at the expense of other domains which are

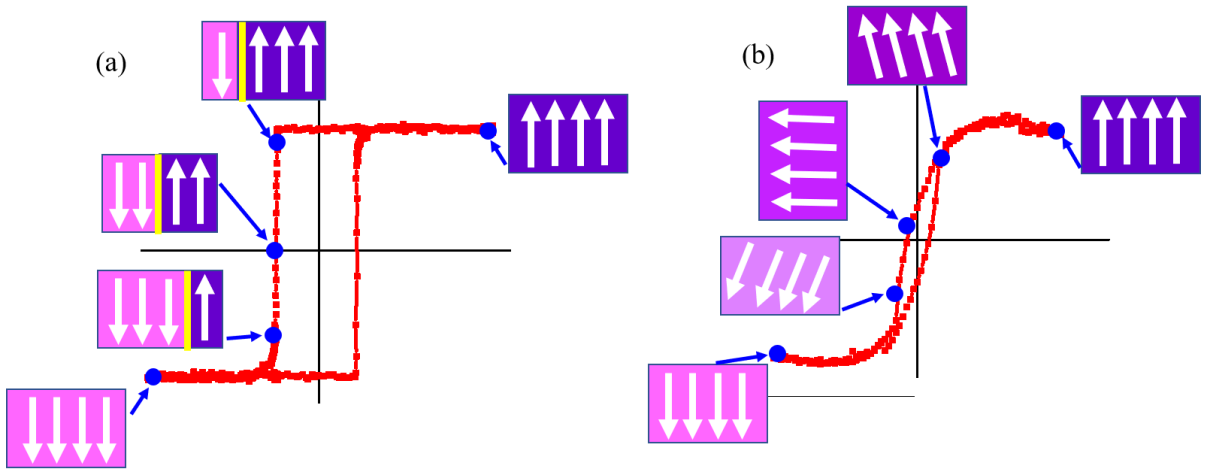

Figure 1.8: Schematic representation of magnetization reversal via (a) domain wall motion and (b) coherent rotation.

unfavourably aligned. DWs can move a small distance after application of a small field and come back to the initial position after removing the field. This mechanism is known as reversible displacement and correspond to the initial curve part of the hysteresis loop. At the intermediate to high field, the anisotropy can be overcome where the magnetization rotates away from its EA to the next crystallographic easy orientation nearest to the field direction. If the applied field is increased further the domains rotate collectively towards the applied field direction. Near the coercive field (H_C) there is a jump in the hysteresis loop which is known as the Barkhausen effect. A schematic representation of the steps of the magnetization reversal via DW motion is shown in figure 1.8 (a). When a sufficiently large field is applied to the

sample all the spins are aligned along the applied field direction and this leads to a single domain state. When the field starts increasing in the opposite direction, some spins get switched to the opposite direction. In figure 1.8 (a) the yellow line represents the $180°$ DW. Further increment of the field leads to reversal of more spins leading to the movement of the DW. Therefore, magnetization reversal from one saturation to opposite saturation state is happening via the movement of the DW which is known as DW motion.

In the results section we have discussed the magnetization reversal via DW motion as well as coherent rotation.

1.2.5: Magnetization dynamics:

1.2.5.1: Landau-Lifshitz-Gilbert (LLG) equation:

The dynamic properties of a magnetic system can be expressed in terms of Landau-Lifshitz-Gilbert (LLG) equation. In 1935 Landau and Lifshitz proposed a dynamical model which contain the precessional motion of the magnetization. The model focuses on the continuous precession equation which considers the quantum-mechanical effects and magnetic anisotropy by means of applied field (H). The Landau-Lifshitz (LL) equation is given by

$$\frac{\partial \boldsymbol{M}}{\partial t} = -\gamma \boldsymbol{M} \times \boldsymbol{H} \tag{1.17}$$

The LL equation is a conservative equation. But the dissipative processes are also present within this dynamic magnetization process. Landau and Lifshitz introduced an additional torque term to explain this dissipation which forces magnetization in the direction of the applied field as shown in Figure 1.9. The Landau-Lifshitz equation becomes

$$\frac{\partial \boldsymbol{M}}{\partial t} = -\gamma(\boldsymbol{M} \times \boldsymbol{H}) - \frac{\lambda}{M_S} \boldsymbol{M} \times (\boldsymbol{M} \times \boldsymbol{H}) \tag{1.18}$$

where, λ is characteristic constant of a material. The magnitude of magnetization (saturation magnetization) is preserved since $|M| = M_s$.

A different approach was proposed by Gilbert in 1955. He introduced a kind of 'viscous force' in this framework, phenomenologically. He added the following term to LL equation:

$$\frac{\alpha}{M_S} M \times \frac{dM}{dt} \tag{1.19}$$

Finally, the LL equation was modified to the LLG equation (Landau-Lifshitz-Gilbert equation) which is expressed as

$$\frac{d\boldsymbol{M}}{dt} = -\gamma(\boldsymbol{M} \times \boldsymbol{H}) + \frac{\alpha}{M_S}\left(\boldsymbol{M} \times \frac{d\boldsymbol{M}}{dt}\right) \tag{1.20}$$

where, γ is the gyromagnetic ratio and α is the Gilbert damping constant, which can be evaluated by ferromagnetic resonance measurement.[60]

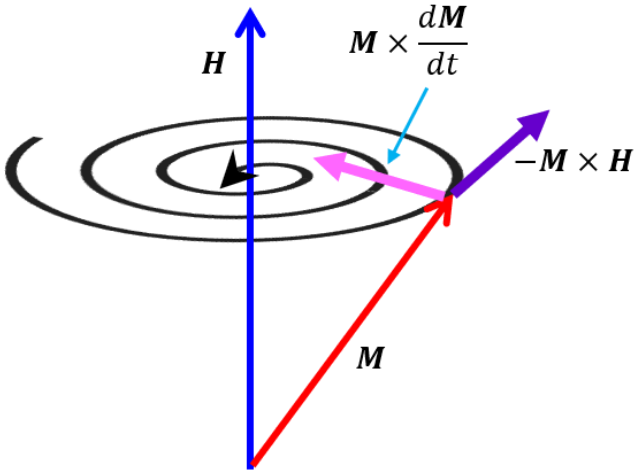

Figure 1.9: Precession of magnetic moment (***M***) around the applied field (***H***) along with a damping.

1.2.6: Organic spintronics:

Organic spintronics is an emerging field for future spintronics devices. In organic spintronics, organic semiconductors (OSCs) are used to control/or transport spin polarized signals. In the following, we will discuss the properties of OSCs and the reasons which make them promising candidates for spintronic applications.

1.2.6.1: Organic semiconductor:

Organic semiconductors are basically π-conjugated molecules which are composed of low atomic number elements like carbon (C) and hydrogen (H), oxygen (O) and nitrogen (N) etc. π-conjugated molecules consist of sp^2 hybridized C atoms whereas in C-based polymers the valence electrons of C atom are bonded with sp^3 hybridization. Different types of hybridization are discussed below.

1.2.6.1.1: Hybridization:

The ground state electron configuration of C is $1s^2 2s^2 2p^2$. C atoms can bond themselves and other elements with *sp*, sp^2 or sp^3 orbitals. The hybridization of orbitals is important as the energy of the hybridized orbitals are lower comparison to the un-hybridized ones.[61] In the first step of the hybridization, one electron jumps from 2*s* to 2*p* states leading to the excited state of C which is not an energetically favourable state. Therefore, to form an energetically favoured state, *s* and *p* orbitals of the excited states are hybridized.

***sp* hybridization:** In the case of *sp* hybridization, the 2*s* orbital is hybridized with only 2*p* orbitals and resulting two *sp* hybrid orbitals. As only one *p* orbital takes part in the hybridization, the other two *p* orbitals are left-out. Here, two *sp* hybrid orbitals are arranged in a linear geometry with 180° angle and the two unhybridized 2*p* orbitals are at 90° to each other. The ground state, excited state, hybridized state and *sp* hybridized orbitals are shown in figure 1.10 (a) to (d), respectively.

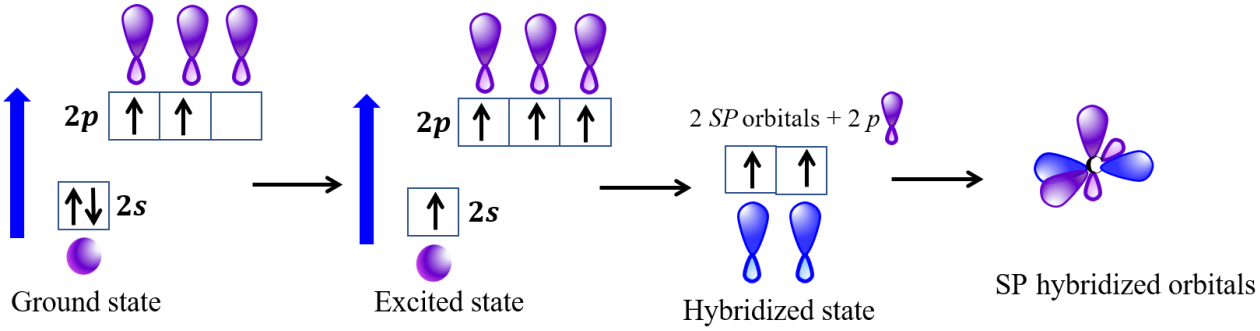

Figure 1.10: Schematic representation of energy levels of carbon and *sp* hybridized orbitals.

sp*^{2} hybridization:** When the 2*s* orbital is mixed with two 2*p* orbitals, the hybridization is called as sp^2 hybridization. Here, three orbitals are mixed and resulting to three ***sp hybridized orbitals.

The three ***sp*** hybridized orbitals are arranged in a tetragonal planar geometry (120°) and unhybridized *p* orbital is perpendicular to the plane of the trigonal planar arrangement.

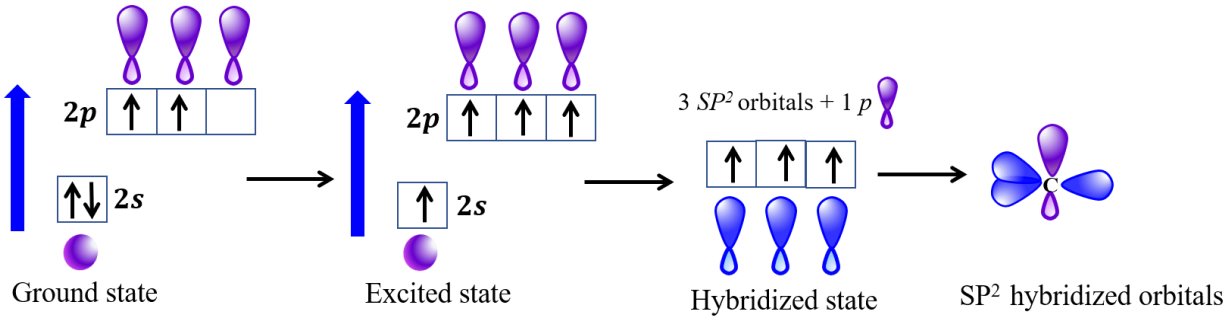

Figure 1.11: Schematic representation of energy levels of carbon and sp^2 hybridized orbitals.

sp^3 hybridization: In case of sp^3 hybridization the 2*s* orbital are hybridized with all the three 2*p* orbitals to form four *s*-*p* hybridized orbitals. Each of the four *s*-*p* hybridized orbitals consist of 25% of *s* and 75% of *p* character. It is called sp^3 hybridization as the hybridization is happening between one *s* and three *p* orbitals. The four ***sp***-hybridized orbitals align themselves in a tetrahedral manner to minimize the electron repulsion. Figure 1.12 shows the schematic of formation of sp^3 hybridization.

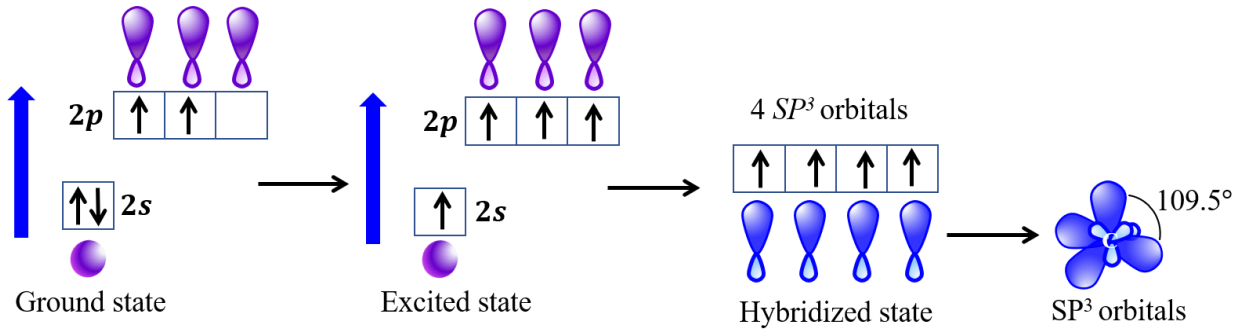

Figure 1.12: Schematic representation of energy levels of carbon and sp^3 hybridized orbitals.

Depending on the hybridization, C can bond to the other elements of the compound via three types of bonds: single, double and triple. Single bonds are the sigma (σ) bonds, which are formed by the head-on overlapping between the two sp^3 hybridized orbitals. The side-by-side overlap between two 2*p* orbitals from each C form a pi (π) bond. A double bond consists of one σ and one π bond. In a triple bond there is one σ and two π bonds. σ bonds are strongly localized whereas π bonds delocalized. In organic materials, the movement of electrons

depends on the delocalization of the electrons in the chemical bonds. The material will behave like an insulator if all the C atoms are bonded via σ bonds as all the electrons in the covalent bonds are strongly localized.

1.2.6.2: Advantage of organic semiconductors:

The main advantage of OSCs due to which they attracted interest in the field of spintronics is their potentially long spin relaxation time (τ_s). The spin relaxation time or spin lifetime is given by[7]:

$$\frac{1}{\tau_s} = \frac{1}{\tau_{\uparrow\downarrow}} + \frac{1}{\tau_{\downarrow\uparrow}} \tag{1.21}$$

where $\tau_{\uparrow\downarrow}$ is the spin–flip time which indicates the average time for an up-spin to flip to a down-spin, and $\tau_{\downarrow\uparrow}$ for the reverse one. For preparing a spintronic device, τ_s takes an important role as it sets the time scale as well as length scale for loss of spin polarization. The dominant mechanisms for spin relaxation are spin-orbit coupling (SOC) and hyperfine interaction (HFI). Both are low for OSCs in comparison to other inorganic materials. In the following we will discuss the SOC and HFI.

1.2.6.2.1: Spin-orbit coupling (SOC):

Spin orbit coupling is a relativistic effect which describes the interaction between the spin angular momentum ($\boldsymbol{s}$) and orbital angular momentum ($\boldsymbol{l}$). The electric ($\boldsymbol{E}$) and magnetic field ($\boldsymbol{B}$) generated by an electron in relativistic limit can be written as[62]:

$$\boldsymbol{E} = -\boldsymbol{\nabla} V(r) \tag{1.22}$$

with $V(r) = \frac{ze}{4\pi\epsilon_0 r}$ and $\boldsymbol{p} \times \boldsymbol{r} = \hbar \boldsymbol{l}$. Where, Z is the atomic number and $\boldsymbol{l}$ is the orbital angular momentum.

$$\boldsymbol{B} = -\left(\frac{1}{2mc^2}\right)\boldsymbol{p} \times \boldsymbol{E} = -\frac{\hbar Ze}{8\pi\epsilon_0 c^2 m^2 r^3}\boldsymbol{l} \tag{1.23}$$

Hence, the Hamiltonian for SOC is $H_{SOC} = -\boldsymbol{\mu_s}.\boldsymbol{B} = \frac{\hbar^2 e^2 Z}{8\pi\epsilon_0 c^2 m^2 r^3}\boldsymbol{s}.\boldsymbol{l}$. Now $\frac{1}{r^3}$ is proportional to Z^3. Therefore, SOC is directly proportional to Z^4. As OSCs mostly contain low Z elements (like C and H), usually SOC is small for the OSCs. However, due to the curvature of certain OSCs, the SOC may be enhanced in OSCs.[39]

1.2.6.2.2: Hyperfine interaction (HFI):

Hyperfine interaction arises due to the interaction between the electron spin and the nucleus. If the electron spin interacts with N nuclear spins, the Hamiltonian for the electron-nuclear coupling is given by:

$$H_{HFI} = \sum_{i}^{N} A_i \boldsymbol{I_i}.\boldsymbol{S} \tag{1.24}$$

Where, A_i is the coupling constant, $\boldsymbol{I_i}$ and $\boldsymbol{S}$ is the spin operator for nucleus *i* and electrons. The electron-nuclear spin interaction and fluctuation affect the spin relaxation time and spin dephasing.[7] HFI is weaker for more electron-nuclear interaction as the fluctuation depends on $\frac{1}{\sqrt{N}}$. Therefore, HFI is stronger for hydrogen (H) than other elements. OSCs are conjugated molecules and there is no overlap between C and H. Hence, in OSCs, HFI is comparatively small. Organic molecules without having H atoms (C_{60}, C_{70}, etc.) show negligible HFI.

1.2.6.3: Spin polarized interface: spinterface

Metal/organic interface plays an important role in injecting spin into the OSC. When a FM comes into contact with an OSC layer at the interface a new hybrid electronic state can be formed. This hybrid interface is called as 'spinterface'.[30] Figure 1.13 (a) shows the schematic representation of spinterface. At the interface, organic molecules interact with the FM surface and this may occur either due to a weak 'physisorption' or a strong 'chemisorption'.[63] Physisorption occurs due to a weak Van-der-Waals like interaction between the inert metallic surface and the organic molecules. However, in the case of chemisorption, a strong charge

transfer and orbital hybridization (i.e., mixing of charge and energy) happen at the FM/OSC interface.[63] Sanvito et al. have shown that due to the formation of spinterface, the DOS of an OSC is modified strongly.[30] Figure 1.13 shows the DOS of a FM and an OSC when (b) they are well separated and (c) they are brought into contact. As long as there is no contact, the overall DOS is the superposition of the individual DOS, i.e., spin polarized DOS of the FM and discrete energy levels for the OSC. Here the current spin polarization only depends on the DOS of the FM. When the OSC is brought into contact with a FM, there is a broadening in the DOS of the OSC. The spin up and spin down energy levels of the OSC are broadened by different amounts because of the energy offset in the spin up and spin down bands in FM.

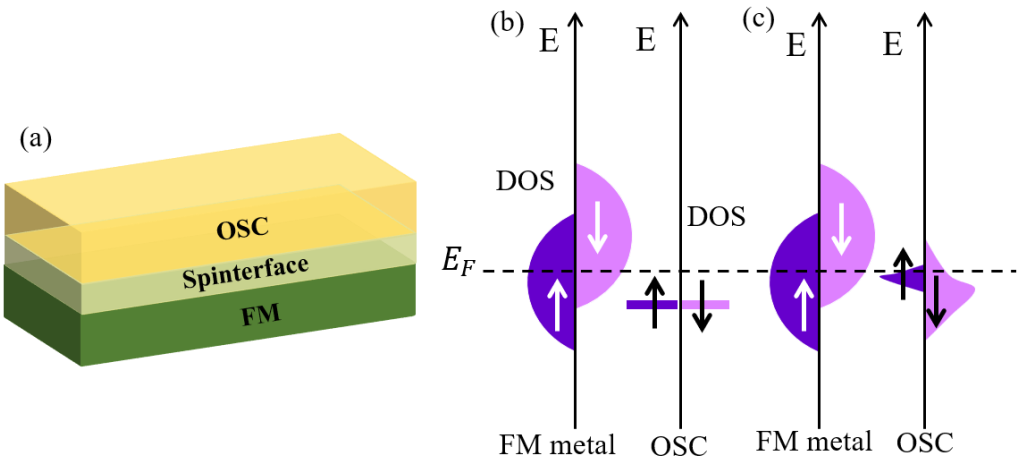

Figure 1.13: (a) Schematic of formation of spinterface at FM/OSC interface. Schematic representation of DOS of a FM and an OSC when they are (b) well separated and (c) brought contact to each other. The figures (b) and (c) are modified figures shown by Sanvito et al.[30]

The spinterface has also significant effect in the metal side. It has been observed that deposition of a OSC layer on top of a FM thin films modify the anisotropy of the system.[33–36,64] Deposition of a C_{60} layer can modify the anisotropy of an ultrathin Co layer from in-plane to out of plane.[36,64] A reduction of magnetic moment in Fe layer has been observed due to the absorption of C_{60} at Fe/C_{60} interface.[33] It has been reported that deposition of C_{60} layer on top of a diamagnetic Cu or paramagnetic Mn can modify the DOS of both the metal and emergent ferromagnetism can be observed.[37,38]

The formation of spinterface opens a wide selection of potentiality for a new class of spintronic devices. In spin valves, depending on the FM/OSC, an enhanced or inverted spin-polarization occurs at the interface which makes the spinterface efficient for use in spintronic devices. However, the mechanism behind the spin transport at the FM/OSC interface is still not understood well. Also, the effect of such hybridized spinterfaces on the magnetic properties such as magnetic domains, magnetization reversal, damping etc. need to studied systematically.

1.2.7: Spin to charge conversion

1.2.7.1: Spin current:

Spin current is a flow of electron spins like charge current (flow of charge of electrons) and it has an important role in the field of spintronics. An electric current can be calculated as $j_c = -e(v_\uparrow + v_\downarrow) = -e(\frac{\partial E}{\partial A_\uparrow} + \frac{\partial E}{\partial A_\downarrow})$, where $v_\sigma(\sigma = \uparrow, \downarrow)$, $A_\sigma(\sigma = \uparrow, \downarrow)$ and $E\ (A_\uparrow,\ A_\downarrow)$ are the velocity operator, vector potential and energy eigenvalues, respectively.[65,66] j_c is independent of spin ($v\uparrow = v\downarrow$) as the vector potential for an electromagnetic field is independent of spin ($A_\uparrow = A_\downarrow$). Therefore, we have only charge current but no spin current (figure 1.14 (a)).

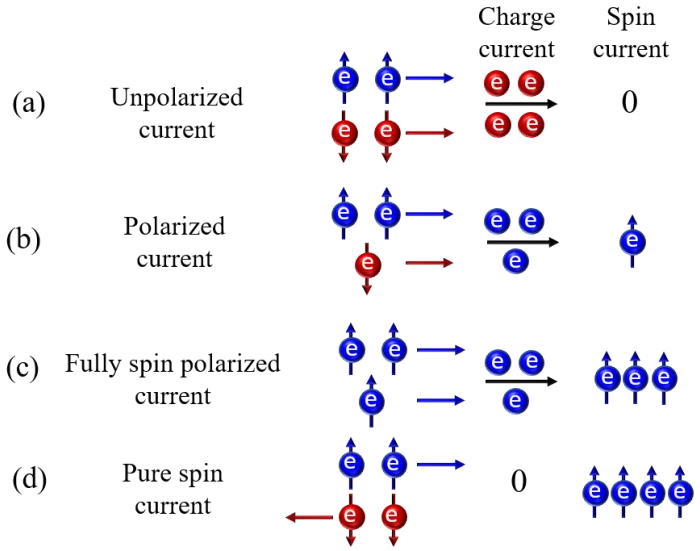

Figure 1.14: Schematic representation of (a) unpolarized current, (b) spin polarized current, (c) fully spin polarized current and (d) pure spin current. The idea of the figure has been taken from Reference [66].[66]

If the vector potential is spin-dependent (i.e., $A_\uparrow \neq A_\downarrow$), there is high probability that the system will circulate spin current. When the velocities of electrons are $v\uparrow = -v\downarrow$, there is no charge current (i.e., $j_c = 0$) and $(v\uparrow - v\downarrow) \neq 0$ (figure 1.14 (d)). This nonzero quantity is relevant to the collective motion of electron spin and known as pure spin current. The spin current is defined as $j_S = \frac{\hbar}{2}(v_\uparrow - v_\downarrow)$.

1.2.7.2: Spin pumping:

When a NM metal or semiconductor layer comes in contact to any FM layer, a pure spin current I_s^{pump} is pumped into the NM layer under ferromagnetic resonance conditions. This process is known as spin pumping. The dissipation of spin angular momentum from FM to NM layer causes linewidth boarding of the ferromagnetic resonance which gives information about the spin injection efficiency across the FM/NM interface. Figure 1.15 shows the schematic representation of injection of pure spin current $\boldsymbol{I}_s^{pump}$ from FM to NM layer via spin pumping. The I_s^{pump} injected into a NM layer is given by[67–69]:

$$\boldsymbol{I}_s^{pump} = \frac{\hbar}{4\pi}\left(A_r \boldsymbol{m} \times \frac{d\boldsymbol{m}}{dt} - A_i \frac{d\boldsymbol{m}}{dt}\right) \tag{1.25}$$

where, $A \equiv A_r + iA_i$ is spin pumping conductance, $\boldsymbol{m}$ and $\hbar$ represent the magnetization direction and Plank's constant, respectively. When the thickness of the FM layer is larger than ferromagnetic coherence length the above equation can be written as[67,69]:

$$\boldsymbol{I}_s^{pump} = \frac{\hbar}{4\pi} g_r^{\uparrow\downarrow} \boldsymbol{m} \times \frac{d\boldsymbol{m}}{dt} \tag{1.26}$$

where, $g_r^{\uparrow\downarrow}$is the real part of the spin mixing conductance.

Spin mixing conductance determine the efficiency of spin transport across the NM/FM interfaces. The spin current injected from FM to NM layer is controlled by the spin mixing conductance. However, if the NM layer thickness is larger than its spin diffusion length (λ_s), near the FM/NM interface a spin accumulation ($\boldsymbol{\mu_s} = \boldsymbol{\mu}_\uparrow - \boldsymbol{\mu}_\downarrow$) occurs in NM. This spin accumulation results in a back flow of spin current, which is defined as[67,69]:

$$\boldsymbol{I_s^{back}} = \frac{g_r^{\uparrow\downarrow}}{2\pi N}\,[\,\boldsymbol{\mu_s} - \boldsymbol{m}(\boldsymbol{m}.\boldsymbol{\mu_s})] \tag{1.27}$$

Then the total spin current can be written as: $\boldsymbol{I_s} = \boldsymbol{I_s^{pump}} + \boldsymbol{I_s^{back}}$.

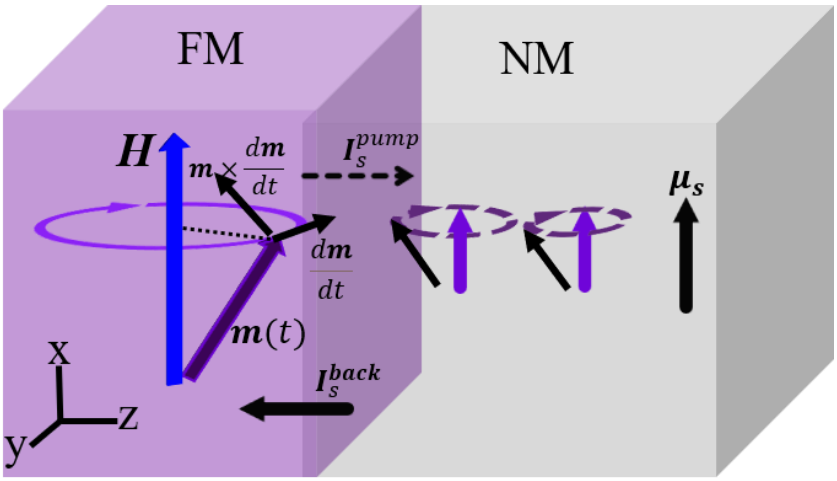

Figure 1.15: Schematic representation of injection of pure spin current $\boldsymbol{I_s^{pump}}$ from FM to NM layer via spin pumping. A spin accumulation ($\boldsymbol{\mu_s}$) may also be arisen in NM layer which drives a spin back flow ($\boldsymbol{I_s^{back}}$) to the FM layer. The idea of the figure has been taken from Reference [69].[69]

1.2.7.3: Spin Hall effect (SHE) and inverse spin Hall effect (ISHE):

The spin Hall effect (SHE) is generated due to the coupling between the charge and spin current because of spin-orbit interaction. When a charge current is flowing along x-axis direction (see figure 1.16 (a)), due to spin dependent scattering spins are accumulated at the edges. Therefore, a net spin current is flowing along the y-axis direction. SHE describes the generation of spin current which is perpendicular to the charge current. The intrinsic SHE depends on SOC effect, whereas skew scattering, side jump scattering are responsible for extrinsic SHE. First experimental detection of SHE is done by Kato et al. using magneto optic Kerr microscopy (MOKE) in GaAs and InGaAs.[70] However, the electrical detection of SHE is not possible due to the equal number of charge distribution at the edges. There is another phenomenon similar to SHE is known as inverse spin Hall effect (ISHE). ISHE is the reverse process of SHE, where

spin current is converted into charge current. Figure 1.16 (b) shows the schematic representation of ISHE. The charge current density ($\boldsymbol{J_c}$) generated by ISHE is given by[71]:

$$\boldsymbol{J_c} = \theta_{SH}(\boldsymbol{J_s} \times \boldsymbol{\sigma}) \tag{1.28}$$

where, $\boldsymbol{J_s}$ is the spin current density, $\boldsymbol{\sigma}$ is Pauli spin matrix and $\theta_{SH} = \frac{J_s}{J_c}$ represents the spin Hall angle (SHA). θ_{SH} of a material shows the spin to charge conversion efficiency.

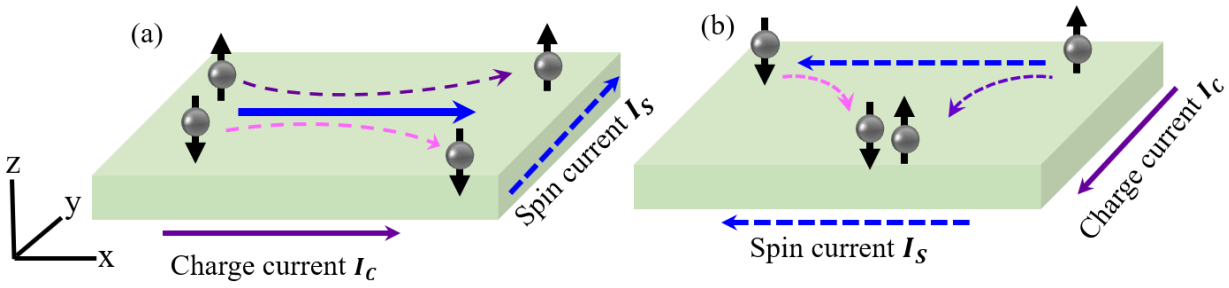

Figure 1.16: Schematic representation of (a) spin Hall effect and (b) inverse spin Hall effect.

CHAPTER 2: Experimental Techniques

In this chapter, the experimental techniques utilized to prepare the thin films and to characterize their structural and magnetic properties have been discussed. We have prepared ferromagnetic thin films of CoFeB and Co using DC magnetron sputtering. Further, bilayers of the FM/C_{60} thin films have been prepared where we have deposited C_{60} using thermal evaporation technique. Structural characterization of these prepared samples has been performed via X-ray reflectivity (XRR) and transmission electron microscopy (TEM) measurements. DC magnetic properties (viz. magnetic moment and saturation magnetization) of the samples have been measured via superconducting quantum interference device (SQUID) magnetometer. Hysteresis loops measurements along with the domain imaging have been performed via magneto-optic Kerr effect (MOKE) based microscopy. Magnetic anisotropy, damping and the inverse spin Hall effect (ISHE) measurements have been performed via ferromagnetic resonance (FMR) spectroscopy. Quantification of the element specific magnetic moment has been performed via X-ray magnetic circular dichroism (XMCD) at ALBA synchrotron light source, Barcelona, Spain.

2.1: Thin film deposition techniques

Various thin film deposition techniques can be covered in two parts: chemical vapour deposition (CVD) and physical vapour deposition (PVD). In both the cases, the deposition of a target material is happening in ultra-vacuum conditions. In CVD process, chemical reactions are taking place between the supplied reagents in gaseous form and the heated substrate surface. But in PVD technique, a solid target material is vapourised and deposited onto the substrate. The main advantage of PVD over the CVD technique is the working temperature. The temperature range for CVD operation is 300 to 900°C which is not suitable for the substrates as it cannot resist such high temperature. In this thesis work different types of PVD techniques have been used to prepare thin film heterostructure.

2.1.1: Sputtering: Sputtering is a PVD method which involves the ejection of atoms from a target material by bombarding highly energetic ions.[59,72] This is a plasma-based technique where gaseous plasma is generated near the target. The positively charged ions from plasma are attracted toward the negatively charged target and the atoms are ejected or sputtered from the target material via momentum transfer. A schematic of a sputtering deposition technique is shown in figure 2.1 (a). In our deposition chamber, Argon (Ar) gas is used to create a plasma. A high negative bias voltage is applied to the target which acts as a cathode. The free electrons get repelled from the negatively charged target and collide with the Ar atoms and create Ar+ ions. These Ar+ ions are attracted towards the target and eject the neutral target atoms by transferring the momentum. The ejected target atoms travel in a solid cone and get deposited on the substrate. A permanent magnet is used just below the target to trap the free electrons. Due to the trapped electrons, a denser plasma is also confined in the vicinity of the target. This process is known as 'magnetron sputtering'.[73]

Magnetron sputtering can be two types, depending on the conductivity of the deposited materials:

DC magnetron sputtering: DC (direct current) magnetron sputtering is one of the simplest methods to deposit a conductive material (i.e., metal). In this process a negative DC field is applied to the target to generate plasma. The negative bias voltage is uniformly distributed to the conductive target and the Ar+ ions become neutralized by momentum transfer. However, this procedure is not possible for the non-conducting insulators. Negative bias voltage cannot be uniformly distributed throughout the target and Ar+ ions are accumulated on the target which results in plasma extinguishment.[74]

RF magnetron sputtering: In this process a RF (radio frequency) power is applied to the target to get rid of the charge accumulation on the target. In the negative half of the RF power, Ar+ ions are attracted towards the target and ejection of target materials resulting in the deposition.

Positive charge accumulation also happens at the same time. During the positive cycle, electrons are attracted to the target and neutralize the positive charges. Therefore, in RF sputtering deposition happens only in one cycle which results in a slow deposition rate.[74]

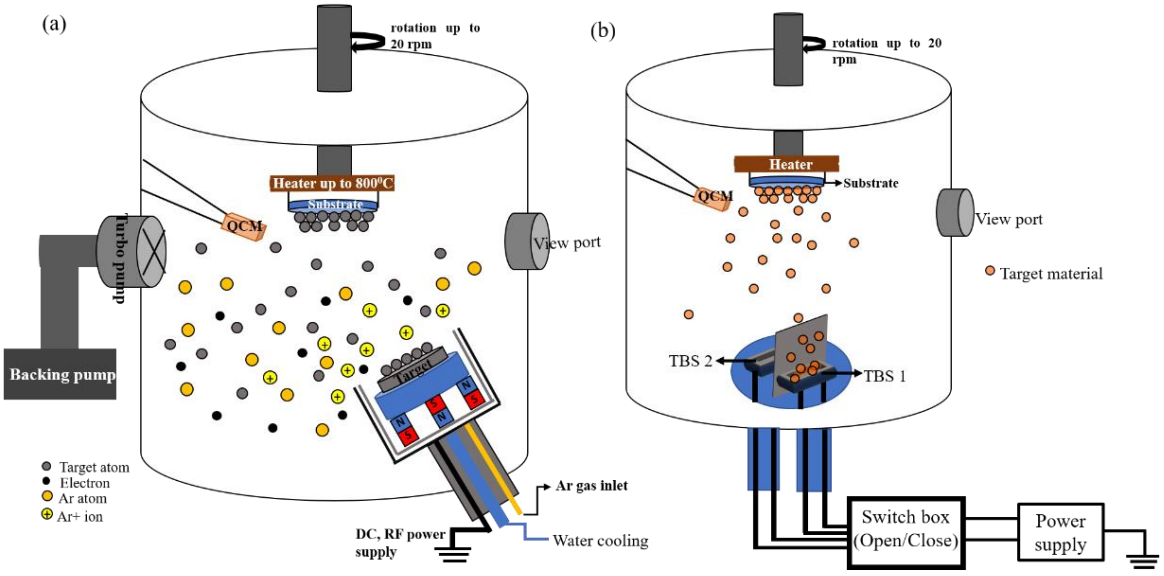

Figure 2.1: (a) A schematic of the sputtering process in a vacuum chamber. The free electrons (black circles) interact with the Ar atoms (dark yellow circles) and create Ar+ ions (light yellow circles). These Ar+ ions hit the target and ejected target atoms (grey circles) by momentum transfer. The ejected target atoms then get deposited on a substrate which is kept in its path of propagation. (b) Thermal evaporation technique in the same vacuum chamber (shown in (a)). TBS 1 and TBS2 represent the thermal boats where the target materials have been kept.

2.1.2: Thermal evaporation: Thermal evaporation is a well-known PVD technique due to its simplicity. In this process, a high current (~100A) is applied to a narrow sheet (known as thermal boat) to heat the target material. After reaching its evaporation point, the material starts evaporating and get deposited on the substrate. A schematic of the thermal evaporation technique is shown in figure 2.1 (b). To deposit the material on the substrate, the mean free path of the evaporated material should be more than the distance between the substrate and the thermal boat. To achieve this, ultra-high vacuum is needed for thermal evaporation.

2.1.3: e- beam evaporation: In this technique a high biased voltage (+2kV) is applied to the target crucible which is placed close to the filament. Applying a sufficient current to the filament, electron emission temperature can be achieved. A stream of electrons (e-beam), emitted from the filament are attracted towards the target crucible. Bombarding the stream of electrons with enough energy to the crucible causes heating which leads to evaporation.[75] Similar to thermal evaporation, a high vacuum is necessary for e-beam evaporation.

We have used a high vacuum multi-deposition system manufactured by Mantis deposition Ltd., UK (shown in figure 2.2 (a)) to prepare the thin film heterostructures. To mount the substrate without breaking the high vacuum, a load lock is attached to the main chamber using a gate valve. The minimum achievable base pressure of the chamber is $5x10^{-10}$ mbar. A QCM (quartz crystal monitor) is used to detect the deposition rate of the materials. During deposition we can rotate the substrate up to 20 rpm and heat it up to 800°C.

This multi-deposition system has the following deposition facilities:

- Five unbalanced magnetron sputtering sources (DC and RF supply).
- Two thermal boat supply (TBS)
- E-beam evaporator having four pockets
- One Nanogen unit
- MAT60

Figure 2.2 (b) represents the schematic of the construction geometry of the deposition system. Thermal evaporation unit is kept at the bottom centre and the other eight sources are at the bottom periphery. All the eight sources are at 45^0 to each other and 30^0 to the substrate normal. This configuration leads to the oblique angle deposition of the materials from the e-beam and the sputtering sources. Due to the oblique angle of deposition, magnetic anisotropy can be induced in the ferromagnetic films.

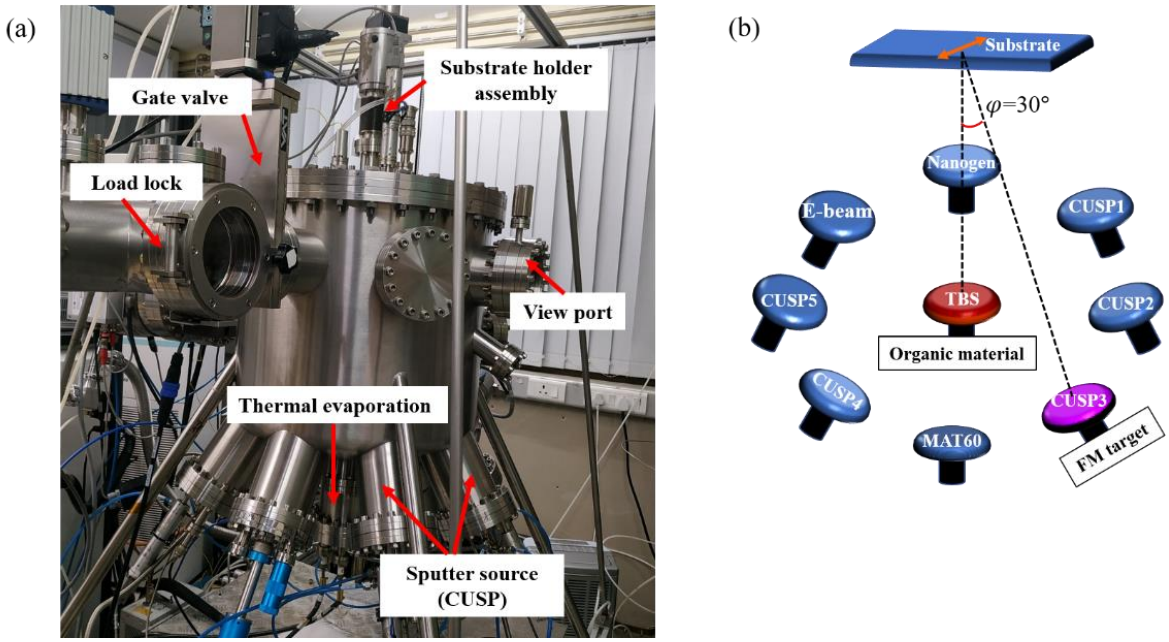

Figure 2.2. (a) An image of a multipurpose high vacuum deposition system manufactured by MANTIS. (b) A schematic representation of the deposition geometry of the system.

2.2: Structural Characterization

2.2.1: X-ray reflectivity (XRR):

X-ray reflectivity (XRR) is one of the valuable techniques to probe characterize the surface structure of a multilayer thin film. The main advantage of XRR is that it can be used for single-crystalline, polycrystalline or amorphous material with a thickness range from 0.1 to 100 nm.[76] In this technique, an x-ray beam is incident on a surface plane at an angle θ_i and reflected from the surface at an angle θ_f. This reflected beam is then detected by a detector placed at an angle $2\theta_i$ with respect to the sample surface. According to the specular reflection geometry $\theta_i = \theta_f$. The momentum transfer vector ($Q_z = k_f - k_i$) is measured along the surface normal and defined as[77]:

$$Q_z = \frac{4\pi}{\lambda} \sin \theta_i \qquad (2.1)$$

where, λ is the wavelength of the incident x-ray beam.

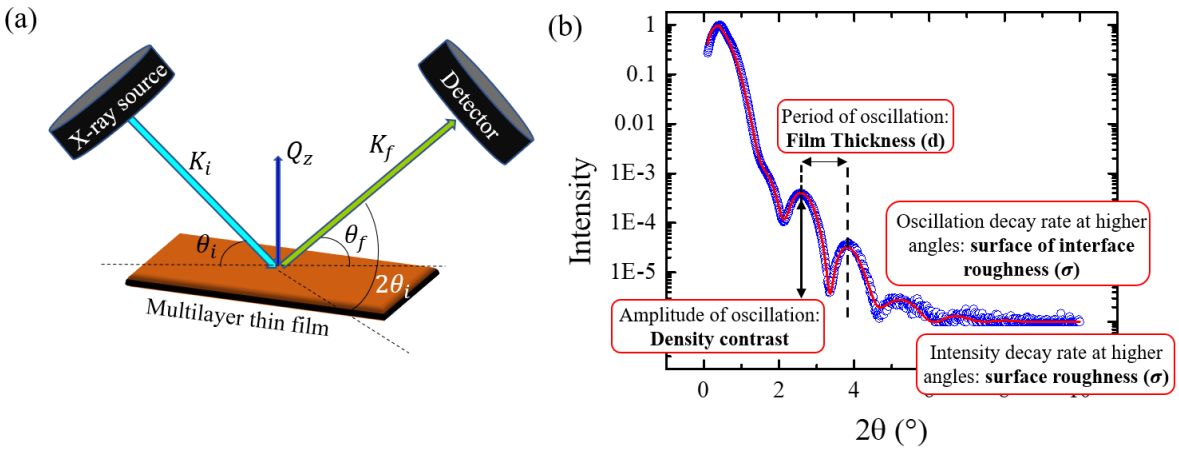

Figure 2.3: (a) A schematic representation of the x-ray reflection technique, where θ_i and θ_f are the incident and reflected x-ray beam, respectively. k_i and k_f are the incident and reflected wave vector, respectively. The momentum transfer vector is denoted as Q_z and measured along the surface normal. (b) A representative x-ray reflectivity curve for the sample Si/CoFeB (5 nm)/MgO and the structural information provided from the reflectivity profile.

A total reflection takes place when an x-ray beam is incident on a sample surface at a grazing angle less than or equal to the critical angle for total reflection (θ_c). With increasing the incident angle θ_i above θ_c, the intensity of the reflected x-ray beam rapidly decreases (shown in figure 2.3 (b)). The refractive index is given by: $n = 1 - \delta + i\beta$; where, $\delta = \frac{\lambda^2}{2\pi}\rho b$ and $\beta = \frac{\lambda}{4\pi}\mu$[77,78]. Here, λ, ρb and μ, are the wavelength of X-ray, scattering length density and linear absorption coefficient, respectively. For an ideal sharp interface, the amplitude of reflectivity of the X-ray can be written using Fresnel's reflectivity formula: $r = \frac{k_z - k\prime_z}{k_z + k\prime_z}$; where, k_z and k'_z are the vertical components of incident and reflected X-ray.

In multilayer thin films where several interfaces are present, the reflectivity of each layer need to be calculated separately. In case of specular reflection from the j[th] and (j+1)[th] layers the reflectivity can be calculated using Parratt formalism: $r_{j,j+1} = \frac{r_{j,j+1} + r_{j+1} e^{2ik_{j+1}d_j}}{1 + r_{j,j+1} r_{j+1} e^{2ik_{j+1}d_j}}$, where d_j is the thickness of the j[th] layer[79]. As the interfaces are not ideally sharp, due to the surface

roughness (σ_j) the reflectivity is damped and can be expressed as $r_{rough_{j,j+1}} = r_{ideal_{j,j+1}} e^{-2k_{z,j}k_{z,j+1}\sigma_j^2}$.[80] Figure 2.3 (b) shows an x-ray reflectivity curve for Si/CoFeB (5 nm)/MgO sample. Oscillations occur due to the interference between the Si substrate, CoFeB and MgO layers. These oscillations are known as Kiessing fringes and depend on the thickness of the film. If the thickness of the film is high the period of oscillation is low. The density of the film can be obtained from the critical angle for total reflection and the amplitude of the oscillation. The amplitude of the oscillation is high if the density of the film largely differs from the substrate. The intensity decay rate at higher angle provides the information of surface roughness while the oscillation decay rate provides the interface roughness. XRR measurements have been performed on all the thin film heterostructure samples to evaluate the thickness and roughness of each layer. All the measurements have been performed using the SmartLab X-ray diffractometer manufactured by Rigaku equipped with a Cu K_α X-ray source having a wavelength of 1.54 Å. The measured data was fitted using GenX software which is based on Parratt formalism[79]. In GenX one simulates the experimental data by putting various parameters such as the thickness, roughness, densities of various layers[81].

2.2.2: Transmission electron microscope (TEM)

Transmission electron microscopy (TEM) is a very powerful technique for structural analysis. The basic principle of TEM is similar to an optical microscope but instead of light, a high energy electron beam (up to 300 kV accelerating voltage) has been used here. TEM is mostly used to study the growth of the layer microstructure and analyse the quality of the prepared film. Using scanning transmission electron microscopy - energy dispersive x-ray spectroscopy (STEM - EDS), one can study the composition of the material.

We have performed high resolution cross-sectional TEM imaging using JEOL F200 available at the Centre for Interdisciplinary Sciences (CIS) at NISER. The operative voltage of this instrument is 200 kV and GATAN oneview CMOS camera is used to record the images. For

the compositional analysis STEM-EDS has been performed. To understand the growth (single crystalline, polycrystalline or amorphous) of the layer, we have performed selected area electron diffraction (SAED) on our samples.

2.3: Magnetic Characterization

2.3.1: Superconducting quantum interference device (SQUID) magnetometry:

Superconducting Quantum Interference Device (SQUID) is a highly sensitive magnetometer used to measure ultra-low magnetic fields with the help of superconducting loops. The development of SQUID magnetometry started from the BCS theory of Superconductivity (Bardeen, Cooper, Schrieffer) in early 1960s.[82] The SQUID has the ability to detect any quantities that can be transduced into magnetic flux. It consists of two separate superconductors with thin insulating layers in between to form parallel Josephson junction.[83] The current density depends on the phase shift ($\Delta\varphi$) between the wave functions of the superconductors. Apart from the Josephson junction, this phase shift is additionally affected by total magnetic flux within the ring.

The sample is suspended using a rod and placed between a superconducting detection coil as shown in figure 2.4. The single turn coils at the top and bottom and the double turn coils at the centre detects on the stray field generated by the sample and cancels out the contribution from the external magnetic field. The vibration of the sample creates alternating magnetic flux across the pick-up coils and generates electrical signals in them. The voltage generated is proportional to the magnetic moment of the sample. Any change in the magnetic moment of the sample caused by external magnetic field is detected by the change in voltage generated in the detection circuit (Figure 2.4). We have used the MPMS3 SQUID magnetometer manufactured by Quantum Design, USA. Three different measurement modes can be performed with the MPMS 3. The DC scan mode allows plotting of raw data points (magnetic moment) with variation in constant or sweeping magnetic fields and temperature.

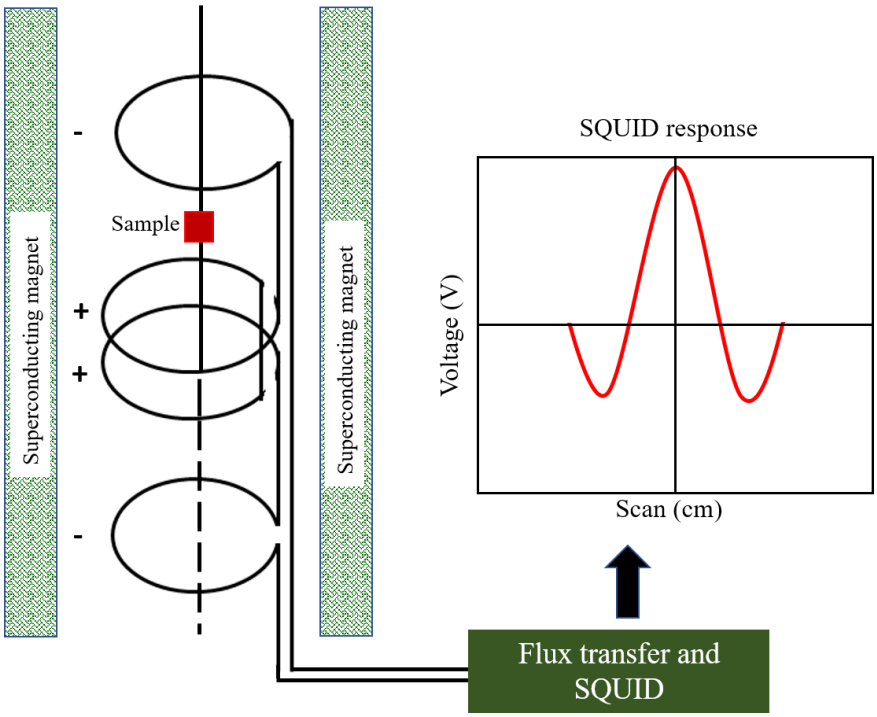

Figure 2.4: A schematic representation of the SQUID with pickup coil. The idea of the image is taken from Reference [84].[84]

The optional VSM (Vibrating Sample Magnetometer) mode provides the ability to measure moment at < 8 x 10^{-8} emu sensitivity (at a maximum field of 7T) with the highly sensitive SQUID sensors operating similar to the VSM methodology. Another mode i.e., AC susceptibility mode uses an oscillating magnetic field and the VSM linear motor to measure the AC susceptibility of a sample. The device is capable of reaching ultra-low temperatures up to a stable 1.8 K which allows to perform low temperature magnetic hysteresis measurements, magnetic moment change as a function of temperature, field cooled hysteresis measurements etc. Ultra-low temperature is achieved by a vacuum insulated chamber filled with a cryogenic liquid helium. A fine-tuned flow impedance allows continuous operation for longer period at 1.8 K. Temperatures up to 400 K is also achieved by heaters installed inside the chamber.

2.3.2: Magneto-optic Kerr effect (MOKE) microscopy

Magneto-optic Kerr effect (MOKE) microscope is used to measure the hysteresis loop along with domain images of a magnetic sample. When a polarized light is incident on a magnetized

surface, the rotation of the plane of polarization of light occurs during the reflection from a reflective magnetized surface. This phenomenon is known as the Kerr effect. MOKE microscopy technique is based on this well-known Kerr effect.[85] This effect is linearly proportional to the magnetization of the sample. Phenomenologically the rotational action of the Kerr effect can be described using dielectric law: $D = \varepsilon E$ where, D is the displacement vector, ε is the asymmetric tensor having the components of the magnetization vector and E is the electric field vector. In magnetic medium, the above relation can be written in the form below[86]:

$$D = \varepsilon(E + iQm \times E) \tag{2.2}$$

where, ε is the regular dielectric constant, m is the magnetization vector and Q is a material parameter which is proportional to the saturation magnetization of the sample that affects the Kerr effect strength. For a magnetic material the dielectric tensor is described as[87]

$$\varepsilon' = \varepsilon \begin{pmatrix} 1 & iQm_z & -iQm_y \\ -iQm_z & 1 & iQm_x \\ iQm_y & -iQm_x & 1 \end{pmatrix} \tag{2.3}$$

Here, $m_x, m_y \; and \; m_z$ are the magnetization components along x, y and z direction, respectively. The asymmetric part of the dielectric tensor only contributes to the magneto-electric effect. The second term in equation 2.2 indicates the gyroelectric nature of the Kerr effect and it is similar to the Lorentz force. The magneto-optical Kerr amplitude (***K***) can be achieved if the Lorentz movement V_{Lor} is projected to the plane perpendicular to the propagation direction of the reflected light wave. ***K*** is perpendicular to the reflected amplitude ***N*** when ***N*** is polarized in the same plane as of the incident light. The polarization vector of the reflected light is rotated by a small angle (θ_K) due to the interference between ***K*** and ***N***. This rotation is known as Kerr rotation and expressed as $\theta_K = \frac{K}{N}$. The Kerr amplitude changes its sign for the domain with opposite magnetization as in this case Lorentz force acts in reverse

direction. A domain contrast is obtained if the reflected light from one type of domain is blocked by the analyzer. The difference in intensities between the bright and dark domains is described as $S \cong 4\beta KN$, where β is the angle between the analyzer and $\boldsymbol{N}$.[86]

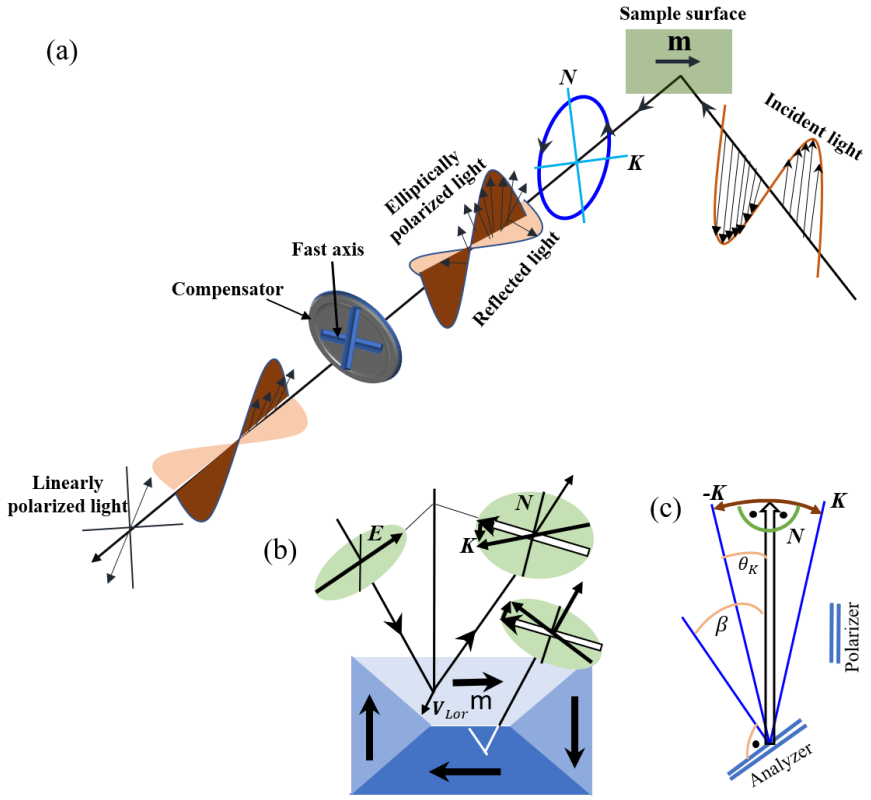

Figure 2.5: (a) A schematic representation of magneto-optical Kerr effect. The incident plane-polarized light become elliptically polarized after reflected from the magnetic sample surface. (b) Elementary magneto-optical interaction for longitudinal MOKE. (c) The orientation of the magneto-optical Kerr amplitude (***K***) and the reflected amplitude (***N)*** with analyzer and polarizer. The idea of the figure has been taken from Reference [86].[86]

Microscopically, MOKE occurs due to the coupling between the electron spin and the electric field of the light in a magnetic medium through the spin-orbit interaction.[87,88] A linearly polarized light can be considered as a sum of left and right circularly polarized light. During propagation through a medium, the electric field of light gives rise to the motion of the electrons in the medium. In absence of an applied magnetic field, the right-circularly polarized electric field will drive the electrons into right circular motion while the left-circularly polarized

electric field will drive the electrons into left circular motion. This results in the same radius of electron orbit for the left and right circular motion. However, when a magnetic field is applied to the propagation direction, a Lorentz force will act on each electron and point toward or away from the circle's centre for the left and right circular motion. Therefore, the radius of the left circular motion will reduce and right circular motion will expand. The difference between the radii of the left and right circular motion will offer different dielectric constant. Hence, the Lorentz force is responsible for the Kerr effect.[88]

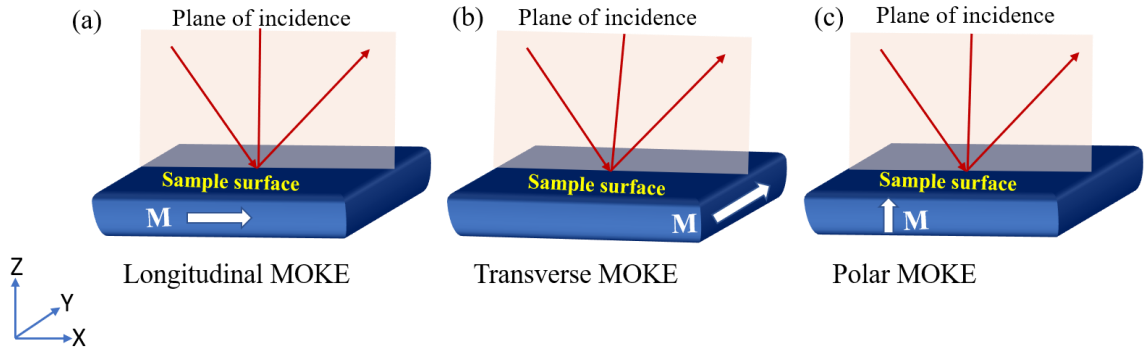

Figure 2.6: Different MOKE measurement geometries (a) Longitudinal MOKE, (b)Transverse MOKE and (c) Polar MOKE.

Depending on the angle between the plane of incidence and the direction of the net magnetization of the sample, MOKE can be sub-divided into three geometries.

Longitudinal MOKE: In this geometry, the direction of the spontaneous magnetization is parallel to both the sample surface and the plane of incidence [figure 2.6.(a)].

Transverse MOKE: In this geometry, the direction of the spontaneous magnetization is parallel to the sample surface but perpendicular to the plane of incidence [figure 2.6.(b)].

Polar MOKE: In this geometry, the direction of the spontaneous magnetization is perpendicular to the sample surface (i.e., out-of-plane) but parallel to the plane of incidence [figure 2.6.(c)].

Figure 2.7 shows the schematic of the Kerr microscopy set up. The light from the LED becomes plane polarized after passing through a polarizer. This plane polarized light is incident on the magnetic sample. For simplicity let us assume the sample has two domain states having

opposite magnetization. The plane polarized light (beams 1 and 2) will rotate in equal and opposite direction after interacting with the opposite magnetizations. Now, if the analyzer is crossed along the one light (say 1), the contrast of the image plane will appear as dark and for the other beam, the contrast will be bright (beam 2).

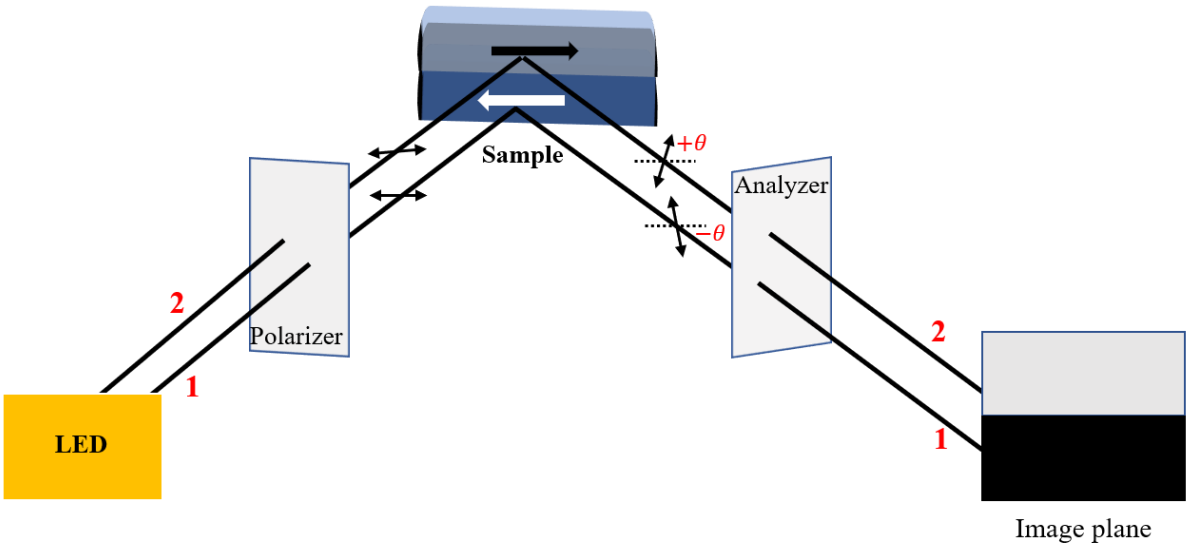

Figure 2.7: A schematic representation of domain formation in Kerr microscopy.

2.3.3: X-ray magnetic circular dichroism (XMCD)

Soft x-ray synchrotron radiation give access to the electronic dipole transitions (core $1s \rightarrow 4p, 2p \rightarrow 3d$) in transition metals and (core $2p \rightarrow 5d, 3d \rightarrow 4f$) in rare-earth elements. In 1975, Stern et al., observed that circularly polarized light can be used to find out information about the spin polarization and spin-orbit splitting.[89] X-ray magnetic circular dichroism (XMCD) is based on the absorption of the core electrons and the circularly polarized light is used to measure the x-ray absorption difference. When a polarized light is incident on a magnetic sample, depending on the orientation of the magnetization, the absorption coefficient also differs based on the helicity of the polarized light. Due to the spin-orbit coupling, $2p$ state is split into two parts $p_{\frac{1}{2}}$ and $p_{\frac{3}{2}}$. For $3d$ transition metal, excited $2p$ core electrons are transited to an unfilled $3d$ state. Transition from $2p_{\frac{1}{2}}$ to $3d_{\frac{3}{2}}$ is known as L_2 edge while $2p_{\frac{3}{2}}$ to $3d_{\frac{3}{2}}$ is known as L_3 edge. Left and right circularly polarized (LCP and RCP) photons will excite the

electrons which have opposite spin polarization. Since $2p_{\frac{1}{2}}(L_2)$ and $2p_{\frac{3}{2}}(L_3)$ have opposite spin orbit coupling ($l - s$ *and* $l + s$, respectively), the spin polarization is also opposite for L_2 and L_3 edges (figure 2.9). XMCD intensity depends on the orientation of the magnetization (**M**) of the magnetic material and the angular moment (**P**) of the polarized photons. Intensity will be maximum when $M||P$**.** The orientation of the intensity can be changed by changing the applied magnetic field or the polarization of the photon. XMCD is advantageous than other techniques as element specific magnetic properties can be characterized using this technique. Using magneto optical sum rule, one can quantify the orbital (L_z) and spin angular momentum (S_z). Most of the XMCD experiments are done using total electron yield (TEY) or total fluorescence yield (TFY) modes which detect the emitted electrons. TEY detection is surface sensitive due to short electron escape depth.[90,91]

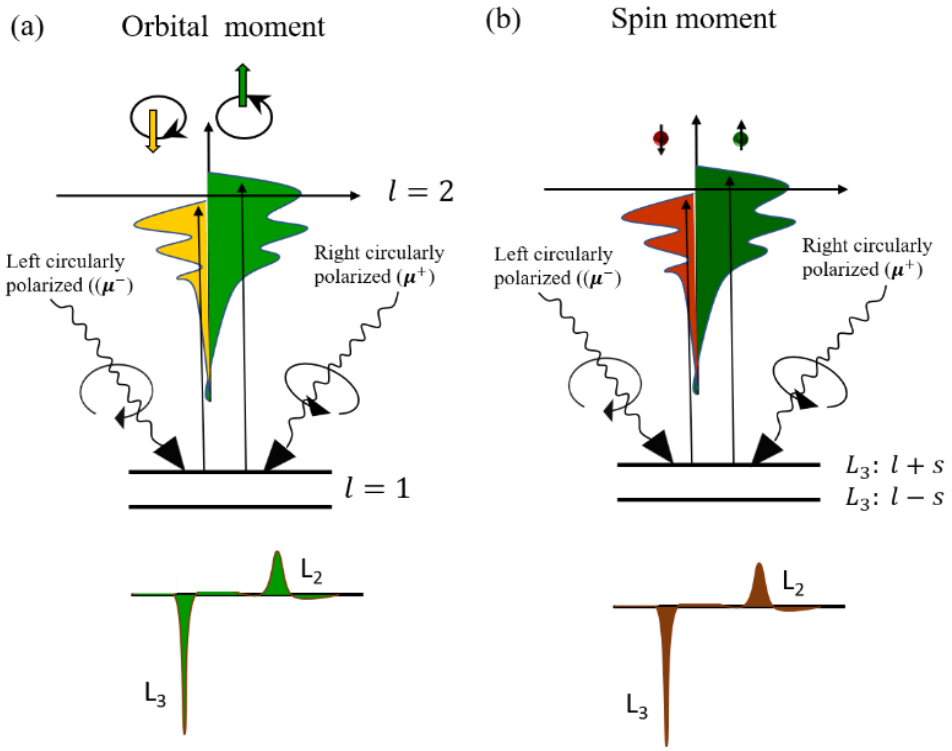

Figure 2.8: XMCD phenomenon in a one-electron model. The transitions occur from 2*p* core shell to unfilled 3*d* states. Using circularly polarized x-rays, (a) the orbital moment and (b) the spin moment can be determined. This figure is motivated by the Reference [92].[92]

Orbital and spin angular momentum can be calculated using the following sum rule formula[92–95]:

$$m_{orb} = -\frac{4\int_{L_3+L_2}(\mu_+ - \mu_-)\,dE}{3\int_{L_3+L_2}(\mu_+ + \mu_-)\,dE}\,(10 - n_{3d}) \tag{2.4}$$

$$m_{spin} = -\frac{6\int_{L_3}(\mu_+ - \mu_-)\,dE - 4\int_{L_3+L_2}(\mu_+ - \mu_-)\,dE}{\int_{L_3+L_2}(\mu_+ + \mu_-)\,dE}\,(10 - n_{3d}) \tag{2.5}$$

Where, m_{orb} and m_{spin} are the orbital and spin magnetic momentum in units of μ_B/atom, respectively. n_{3d} is the 3d electron occupation number of the specified transition metal. L_2 and L_3 denote the integration range. We have calculated the ratio of orbital to spin magnetic moments using the below equation[92]:

$$\frac{m_{orb}}{m_{spin}} = \frac{2\int_{L_3+L_2}(\mu_+ - \mu_-)\,dE}{9\int_{L_3}(\mu_+ - \mu_-)\,dE - 6\int_{L_3+L_2}(\mu_+ - \mu_-)\,dE} \tag{2.6}$$

The XMCD measurements, discussed in this thesis, are performed at BOREAS beamline, ALBA, Barcelona, Spain.[96] The optics layout of the BOREAS beamline is shown in figure 2.9 (a, c) and the end station hector is shown in figure 2.9 (b). The technical specifications of the beamline are the following:

Photon energy range: 80 eV to > 4000 eV

Maximum resolving power: >10000 for 80 – 1500 eV and <5000 for 1500 – 4000 eV

Applied magnetic field range: up to $\pm$ 6 T

Temperature range: 3K to 350 K

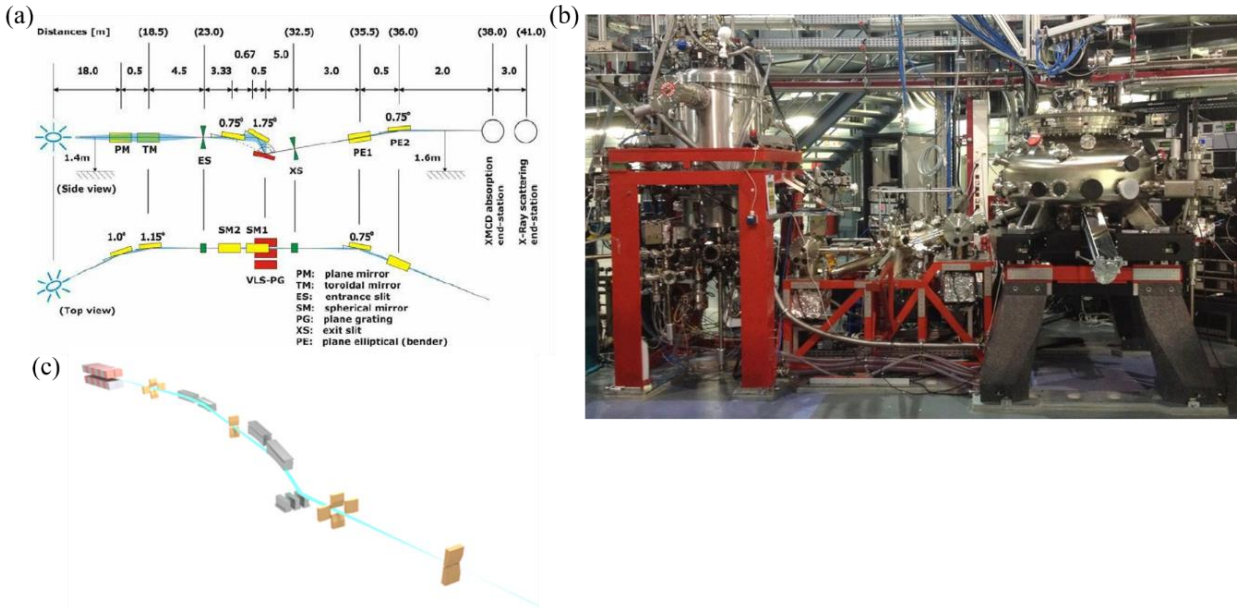

Figure 2.9: Optics layout of BOREAS beamline (a, c). (b) X-ray Absorption Spectroscopy and magnetic circular dichroism end station (Hector).[96]

2.3.4: Ferromagnetic resonance (FMR) spectroscopy:

Ferromagnetic resonance (FMR) technique is commonly used to investigate the dynamic magnetic properties of a ferromagnet.[97,98] If an external magnetic field (H_{ext}) is applied to a ferromagnetic sample, the magnetization of the sample will align along the direction of the applied H_{ext}. Appling a small perturbation (h_{rf}) transverse to the applied magnetic field, it is possible to excite the oscillation of the spin. The spins then start precessing around the h_{rf} (shown in figure 2.10 (c)) and continue the precession until it gets back to its equilibrium condition via damping. At resonance condition, the frequency of h_{rf} matches with the spin precessional frequency and the microwave power gets absorbed into the sample. This process can be explained by Zeeman splitting of the energy levels under the application of an external magnetic field. Due to Zeeman splitting the energy level of the free electrons are split into $\pm\frac{1}{2}g\mu_B H$. When a RF field with frequency ν ($where, h\nu = g\mu_B H$) is applied to a ferromagnetic sample, it absorbs the energy to go to the excited level. Since the resonance frequency depends

on the local field, sweeping the H_{ext} by holding the frequency of h_{rf} constant one can get the absorption spectra (figure 2.10 (d)).

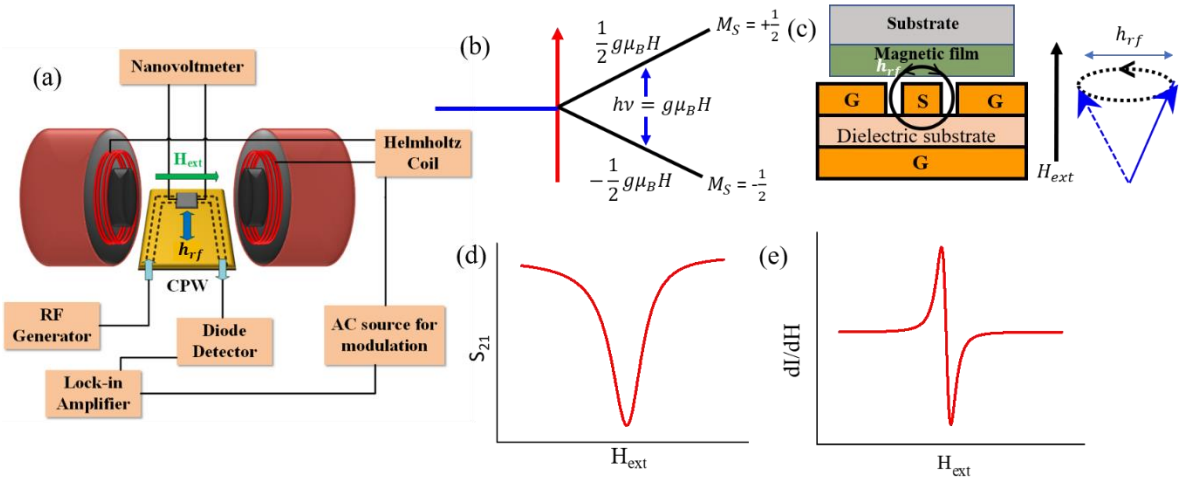

Figure 2.10: (a) Coplanar waveguide based ferromagnetic resonance (CPW-FMR) and inverse spin Hall effect (ISHE) set-up with lock-in detection. (b) A schematic of Zeeman splitting under an external magnetic field. (c) Configuration of a CPW (left side) and schematic of presession of a spin after applying H_{ext}. (d) Absorption spectra (FMR response) and (e) derivative of the FMR response.

Figure 2.10 (a) shows the coplanar waveguide based ferromagnetic resonance (CPW-FMR) set-up with lock-in detection. A schematic of a CPW configuration is shown in figure 2.10 (c). Here, G-S-G represents the ground-signal-ground configuration. During the measurement the sample has been kept on the CPW in a flip chip manner (see figure 2.10. (c)). In CPW-FMR the absorption spectra (FMR response) can be extracted from the transmission coefficient (S_{21}) of the waveguide. In our CPW-FMR set up, a pair of Helmholtz coils is used to generate a small ac signal (490Hz) parallel to H_{ext} and this extra signal modulates the FMR response (S21). A RF diode is used to eliminate the RF part of the signal. After elimination, the signal is detected by a lock-in and the output of the lock-in is the derivative of the FMR response instead of the absorption spectra (figure 2.10 (e)). This FMR derivative consists of both symmetric (A_2) and anti-symmetric (A_1) components and can be fitted using the Lorentzian shape function

$dI/dH = A_1 \frac{4\Delta H(H-H_r)}{[4(H-H_r)^2+\Delta H^2]} - A_2 \frac{\Delta H^2-4(H-H_r)^2}{[4(H-H_r)^2+\Delta H^2]} + offset$. From this fitting linewidth (ΔH), resonance field (H_r) can be achieved[99]. Further, it is possible to measure frequency (f) and angle dependence of H_r by sweeping the frequency and varying the sample w.r.t H_{ext}, respectively. Anisotropy field (H_K) and effective magnetization ($4\pi M_{eff}$) can be obtained by fitting the experimental data using Kittel equation $f = \frac{\gamma}{2\pi}\sqrt{(H_K + H_r)(H_K + H_r + 4\pi M_{eff})}$ where, γ is the gyromagnetic ratio[98].The dynamic magnetic properties like intrinsic damping (α) of the FM material can be evaluated from $\alpha = \Delta H\gamma/4\pi f$ relation.[100] Further, the anisotropy constant can be evaluated from angle dependent H_r data. The detailed discussion about the anisotropy calculations is described in chapter 4.

All the FMR measurements have performed using NanOsc phase FMR. The technical specifications of this CPW-FMR set up are:

Frequency sweep: 2-17 GHz

Magnetic field range: ± 4000 Oe

Microwave power: 11 mW

Further, we have used the same set-up for inverse spin hall effect (ISHE) detection. To measure the ISHE voltage, using silver paste and copper wire, contacts have been made at the two edges of the sample and then connected to a nano-voltmeter (Keithley 2182A) (see figure 2.10. (a)). The detail calculations are discussed in chapter 7.

Chapter 3: Induced magnetism at the interface of Cu and C_{60}

Only few transition metals like Co, Fe and Ni are ferromagnetic at room temperature. Obtaining ferromagnetism without having any ferromagnet is novel as well fascinating from fundamental as well as research point of view. It has been shown by Ma'Mari et al., that it is possible to alter the electronic state of non-magnetic Cu, Pt, Pd, Mn etc. and make them ferromagnetic at NM/C_{60} interface.[37,38] At the interface there is a strong interfacial *p-d* coupling between the 3*d* electrons of metal and π-bonded *p* electrons of C.[37] It has been observed that the charge transfer and surface reconstruction at NM/C_{60} interface can lead to ferromagnetism.[101]

On the one hand the results by Ma'Mari et al., has not been shown by any others and on the other hand, the quantification of the induced magnetic moment and the thickness of spinterface have not been reported yet. In this context, we have prepared Cu/C_{60} multilayers samples to quantify the magnetic moment induced in Cu and the spinterface thickness at Cu/C_{60} interface. We have prepared multilayer Cu/C_{60} thin films on Si/SiO_2 (native) substrate in a multi-deposition high vacuum chamber manufactured by Mantis deposition Ltd. UK.

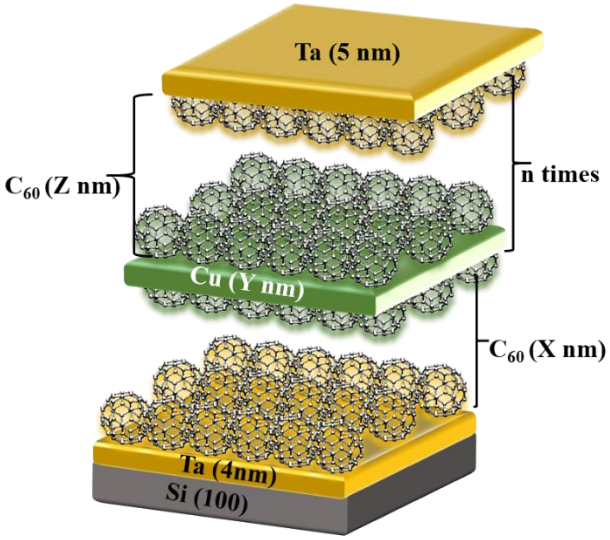

Sample SPC1	X= 16, Y= 2.2, Z= 40, n= 1
Sample SPC2	X= 8, Y= 1.8, Z= 4, n= 1
Sample SPC3	X= 16, Y= 1.8, Z= 8, n= 2

Figure 3.1: Schematic of the sample structure (not to scale).

The base pressure of the deposition chamber was ~ 5×10^{-8} mbar. All the layers have been deposited without breaking the vacuum. Ta and Cu layers are deposited using DC magnetron sputtering and C_{60} layer is deposited via thermal evaporation. Sublimed grade 99.9% pure C_{60}

powder material has been purchased from Sigma Aldrich and we have used this powder material in thermal evaporation without any extra purification. The deposition pressure for Cu and Ta was at 5×10^{-3} mbar, whereas for C_{60} evaporation the chamber pressure was at 1×10^{-7} mbar. The deposition rate of Cu and C_{60} layers were 0.1 and ~ 0.1 – 0.15 Å/s, respectively. For better growth of Cu, a 5 nm thick Ta layer was taken as a seed layer. A capping layer of Ta has been deposited on top of C_{60} to prevent oxidation. The schematic of the sample structure is shown in figure 3.1. The sample details are the following:

Sample SPC1: Si/Ta (4 nm)/C_{60} (16 nm)/ Cu (2.2 nm)/C_{60} (40 nm)/Ta (5 nm),

Sample SPC2: Si/Ta (4 nm)/C_{60} (8 nm)/ Cu (1.8nm)/C_{60} (4nm)/Ta (5 nm),

Sample SPC3: Si/Ta (4 nm)/C_{60}(16 nm)/ [Cu (1.8 nm)/C_{60}(8 nm)]$_2$/Ta (5 nm).

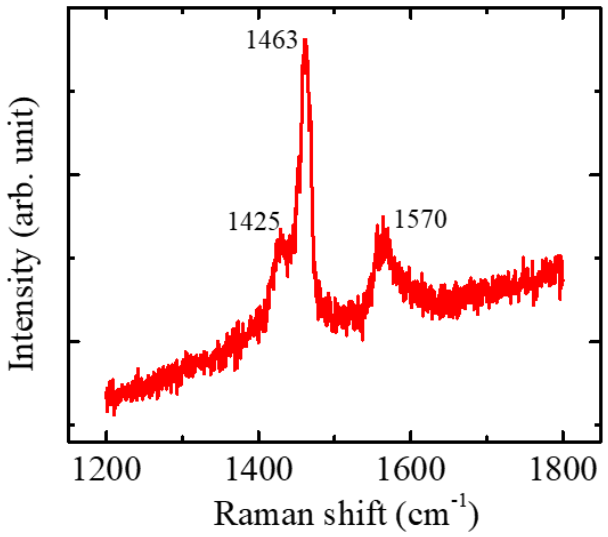

Figure 3.2: Raman spectroscopy data for 20 nm C_{60} thin films.

To confirm the deposition of C_{60} molecules we have performed Raman spectroscopy measurement on single layer C_{60} film. Figure 3.2 shows the Raman spectroscopy data for a 20 nm C_{60} film. Observed Raman shift peaks at 1425, 1463 and 1570 cm-1 confirm the growth of C_{60} molecules.[102,103]

Interface has an important role in inducing magnetism at Cu/C_{60} interface. From the previous report it has been observed that Cu thickness is very crucial and for the thicker Cu layer the

bulk contribution is dominated which quenches the magnetization.[37] It is known that the interdiffusion of metal/OSC interface is higher than that of OSC/metal. Due to the buckyball structure of C_{60}, interdiffusion is expected at Cu/C_{60} interface. It is reported that the Cu-C_{60} interdiffusion might help to transfer the charge from Cu to C_{60}.[104] Therefore, to investigate the quality of interface such as roughness and estimate the interdiffusion between Cu and C_{60}, we have performed x-ray reflectivity (XRR) using X-ray diffractometer manufactured by Rigaku.

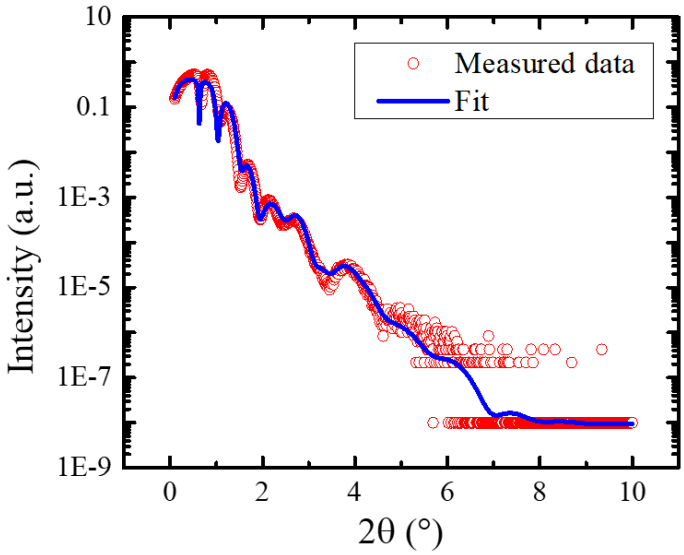

Figure 3.3: X-ray reflectivity data for sample SPC2. The red open circles are the measured data and the blue solid line is the best fit.

We have fitted the experimental data using GenX software.[81] During the fitting we have varied thickness, density and roughness of each layer. The maximum range of the density has been considered as bulk density of the material and minimum density has been chosen as 60% of its bulk value. We have considered the lowest figure of merit (FOM) value as best fit. It has been observed from XRR fitting that interdiffusion is present at both the Cu/C_{60} and C_{60}/Cu interfaces. Figure 3.3 shows the XRR data and best fit for sample SPC2 and the fitted data are shown in table 3.1.

Table 3.1: Parameters obtained from XRR fit

Layer	Thickness (nm)	Roughness (nm)
Ta	5.1	1.2
C_{60}	4.2	0.50
Cu/C_{60} interdiffusion	0.53	0.19
Cu	0.96	0.37
C_{60}/Cu interdiffusion	0.58	0.21
C_{60}	4.8	0.47
Ta	4.3	1.5

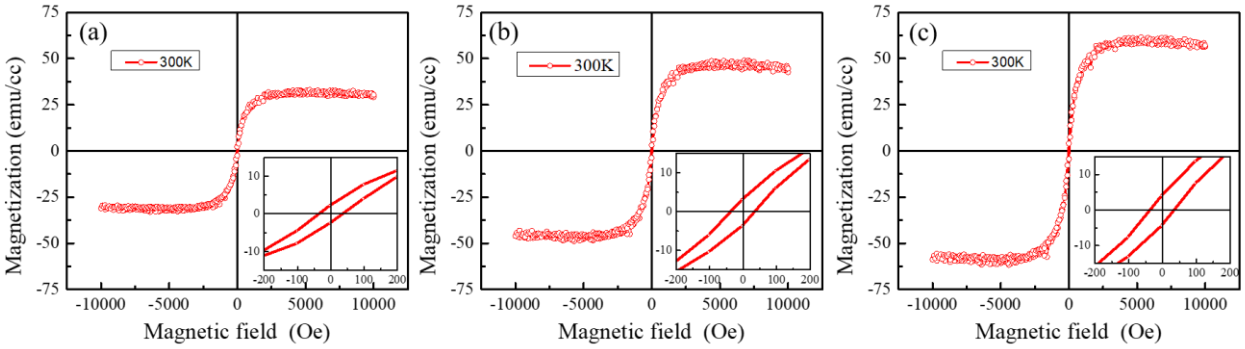

Figure 3.4: Room temperature (300 K) *M-H* loops for samples SPC1 (a), SPC2 (b) and SPC3 (c).

We have performed in-plane *M-H* loop measurements by superconducting quantum interferences device (SQUID) magnetometry (MPMS3) manufactured by Quantum Design, USA. We have used the following formula to correct the background of the Si substrate:

$$m_{film} = m_{Sample} - \frac{m_{Substrate}}{A_{Substrate}} \times A_{Sample} \tag{3.1}$$

where m_{film}, m_{Sample} and $m_{Substrate}$ are the magnetic moment of the thin film, subatrate+film and only substrate, respectively. A_{Sample} and $A_{Substrate}$ represent the area of the sample and the substrate respectively. To calculate the magnetization (shown in Figures 3.4 and 3.5) of the sample we have considered the total thickness of the Cu layer as the exact thickness of magnetic Cu layer is not known.

Figure 3.4 (a - c) show the room temperature (RT) hysteresis loops t for the samples SPC1, SPC2 and SPC3, respectively. It has been observed that all the samples exhibit ferromagnetism at RT even if no FM is present in the sample stack. Further, we have measured the hysteresis loops at low temperature (10 K) for all the samples (shown in figure 3.5 (a) SPC1, (b) SPC2 and (c) SPC3). It has been observed that magnetization increases with decreasing the temperature which is expected. Thermal disorder increases with increase in temperature which oppose the magnetic dipoles to align with the magnetic field, thus resulting in a decrement in the total magnetization. In figure 3.4 and 3.5, we have seen that the magnetization increases with number of Cu/C_{60} interfaces and also it depends on the thickness of the Cu layer. Magnetization of the samples SPC2 and SPC3 are slightly higher (Cu thickness = 1.8 nm) than SPC1 (Cu thickness = 2.2 nm). Also, the magnetization for SPC3 is higher than SPC2, where the greater number of Cu/C_{60} interfaces is present.

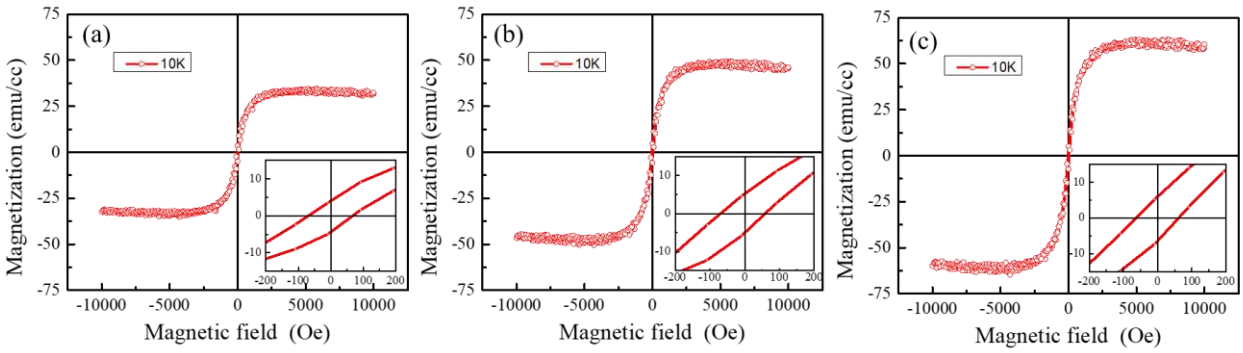

Figure 3.5: *M-H* loops for sample SPC1 (a), SPC2 (b) and SPC3 (c) measured at 10 K.

Angle dependent *M-H* measurements have been performed to investigate the presence of anisotropy in the system. Figure 3.6 show the hysteresis loops measured at 0° and 90° via SQUID magnetometer for sample SPC2 at 10 K (a) and 300 K (b). There is no change in H_C for the hysteresis loop measured at 0° and 90°, which confirms that the samples are isotropic in nature.

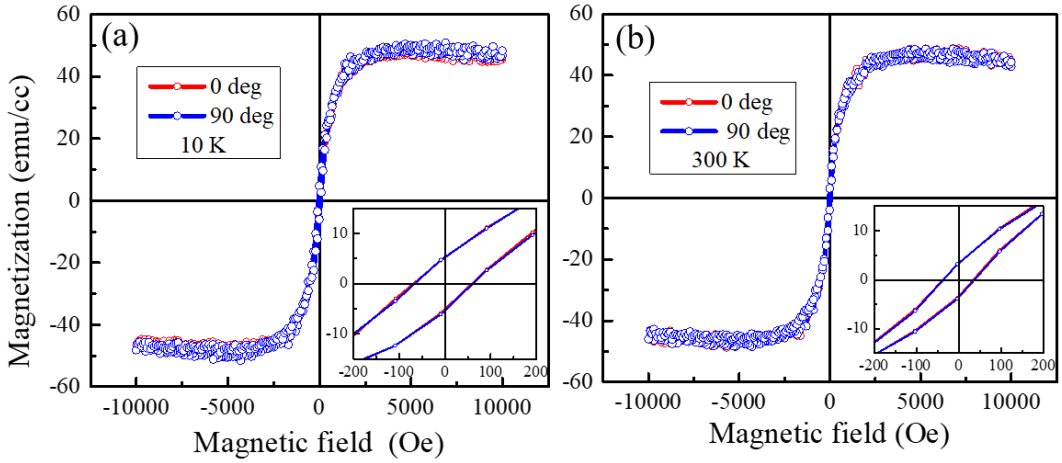

Figure 3.6: *M-H* loops measured at 0^0 and 90^0 via SQUID magnetometer for sample SPC2 at 10 K (a) and 300 K (b).

The induced magnetism observed in Cu/C_{60} samples is probably due to the charge transfer from Cu to C_{60}. Being neutral in charge, neutrons are non-perturbing and non-destructive for the system. The main advantage of using neutron is, it has its own magnetic moment which provides an addition degrees freedom to probe magnetism in multilayers. PNR is a depth selective technique. Using PNR one can calculate the magnetic moment of each layer as well as the thickness of the individual layers. In order to quantify the thickness of the Cu/C_{60} spinterface and the induced magnetic moment we have performed PNR at MARIA reflectometer at FRM II, Garching, Germany.[105] The wavelength (λ) of the neutrons has been chosen to be 6.5 Å. We have measured the momentum transfer (Q_Z) by rotating the sample in a specific angle and keeping the λ constant. We have measure two non-spin flip (NSF) scattering cross sections (R^{++}) and (R^{--}), where the first and second signs represent the polarization of the incident and reflected neutrons, respectively. Figure 3.7 shows the PNR data measured at remanence for samples SPC2 (a) and SPC3 (b). The red and blue lines correspond to the data measured for R^{++} and R^{--} reflectivity, respectively. We are unable to evaluate the magnetic moment from these PNR fits as the magnetic moment induced in Cu at Cu/C_{60}

interface is tiny. Therefore, we aimed to perform XMCD to evaluate element specific magnetic moment.

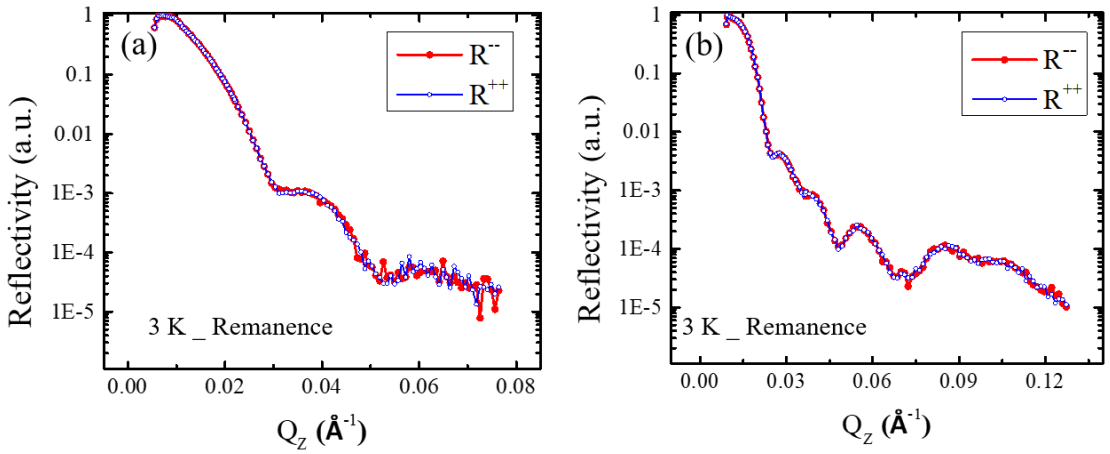

Figure 3.7: Polarized neutron reflectivity (PNR) data measured at 3 K and at remanence for sample SPC2 (a) and SPC3 (b).

In XMCD, circularly polarized light is used to probe the X-ray absorption (XAS) difference under a magnetic field, one taken with right circularly polarized x-rays and the other one with left circularly polarized x-rays. Information on the electronic as well as magnetic properties of the atoms e.g., orbital (*Lz*) and spin angular momentum (*Sz*) can be obtained by analysing the XMCD spectra using magneto-optical sum rules.[92,93,106,107] For 3d transition metals, the excited electrons are transited from 2*p* state to unfilled 3*d* state. Therefore, to obtain the magnetic information of the 3d metals, XMCD experiments are performed at the $L_{2,3}$ absorption edges. To calculate the magnetic moment induced in Cu, we have performed XMCD measurements at the BOREAS beamline at Alba Synchrotron Light Source, E-08290 Barcelona, Spain.[96] Circularly polarized X-rays with energy range 80 – 1500 eV were incident on the samples to excite the 2*p* core electrons of Cu and maximum resolution of $\frac{\Delta E}{E} = 10^{-4}$. The electrons released from the sample via this process were collected as a drain current in total electron yield (TEY) mode. $\pm$ 6 T magnetic field has been applied collinear to the impinging X-rays to saturate the samples. Before starting the experiment, the energy was calibrated with the known

CoO reference. All the measurements were performed under UHV conditions with a base pressure of $\sim 2 \times 10^{-10}$ mbar and at a sample temperature of 1.7 K.

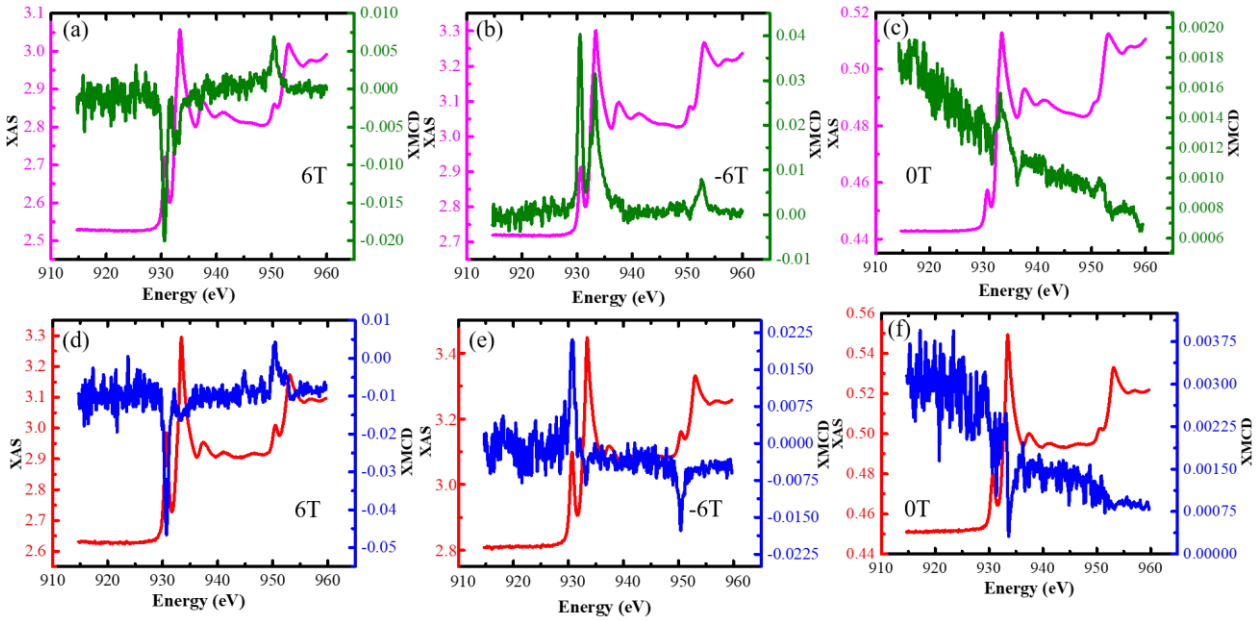

Figure 3.8: XAS and XMCD spectra of the sample SPC2 measured at (a) 6T, (b) -6T and (c) 0T magnetic field at Cu $L_{2,3}$ edges. Similar for the SPC3 at (d) 6T, (e) -6T and (f) 0T. All the measurements were performed at 1.7 K.

Figure 3.8 show the XMCD and XAS spectra for sample SPC2 measured under (a) +6T, (b) -6T and (c) 0T magnetic field. The same for sample SPC3 are shown in figure 3.8 (d) +6T, (e) -6T and (f) 0T magnetic field. It has been observed that applying a negative field the sign of XMCD was changed, which confirms that the measured XMCD signal is not an artifact. Cu L_3 and L_2 edges spectra are observed at 933.4 and 953.06 eV, respectively. There is a XMCD signal coming from the pre-peak at 930.8 eV, which corresponds to Cu_2O. However, we have observed a significant dichroism signal from Cu L_2 and L_3 edges. It has been shown that interface is playing a significant role in inducing magnetism in Cu at Cu/C_{60} interface. Magnetization vanishes after introducing Al or Al_2O_3 layer in between Cu and C_{60} layers.[37] There are few reports on C_{60} induced interface reconstruction for C_{60}/Au (110)[108], C_{60}/Pt (111)[109], C_{60}/Al (111)[110], C_{60}/Ag (100)[111], C_{60}/Ag (111)[112] and C_{60}/Cu (111)[113] systems. In the

reconstructed interface there is vacancy of atoms (metal) and in the vacant place C_{60} can sink. For example, in (4×4) surface structure with 7 atom hole reconstruction means in a $(4 \times 4 = 16)$ unit cell 7 Cu atoms are removed from outermost Cu layer leaving 9 atoms out of 16. So, there is 7 vacancy holes created in the surface and C_{60} molecule is perfectly fitted in the vacant place.[114] Similarly, Yang. et. al has shown that C_{60} adsorption can create 4 atom vacancies at Fe surface.[115] It has been measured that 1-3 electron transfer per C_{60} for reconstructed C_{60}/Cu (111) interface[116] whereas, an unreconstructed interface receives much smaller amount ($< 0.8e^{-}$).[117] The origin of the charge state of C_{60}^{-3} to a reconstructed interface is due to (4×4) 7-atom vacancy in the surface.[114] The possible reason of this induced magnetic moment is hybridization between d_{Cu} and $p_{C_{60}}$ orbitals.[37,38,118,119] Due to the charge transfer and hybridization between Cu and C_{60}, the density of states of Cu is modified and exhibits ferromagnetism at room temperature.

We have calculated the orbital and spin angular momentum using the following sum rule formula[92,93,95,107]:

$$m_{orb} = \frac{-4q(10 - n_{3d})}{3r} \tag{3.2}$$

$$m_{spin\ effective} = \frac{-(6p - 4q)(10 - n_{3d})}{r} \tag{3.3}$$

where, $q = \int_{L_3+L_2}(\mu_+ - \mu_-)dE$, $p = \int_{L_3}(\mu_+ - \mu_-)dE$, $r = \int_{L_3+L_2}(\mu_+ + \mu_-)dE$

m_{orb} and $m_{spin\ effective}$ are the orbital and spin magnetic momentum in units of μ_B/atom, respectively. n_{3d} is the 3d electron occupation number of the specified transition metal. L_2 and L_3 denote the integration range.

Figure 3.9 show $L_{2,3}$ edge XAS and XMCD spectra and their integrations calculated from the spectra for samples SPC2 (a,b) and SPC3 (c,d), respectively. The dotted lines are the integral of the XAS after subtracting two-step-like function from XAS spectra. A two-step function has

been substracted from XAS spectra before the XAS integration to remove all the contributution, called the transition to the continuum, to the XAS that does not come from the

been substracted from XAS spectra before the XAS integration to remove all the contributution, called the transition to the continuum, to the XAS that does not come from the

2*p*-3*d* transition.

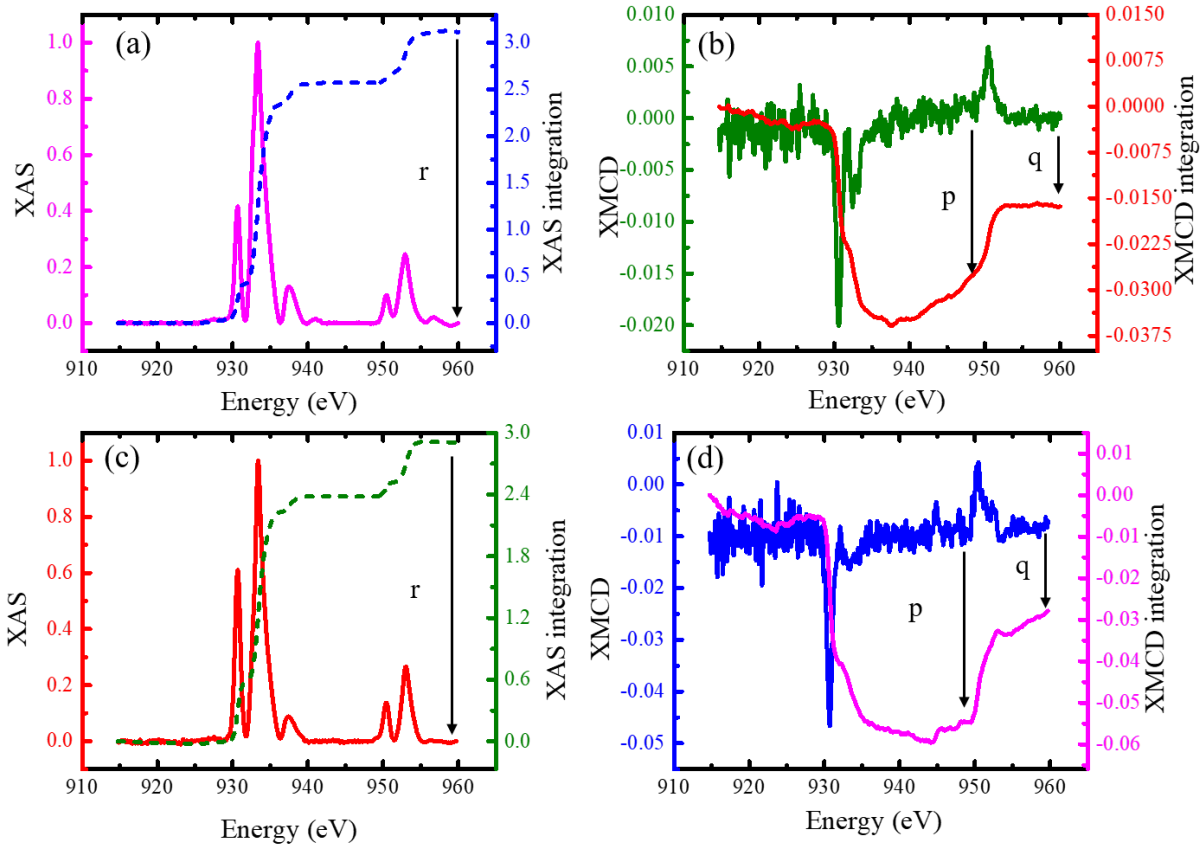

Figure 3.9: $L_{2,3}$ edge XAS and XMCD spectra: The summed XAS and XMCD spectra and their integrations calculated from the spectra are shown for sample SPC2 (a), (b) and SPC3 (c), (d), respectively. The dotted lines are the integral of the XAS spectra after subtracting two-step-like function from XAS spectra. The p, q and r are the three integrals needed in the sum-rule analysis.

The integral for the whole range, L_3 + L_2, can be precisely determined from the integrated spectrum, i.e., the *q* value and the integral for the L_3 edge i.e. the *p* value are shown in figure 3.9. The *r* value is the XAS integral needed in the individual sum rule calculation. The spin

magnetic moment of Cu for samples SPC2 and SPC3 are evaluated to be 0.0078 ± 0.0019 and 0.0116 ± 0.0032 μ_B/atom, respectively. The hole numbers of n_{Cu} has been chosen to be 0.4[120]. With increasing the number of Cu/C_{60} interfaces the magnetic moment of Cu increases. Although paramagnetism in Cu is reported earlier[121,122], the XMCD and SQUID results suggest that a net magnetic moment is induced on the Cu atoms as a consequence of the interaction with the C_{60}. Therefore, the induced magnetism is coming from the Cu/C_{60} interface and not from the metallic Cu.

CHAPTER 4: Effect of C_{60} on magnetic anisotropy and domain structure at CoFeB/C_{60} interface

From this chapter onwards we will discuss the modification of magnetic properties due to the spinterface in FM/OSC system. There are already a few reports on FM/C_{60} bilayer systems, where it has been observed that C_{60} layer can modify the domain size as well as the magnetic anisotropy of the system.[33–35] In epitaxial Fe/C_{60} bilayer system, ~ 2 nm of C_{60} layer become magnetic at the interface and exhibit ~3 μ_B/cage magnetic moment[33]. With introduction of a C_{60} layer, the anisotropy of the system decreases in polycrystalline Fe/C_{60} system,[123] whereas in polycrystalline Co/C_{60} system the anisotropy increases after inserting a C_{60} layer.[35] However, till now there is no such study on spinterface in amorphous CoFeB/C_{60} system. The main advantage of CoFeB is that it is a low damping material. Also, it is amorphous in nature, and it is easy to prepare such amorphous thin films. In this context, we have prepared in-plane anisotropic CoFeB thin film with and without C_{60} layers. We have investigated the magnetic

Table 4.1: Details of the sample structure

Sample name	Sample structure
SPI1	Si/SiO2(native)/CoFeB (5.0 nm)/MgO (2 nm)
SPI2	Si/SiO2(native)/CoFeB (5.0 nm)/C_{60} (1.1 nm)/MgO (2 nm)
SPI3	Si/SiO2(native)/CoFeB (5.0 nm)/C_{60} (2 nm)/MgO (2 nm)
SPI4	Si/SiO2(native)/CoFeB (5.0 nm)/ C_{60} (5 nm)/MgO (2 nm)
SPI5	Si/SiO2(native)/CoFeB (5.0 nm)/ C_{60} (15 nm)/MgO (2 nm)

properties such as magnetization reversal, domain, anisotropy and damping in CoFeB/C_{60} system and compared it with the reference CoFeB sample. All the samples are prepared on

Si/SiO_2(native) substrate. The sample details are listed in table 4.1. CoFeB, C_{60} and MgO layers have been deposited in a multi-deposition high vacuum chamber manufactured by Mantis using DC magnetron sputtering, thermal evaporation, and e-beam evaporation, respectively. The base pressure in the chamber was at ~1×10^{-7} mbar. To avoid oxidation and surface contamination all the layers were deposited without breaking the vacuum. The deposition pressure for CoFeB was at 5×10^{-3} mbar and 1×10^{-7} mbar for C_{60} and MgO evaporation. The CoFeB and C_{60} layers were deposited with the rate of 0.1 and ~ 0.1 – 0.15 $Å s^{-1}$, respectively. A 2 nm of MgO layer was used as a capping layer. C_{60} layer was deposited normal to the substrate whereas CoFeB plume was at 30° w.r.t to the substrate normal due to the chamber's in-built geometry.

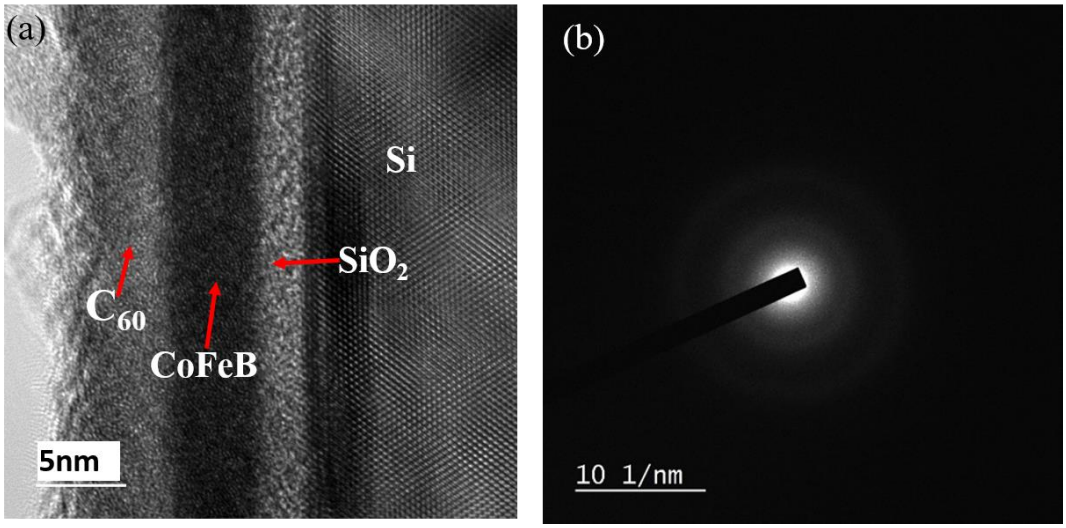

Figure 4.1: (a) High resolution cross-sectional TEM image of SPI4. (b) SAED image of SPI4.

It is reported that the interface has a significant effect on the magnetic properties of the FM/OSC system. To investigate the growth of each layer, we have performed cross-sectional high resolution transmission electron microscopy (HRTEM) and selected area electron diffraction (SAED) using JEOL F200, operating at 200 kV and equipped with a GATAN OneView CMOS camera on sample SPI4. Figure 4.1 (a) shows the HRTEM image of sample SPI4 and all the layers are separately marked. The sharp interface indicates that there is no intermixing present between CoFeB and C_{60}. Figure 4.1 (b) shows SAED image of the sample

SPI4. The diffuse rings in SAED image confirm the amorphous growth of CoFeB and C_{60} layers. For the compositional analysis, scanning transmission electron microscopy-energy dispersive x-ray spectroscopy (STEM-EDS) has been performed. Figure 4.2 (a) shows the region of the sample where the STEM-EDS has been performed. The brighter part in this image indicates the layer of the element having high atomic number (Z). Figure 4.2 (b) represents the element specific mapping for individual layers. EDS line profile and EDS spectra have been shown in figure 4.2 (c) and (d), respectively. In the EDS line profile, it has been observed that the Co and Fe peaks are at the same position which indicates the formation of CoFeB alloy. Further, the EDS spectra shows the presence of C, Mg, O, Fe and Co elements in the sample. Here, we have not properly observed the presence of Boron(B) as it is a lighter atom.

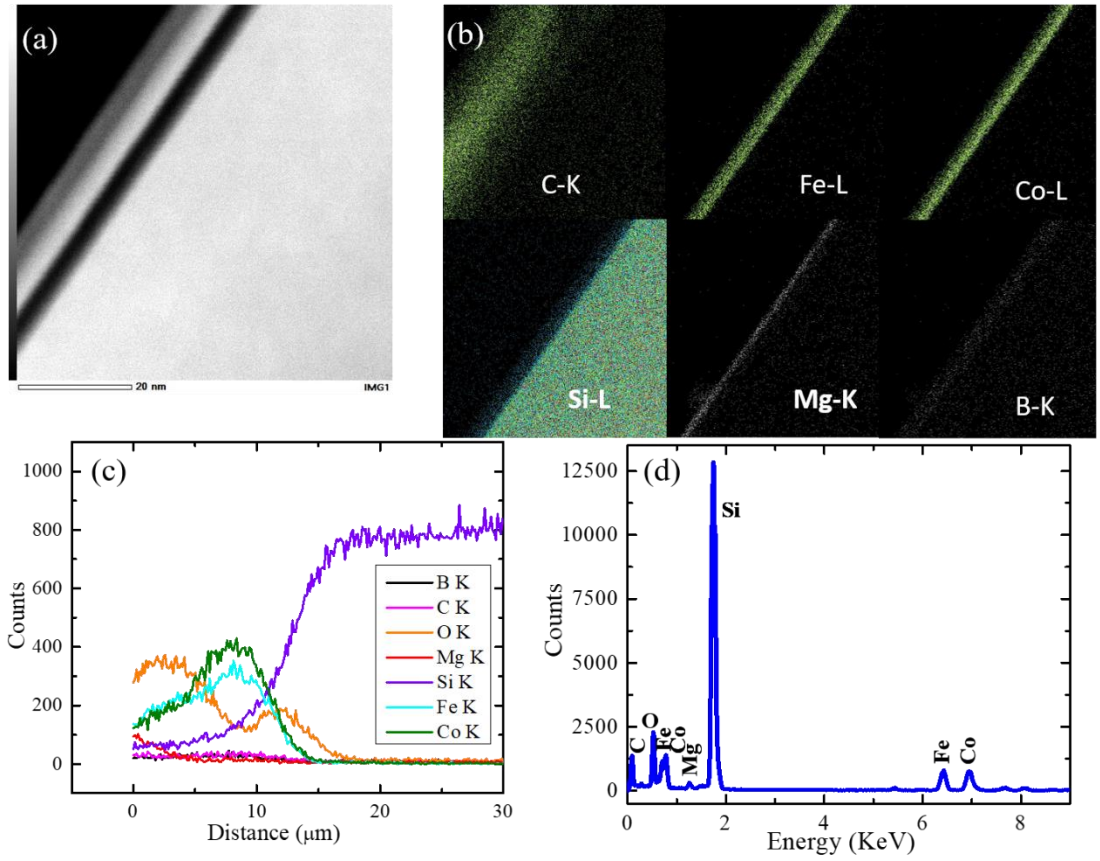

Figure 4.2: (a) The region of the sample SPI4 where the STEM-EDS has been performed. (b) Element specific mapping for each layer. (c) EDS line profile of each element present in the system. (d) EDS spectrum of sample SPI4 showing the presence of different elements.

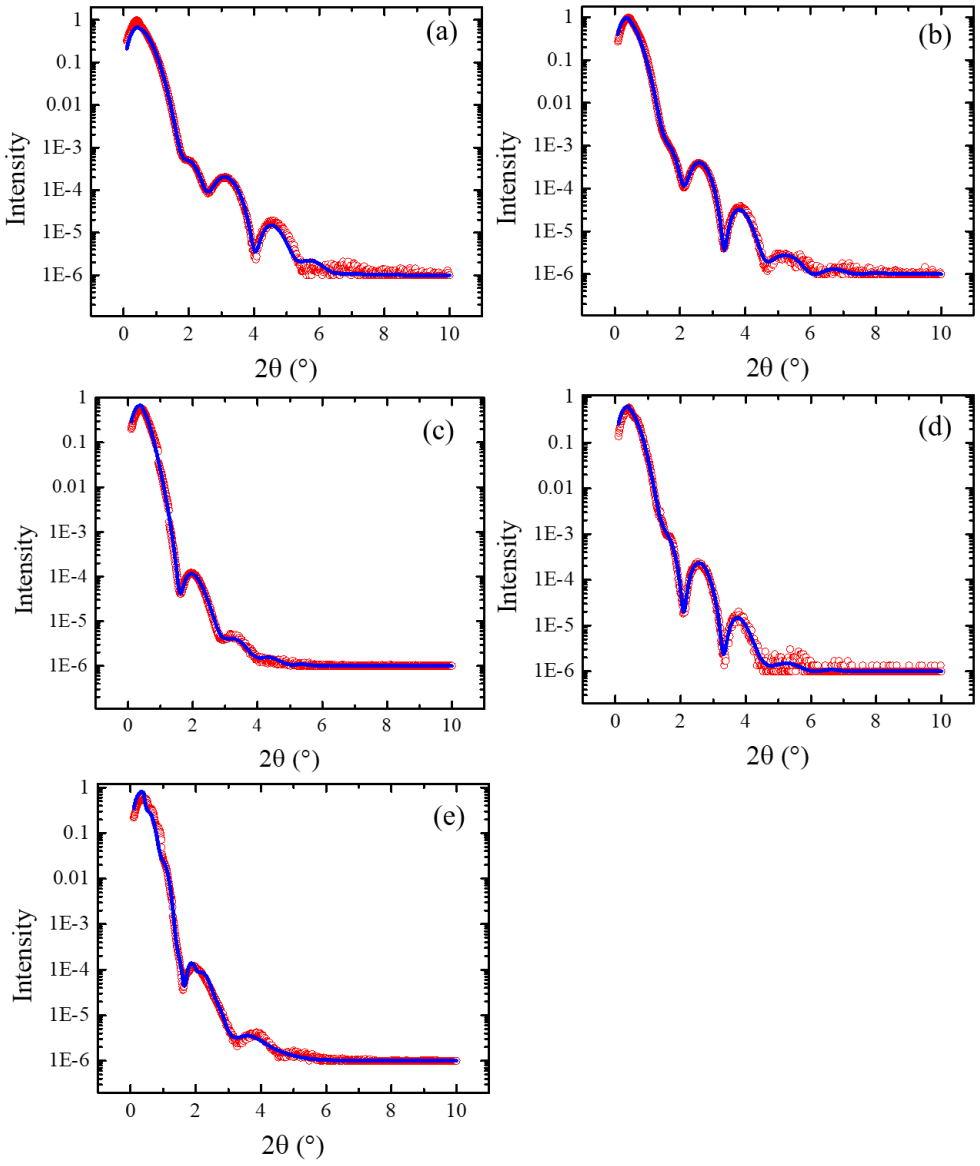

Figure 4.3: XRR data and the best fits for samples SPI1, SPI2, SPI3, SPI4 and SPI5 are shown in (a), (b), (c), (d) and (e), respectively. The red open circles are experimental data, and the blue solid lines represent the best fits.

To obtain the structural information such as thickness (t), roughness (σ), we have performed X-ray reflectivity (XRR) measurements. Figure 4.3 (a-e) show the XRR data and the best fits for samples SPI1, SPI2, SPI3, SPI4 and SPI5, respectively. The experimental data have been fitted using GenX software.[81] Similar to the fitting of figure 3.3 data here also we have varied the thickness, roughness, density of each layer and considered the lowest value of FOM as best fit. As samples (SPI1- SP I5) consist of same type of elements, the density of each layer has

been kept almost the same. The extracted parameters from the fitting have been listed in table 4.2.

Table 4.2: Extracted parameters from the XRR fits

	Sample SPI1		Sample SPI2		Sample SPI3		Sample SPI4		Sample SPI5	
Layers	t (nm)	σ (nm)	t (nm)	σ (nm)	t (nm)	σ (nm)	t (nm)	σ (nm)	t (nm)	σ (nm)
CoFeB	5.50	0.91	5.60	0.93	5.50	0.87	5.00	0.81	5.45	0.96
C_{60}	-	-	1.10	0.20	2.0	0.60	5.02	0.52	15.0	1.80
MgO	1.95	0.61	1.90	0.57	1.80	0.51	2.09	0.76	1.98	0.75

To study the effect of C_{60} on magnetic domains and magnetization reversal, we have performed longitudinal magneto-optic Kerr effect (MOKE) based microscopy. Hysteresis loops have been measured along with domain images for all the samples. All the measurements have been performed at room temperature. Figure 4.3 (a) shows the hysteresis loop measured along the easy axis (EA) of the sample SPI1 (without C_{60}). Domain images at different fields are shown in figure 4.4 (b-f) which are marked in the hysteresis loop of the figure 4.4 (a).

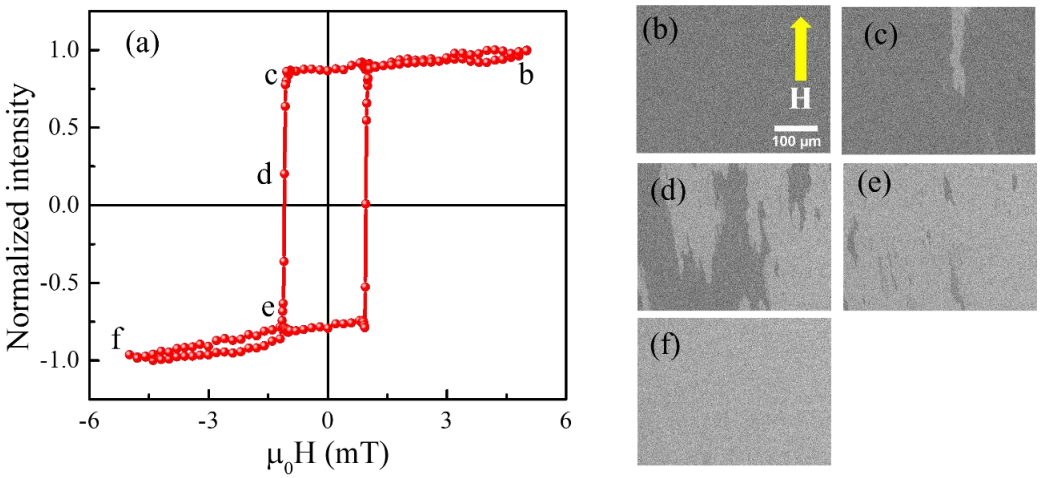

Figure 4.4: (a) Hysteresis loop measured along EA for sample SPI1. (b-f) Domain images captured at different field values, as marked in (a). Scale bar and the magnetic field direction are shown in (b) and same for all the images.

The square shaped loop indicates that along EA the magnetization reversal is happening via domain wall motion. A single jump has been observed between positive to negative saturation, which suggest a 180° domain wall reversal. Domain images shown in figure 4.4 (b-f) show the magnetization reversal from positive saturation state to negative saturation state. Here, light and dark grey represent two negative and positive magnetizations. At positive saturation all the spins are aligned along the applied field direction which produce a single domain state (dark grey (figure 4.4 (b)). As the magnetic field decreases, the image contrast also changes and bright contrast domain appears (figure 4.4 (c) corresponding to the point (c) marked in the hysteresis loop (a)). This dark and light grey region indicate the presence of two different domains. With further decrease in the field the light grey domain expands (figure 4.4 (d)) and reaches to the negative saturation state with complete bright contrast (figure 4.4 (f)). We have performed angle dependent hysteresis loop measurement by varying the angle (ϕ) between the EA and the applied magnetic field. Angle dependent hysteresis loops for samples SPI1, SPI2, SPI4 and SPI5, measured at ϕ = 0°, 30°, 45° and 60° are shown in figure 4.5 (a), (b), (c) and (d), respectively. Figure 4.5 (e) shows the hysteresis loops of the samples measured at ϕ = 90° i.e., the hard axis (HA). Here, red, green, blue, and pink represent samples SPI1, SPI2, SPI4 and SPI5, respectively. It has been noted that along HA the 'S' shaped hysteresis loop has been observed, which indicates that along this axis magnetization reversal happens via coherent rotation. For all the samples, we found that the EA at 0° and HA at 90°, which is expected for uniaxial anisotropic systems. These results show that all the samples exhibit uniaxial anisotropy which we have further confirmed using angle dependent ferromagnetic resonance (FMR) measurements. The EA of the anisotropy lies in-plane and at 90° angle w.r.t the projection of the plume direction. Due to chamber's geometry, CoFeB was deposited at 30° angle w.r.t. the substrate normal. Due to the oblique angle deposition, uniaxial anisotropy induced in the

systems.[35,55,124–130] Domain images captured near coercive field (H_C) at ϕ = 0°, 30°, 45°, 60° and 90° for all the samples are shown in figure 4.6.

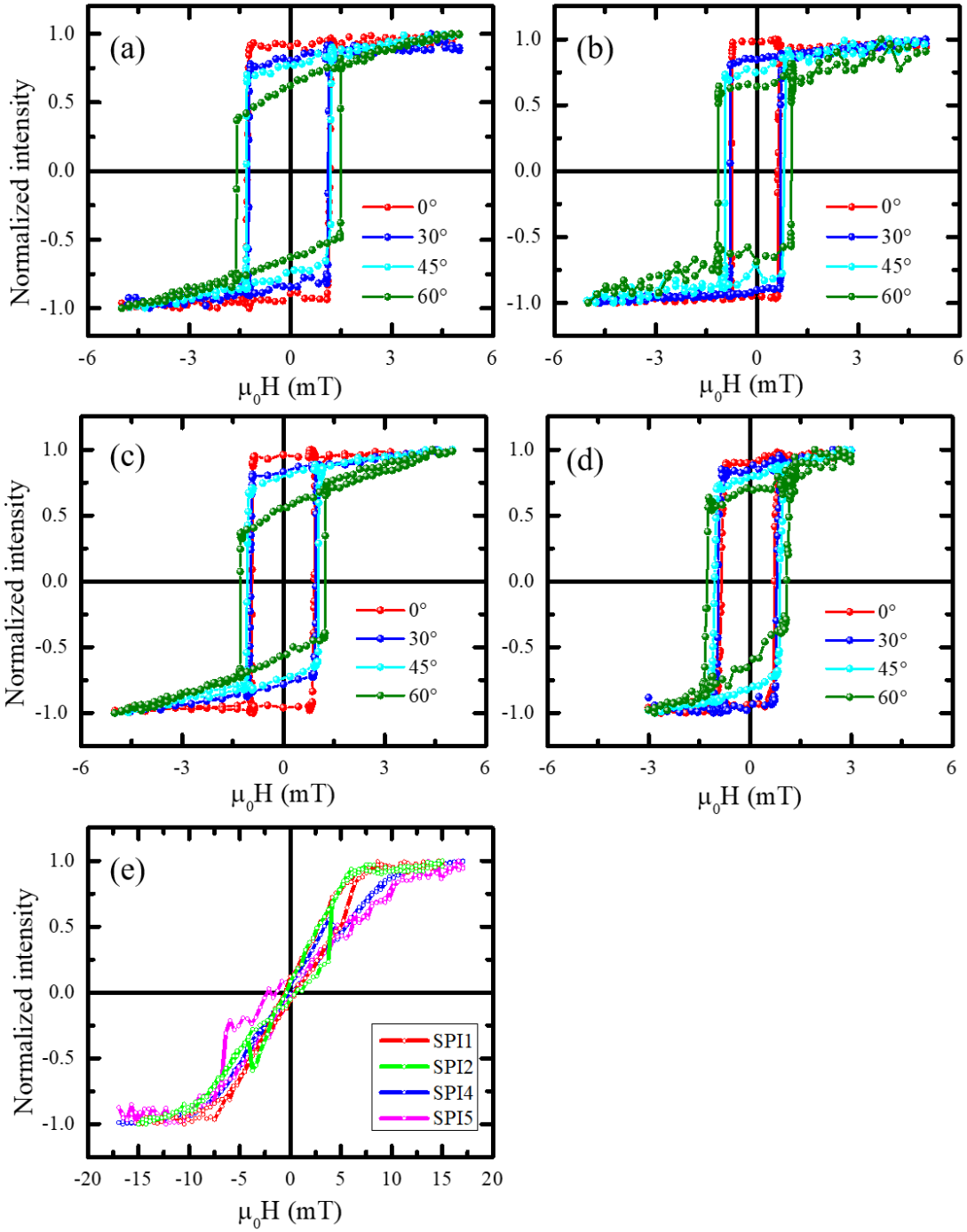

Figure 4.5: Hysteresis loops measured along ϕ = 0°, 30°, 45° and 60° for sample SPI1 (a), SPI2 (b), SPI4 (c) and SPI5 (d). (e) Hysteresis loop along HA (ϕ = 90°) for sample SPI1 (red), SPI2 (green), SPI4 (blue) and SPI5 (pink).

For the samples SPI2 and SPI5, the tilt of the domains is opposite to SPI1 and SPI4. This opposite tilt is due to the anti-clockwise (SPI2 and SPI5) and clockwise (SPI1and SPI4) rotation of the sample stage w.r.t EA during measurement. It should be noted that there is no significant change in the domain structure between CoFeB single layer and CoFeB/C_{60} bilayer samples. In earlier reports on Co/C_{60} and Fe/C_{60}, it has been shown that FM/OSC spinterface has significant effect on domain shape and size.[33–35] In polycrystalline Fe/C_{60} system, the domain size decreased for the bilayers in comparison to the single layer Fe film.[123] However, the domain size increased for the polycrystalline Co/C_{60} bilayers as compared to the single layer Co film.[35] Here, we have considered an amorphous CoFeB system and spinterface has very negligible effect on shape and size of magnetic domains.

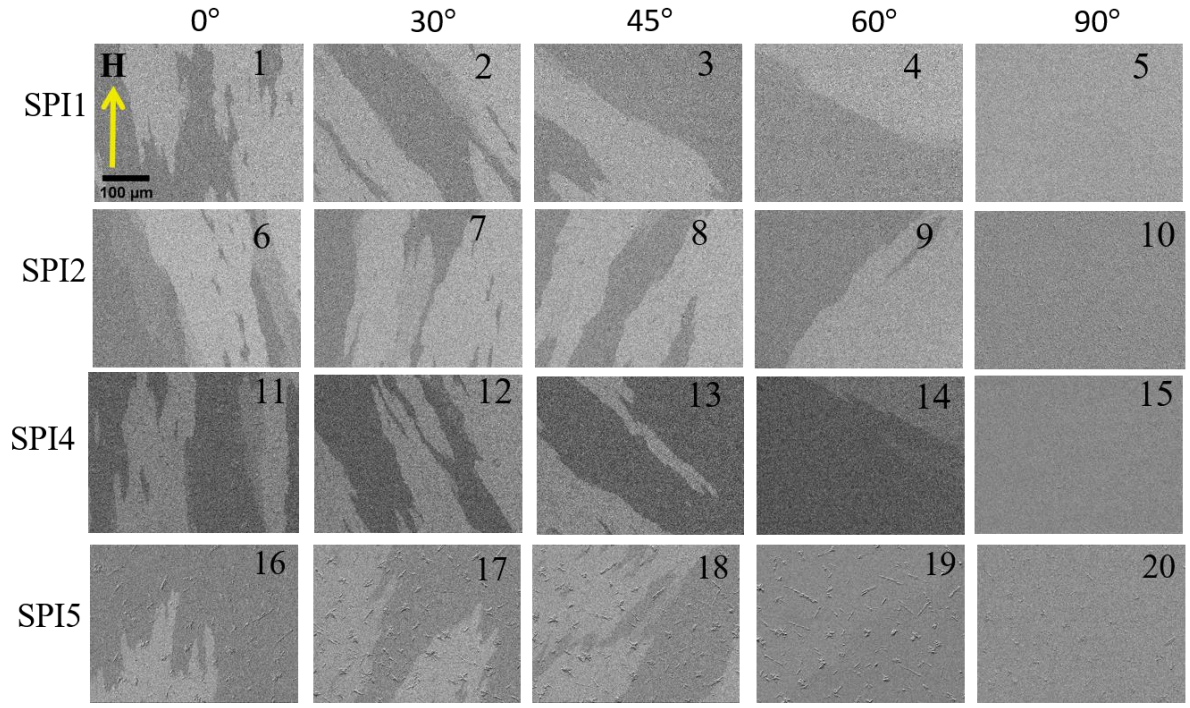

Figure 4.6: Domain images near H_C for samples SPI1, SPI2, SPI4 and SPI5 are shown in (1-5), (6-10), (11-15) and (16-20), respectively. Scale bar and the magnetic field direction are shown in 1 and the same for all the images.

Further, to study the magnetization dynamics we have performed frequency (*f*) dependent FMR measurement in the frequency range 6 to 17 GHz for all the samples. Figure 4.7 (a) shows the

schematic of the direction of applied field (H_{ext}) and RF field (h_{rf}) w.r.t. the sample orientation. Figure 4.7 (b) represents the frequency dependent FMR spectra for sample SPI1. The experimental data has been fitted using a Lorentzian function (Eq. 4.1), where ΔH, H_r, A_1 and A_2 are linewidth, resonance field, anti-symmetric and symmetric components, respectively.[131]

$$FMR\ signal = A_1 \frac{4\Delta H(H - H_r)}{[4(H - H_r)^2 + \Delta H^2]} - A_2 \frac{\Delta H^2 - 4(H - H_r)^2}{[4(H - H_r)^2 + \Delta H^2]} + offset \qquad (4.1)$$

f vs H_r and ΔH vs f plots have been shown in figure 4.8 (a) and (b), respectively, for all the samples. We have calculated the effective damping constant (α_{eff}) by fitting the experimental data using the following equations 4.2 and 4.3.[98,100]

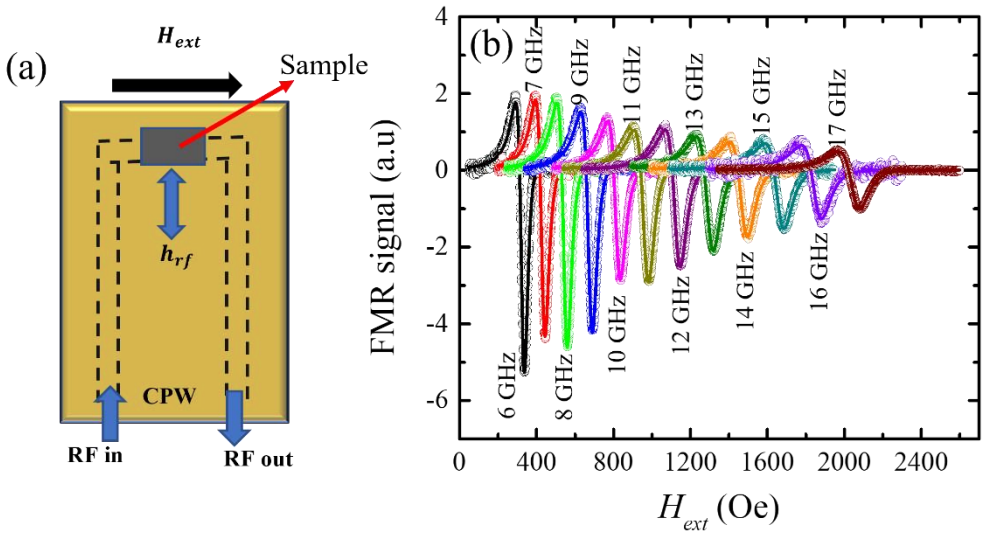

Figure 4.7: (a) Schematic of the FMR set-up and the direction of applied field, rf field direction w.r.t sample orientation. (b) Frequency dependent FMR spectra for sample SPI1 measured in the frequency range 6-17 GHz.

$$f = \frac{\gamma}{2\pi}\sqrt{(H_K + H_r)\left(H_K + H_r + 4\pi M_{eff}\right)} \qquad (4.2)$$

where, gyromagnetic ratio $\gamma = \frac{g\mu_B}{\hbar}$ and g, μ_B, $\hbar$, H_K are Lande-g factor, Bohr magneton, reduced Planck's constant and anisotropy field, respectively.

$$\Delta H = \Delta H_0 + \frac{4\pi\alpha_{eff} f}{\gamma} \qquad (4.3)$$

where, ΔH_0 is the inhomogeneous line width broadening which depends on the magnetic inhomogeneity of the sample.

α_{eff} consists of intrinsic Gilbert damping (α_G), damping affected by interface (α_{int}), magnetic proximity (α_{mp}) and spin pumping (α_{sp}) and it is defined[132]:

$$\alpha_{eff} = \alpha_G + \alpha_{int} + \alpha_{mp} + \alpha_{sp} \tag{4.4}$$

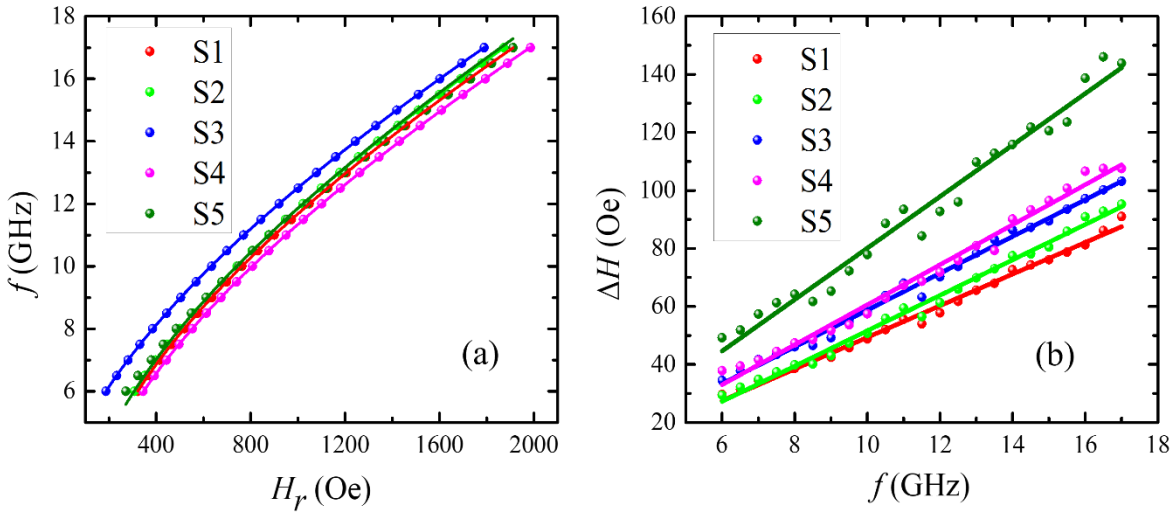

Figure 4.8: (a) f vs H_r and (b) ΔH vs f plots for all the samples. Solid circles represent the experimental data whereas solid lines are the best fits using equation 4.2 and 4.3.

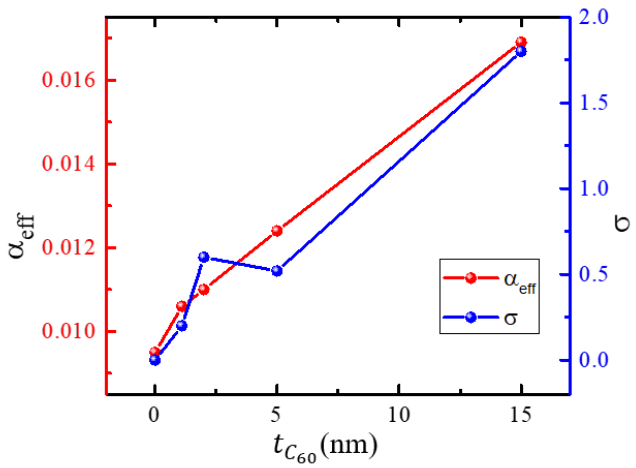

Figure 4.9: C_{60} **t**hickness ($t_{C_{60}}$) dependence of α_{eff} (a) and roughness of C_{60} (σ) (b).

It is difficult to disentangle the individual components. Therefore, the effective damping can only be quantified. The values of α_{eff} for the samples SPI1, SPI2, SPI3, SPI4 and SPI5 are 0.0095±0.0002, 0.0106±0.0002, 0.0110±0.0002, 0.0124±0.0003 and 0.0169±0.0006,

respectively. It has been observed that after introduction of a C_{60} layer, α_{eff} increases and it continuously increases with increase in the thickness of C_{60}. The possible reason behind this increase in α_{eff} might be due to the interface roughness or other effects at the interface such as spin pumping. The detailed discussion on spin pumping at CoFeB/C_{60} has been discussed in chapter 7. C_{60} **t**hickness ($t_{C_{60}}$) dependence of α_{eff} and Roughness of C_{60} have been shown in figure 4.9. It has been observed that the roughness of C_{60} increases with increasing the thickness of C_{60}. As the roughness increases the α_{eff} also increases.

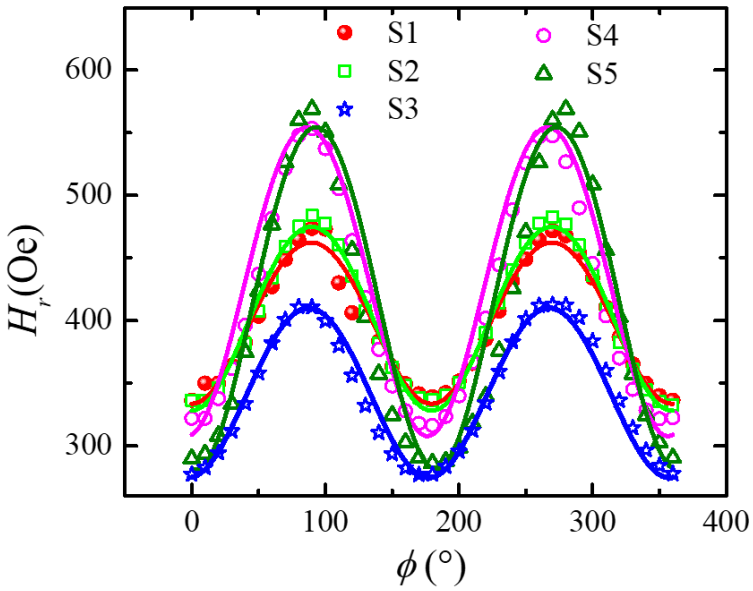

Figure 4.10: Angle dependence of resonance field (H_r) for all the samples. red solid circles, green open squares, blue open stars, pink open circles and green open triangles represent the experimental data for SPI1, SPI2, SPI3, SPI4 and SPI5, respectively, and solid lines are the best fits using equation 4.5.

In order to quantify the anisotropy of the system and study the anisotropy symmetry, we have performed angle dependent FMR measurements at a fixed frequency of 7 GHz. We have rotated the sample in 5° intervals w.r.t the applied magnetic field and measured the FMR spectra. H_r for each angle has been extracted by fitting the FMR spectra using equation 4.1. Figure 4.10 shows the H_r vs ϕ plot for all the samples. The experimental data for SPI1, SPI2, SPI3, SPI4 and SPI5 are represented in red solid circles, green open squares, blue open stars,

pink open circles and green open triangles, respectively, and the solid lines are the best fits using eqn. 4.5. The experimental data is fitted using the Landau-Lifshitz-Gilbert (LLG) equation[133]:

$$f = \frac{\gamma}{2\pi}\left(\left(H + \frac{2K_2}{M_S}\, cos\ cos\ 2\phi\right)\left(H + 4\pi M_S + \frac{2K_2}{M_S}\,\phi\right)\right) \tag{4.5}$$

where, K_2 is the in-plane uniaxial anisotropy constant, ϕ is the in-plane angle between the EA w.r.t the applied magnetic field direction and M_S is the saturation magnetization.

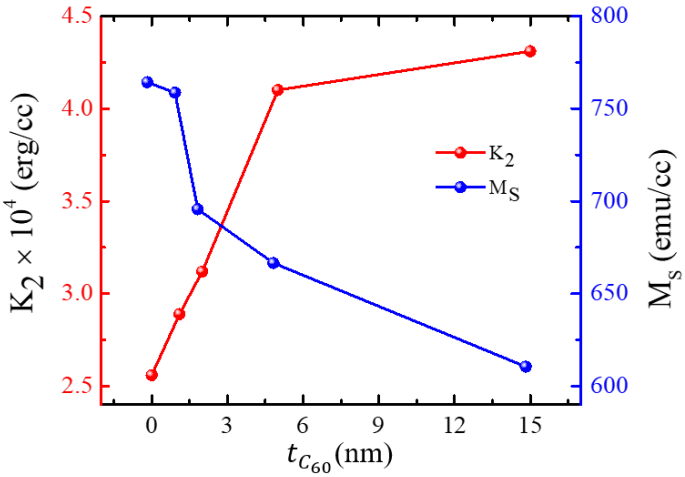

Figure 4.11: C_{60} **t**hickness ($t_{C_{60}}$) dependence of anisotropy constant (K_2) and saturation magnetization (M_S). Red line with solid circles represents K_2 and blue line with solid circles represents M_S.

The extracted values of K_2 and M_S from the fitting of equation (4.5) for all the samples are shown in table 4.3 and thickness dependence of K_2 and M_S is shown in figure 4.11. It has been observed that the anisotropy of the system increases after inserting a C_{60} layer. Also, it has been observed that the saturation magnetization of the system reduces after inserting a C_{60} layer. In previous studies, a reduction of magnetic moment in FM layer has been observed due the formation of spinterface.[33,35,123] The possible reason for this increment in the anisotropy may be due to the hybridization between *d* orbital of Co, Fe, and *p* orbital of C. Due to d-p hybridization at the interface, DOS of C_{60} is modified and forms a spinterface. The anisotropy

increases from 2.56×10^4 to 2.89×10^4erg/cc from single layer CoFeB to CoFeB/C_{60} (1.1 nm) bilayer. It further increases with increasing the thickness of C_{60}. There is a small change in the anisotropy (4.10×10^4 to 4.31×10^4erg/cc) by varying the C_{60} thickness from 5 nm to 15 nm. It has been reported that after a certain thickness of C_{60} layer, the spinterface thickness remains almost constant with increasing C_{60} thickness. The thickness of the spinterface is ~2 nm. This states that the anisotropy is more for SPI4 as compared to SPI2 and SPI3 with increase in spinterface thickness. Whereas from SPI4 to SPI5, increasing the C_{60} thickness does not change the spinterface thickness, thereby keeping the change in anisotropy value negligible. However, the exact thickness of CoFeB/C_{60} spinterface is not known. Future PNR experiments can be carried out to evaluate the thickness of such a spinterface. Our results reveal that the anisotropy for the bilayer samples is more than the CoFeB reference sample.

Table 4.3: The values of K_2 and M_S extracted from the fitting of LLG equation for all the samples

Sample	K_2 (erg/cc)	M_S (emu/cc)
SPI1	2.56×10^4 ±716.80	764.26±2.09
SPI2	2.89×10^4 ±547.40	758.56±0.74
SPI3	3.12×10^4 ±823.91	695.63±3.41
SPI4	4.10×10^4 ±1101.98	666.55±1.28
SPI5	$4.31 \times 10^4 \pm 1891.77$	610.59±6.24

Further, we have compared the FMR anisotropy results with the saturation fields ($\mu_0 H_k$) observed in the hysteresis loops along HA in Figure 4.5.(e). From the figure 4.5 (e) we found that $\mu_0 H_k$ for the samples SPI1, SPI2, SPI4 and SPI5 are 8.06, 9.73, 11.27 and 13.20 mT, respectively. To calculate $\mu_0 H_k$ from the FMR results, we have used the formula $\mu_0 H_k = \frac{2K_2}{M_S}$.[36]

The FMR results show that $\mu_0 H_k$ for the samples SPI1, SPI2, SPI4 and SPI5 are 6.7, 7.6, 12.3 and 14.11 mT, respectively. The small deviation between these two results can be due to the two different techniques. However, in both the cases similar trend has been observed.

In summary, the effect of C_{60} on magnetization reversal, domain, and anisotropy of a low damping amorphous CoFeB alloy have been studied thoroughly. It has been observed that C_{60} layer has a minimal effect on the magnetization reversal of a CoFeB layer. Domain shape and size are almost similar for the bilayer CoFeB/C_{60} samples as compared to reference CoFeB thin films. However, it is difficult to conclude that spinterface have no effect on domain structure of an amorphous ferromagnet. Future work in theory may help in understanding the exact mechanism behind any change of domains due to the spinterface in amorphous ferromagnetic systems. This work brings an important insight that spinterface has almost no effect on the domains in an amorphous CoFeB/C_{60} bilayer system. From the magnetization dynamics study, we have observed that the damping of the system increases with increasing the C_{60} layer thickness. Further, from angle dependent FMR measurements we have evaluated the magnetic anisotropy constant for all the samples. It has been observed that anisotropy has been increased for the bilayer CoFeB/C_{60} thin films in comparison to the single layer CoFeB. With increasing the thickness of the C_{60} layer, the anisotropy also increases. This study reveals that the anisotropy of an amorphous CoFeB system can be enhanced by inserting a C_{60} layer, which can be suitable for future spintronics devices. Theoretical work is needed to explain the exact nature of spinterface and understand the origin.

CHAPTER 5: Effect of Rubrene on magnetic anisotropy and domain structure in Co/Rubrene system

Rubrene (5,6,11,12tetraphenyltetracene) is a prototype of OSC which consists of 24 H and 42 C atoms. It shows highest carrier mobility among other OSCs which is ~40 $cm^2/(Vs)$ for holes and low energy gap ~2.3 eV.[28,134] The spin-orbit coupling in rubrene is also 1 order less than Alq_3.[135] Because of aforementioned properties, it has drawn immense research interest in the field of organic spintronics. The major application of Rubrene is in field-effect transistors, photovoltaic cells and light emitting diodes.[136–138] There are a few reports on organic spin valve systems using Rubrene as a spacer layer.[23,139] However, to the best of our knowledge no work has been reported on the effect of spinterface in FM/Rubrene on magnetization reversal, magnetic domains and anisotropy. It has been shown that inserting a C_{60} layer one can modify the magnetic properties of FM layer.[31,33,34,123] Introduction of a C_{60} layer can enhance the anisotropy and increase the size of domains in Co/C_{60} system as compared to the reference Co film.[35] However, it has not been studied yet that these modifications are only specific to the Co/C_{60} interface or other Co/OSC interface e.g. Co/Rubrene. In this context, we have studied the magnetization reversal of a Co/Rubrene bilayer system in terms of domain imaging and compared that to the reference Co thin film. We have prepared Co thin films on Si substrate with and without rubrene layer. The samples are named as SPI6 and SPI7 for rubrene thickness of 0 and 20 nm, respectively. The detailed sample structure is the following:

SPI6: Si/SiO_2(native oxide)/Co (20 nm)/Ta (5 nm)

SPI7: Si/SiO_2(native oxide)/Co (20 nm)/ Rubrene (20 nm)/Ta (5 nm)

The samples were prepared on Si (100)/SiO_2 (native oxide) substrate using DC magnetron sputtering and thermal evaporation for Co and rubrene, respectively, in the same UHV chamber manufactured by Mantis Deposition Ltd., UK. To prevent oxidation, the samples are capped with a layer of 3 nm Ta. The deposition pressure for Co, Ta was 5×10^{-3} mbar and 1×10^{-7} mbar

for Rubrene evaporation. The Co and Rubrene layers were deposited with the rate of 0.1 and ~ 0.12 – 0.18 $Å s^{-1}$, respectively. Sublimed grade 99.9% pure Rubrene has been purchased from Sigma Aldrich and we have used this powder material in thermal evaporation without any extra purification. Rubrene layer was deposited normal to the substrate whereas the Co plume was at 30° w.r.t to the substrate normal due to the in-built geometry of the deposition system. As discussed previously, due to this oblique angle deposition a presence of uniaxial anisotropy is expected in the samples.[34,35,55,56,124–126,128–130]

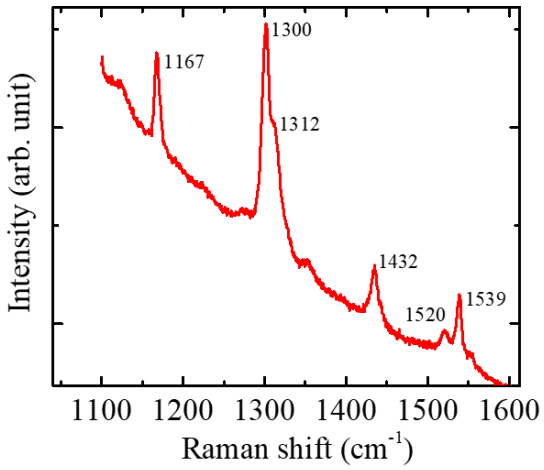

Figure 5.1: Raman spectroscopy data for sample SPI7.

To confirm the deposition of Rubrene molecules we have performed Raman spectroscopy measurement on Co/Rubrene bilayer sample (SPI7). Figure 5.1 shows the Raman spectroscopy data for sample SPI7. Observed peaks at 1167, 1300, 1312, 1432, 1520 and 1539 cm^{-1} confirm the growth of Rubrene molecules.[140]

To study the effect of rubrene on magnetization reversal and domain structure, we have performed hysteresis loop measurements along with domain images using MOKE microscopy for both the samples (with and without rubrene layer). Measurements have been performed at room temperature within a field range $\pm$ 30 mT by varying the angle (ϕ) between the EA and the direction of the applied field in longitudinal mode. Figure 5.2 (a) shows the hysteresis loop measured along the EA of the sample SPI6 (without Rubrene layer). Domain images at

different fields are shown in figure 5.2 (b-g) which are marked in the hysteresis loop of the figure 5.2 (a).

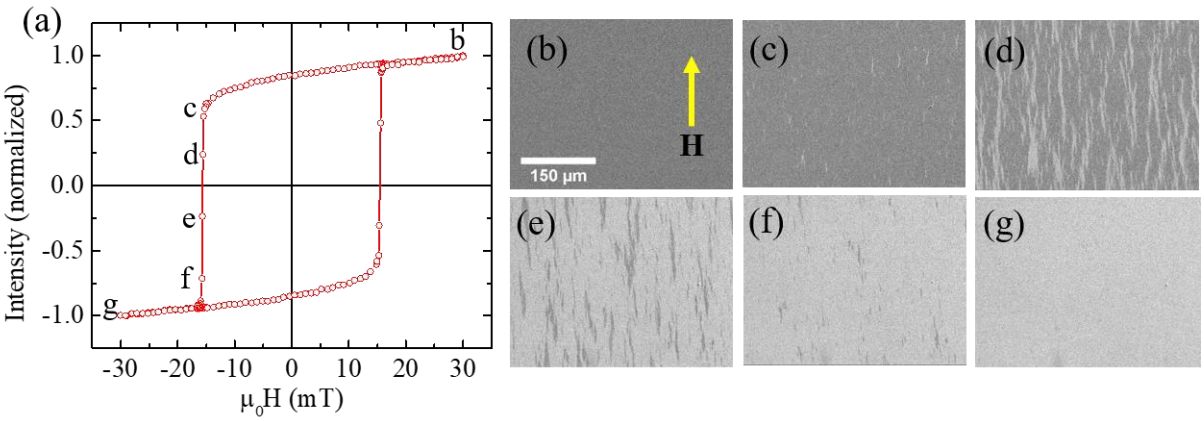

Figure 5.2: (a) Hysteresis loop measured along EA for sample SPI6. (b-g) Domain images captured at different field values, which are marked in (a). Magnetic field direction and scale bar are shown in (b) and same for all the images.

Similar to in-plane anisotropic CoFeB films, here also the magnetization reversal is happening via domain wall motion along the EA (square shaped loop). A single jump between positive to negative saturation indicates a 180° reversal. Figure 5.2 (b-g) show the domain images from a positive saturation state to negative saturation state. At positive saturation, all the spins are aligned in the same direction of the applied field and create a single domain state (dark grey (figure 5.2 (b)). With decreasing the magnetic field, the image contrast also changes from dark to bright and light grey domain appears (figure 5.2 (d) corresponding to the point (d) marked in the hysteresis loop (a)). With further decreasing the field the light grey domain expands (figure 5.2 (e)) and reaches to negative saturation state with complete bright contrast (figure 5.2 (g)). Figure 5.3 (a) shows the EA hysteresis loop for SPI7 (with Rubrene layer) and figure 5.3 (b-g) represent the domain images at different fields which are marked in the hysteresis loop (a). This sample also shows a 180° reversal and the reversal occurring via domain wall motion. The H_C values for the samples SPI6 and SPI7 are 15.56 and 8.20 mT, respectively. It

should be noted that, the value of H_C decreased in the sample having Rubrene layer (SPI7) in comparison to the sample without Rubrene (SPI6).

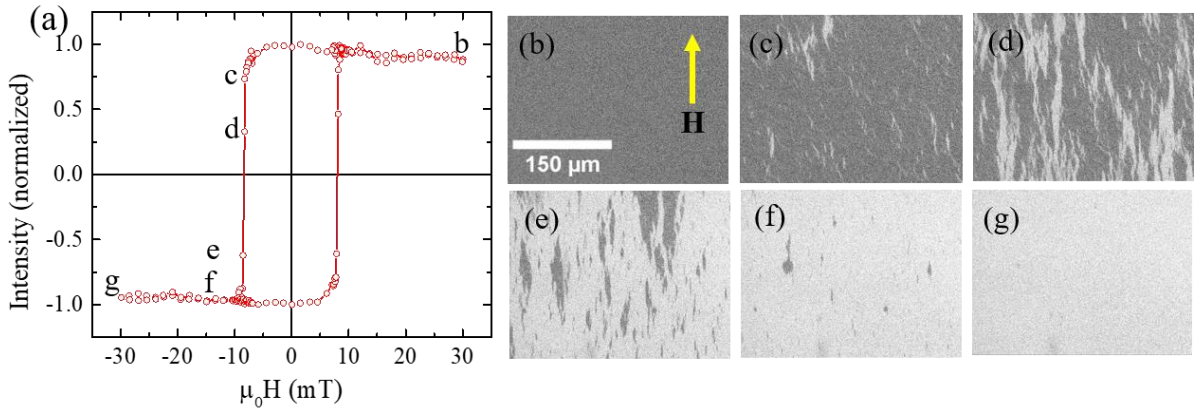

Figure 5.3: (a) Hysteresis loop measured along EA for sample SPI7. (b-g) Domain images captured at different field values, which are marked in (a). Magnetic field direction and scale bar are shown in (b) and same for all the images.

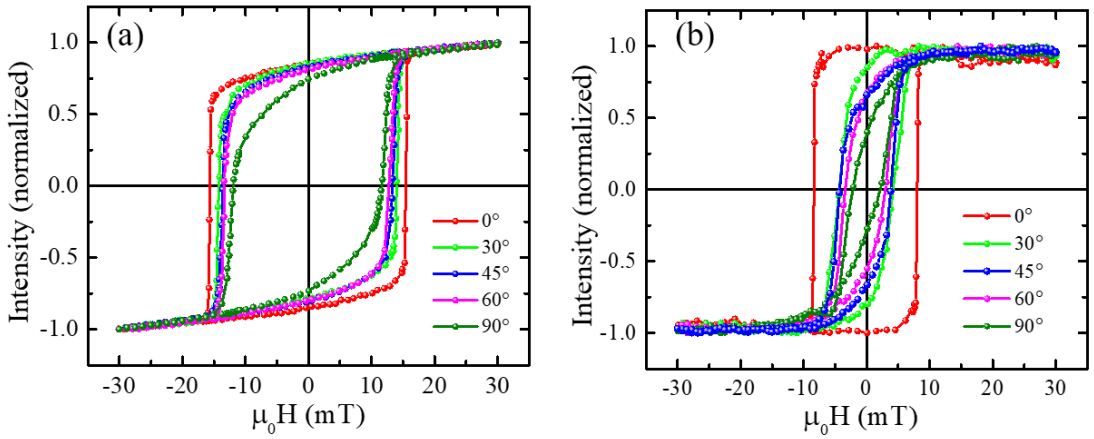

Figure 5.4: Hysteresis loops measured along ϕ = 0°, 30°, 45°, 60° and 90° for sample SPI6 (a), and SPI7 (b).

Angle dependent hysteresis loops for the samples SPI6 and SPI7, measured at ϕ = 0°, 30°, 45°, 60° and 90° are shown in figure 5.4 (a) and (b), respectively. The change in the shape of the hysteresis loops with ϕ indicates the presence of anisotropy in the samples. For both the samples, HA is at 90° w.r.t EA. It should be noted that in single layer Co film we have not observed complete 'S' shaped hysteresis loop (vanishing M_R). The reason behind this nature might be dispersion of the local grain anisotropies (i.e., the misalignment of magnetization

directions among the neighbouring grains) due to the polycrystalline growth of Co film on top of Si (100) substrate[35,127,141,142]. Figure 5.5 (a-e) represent the domain images of SPI6, recorded near H_C at ϕ = 0°, 30°, 45°, 60° and 90°, respectively. Similarly, figure 5.5 (f-j) show the same for SPI7. We have not observed any domain at ϕ = 90° for SPI6 and ϕ = 30°, 45°, 60°, 90° for SPI7 as the magnetization reversal may occur via coherent rotation.

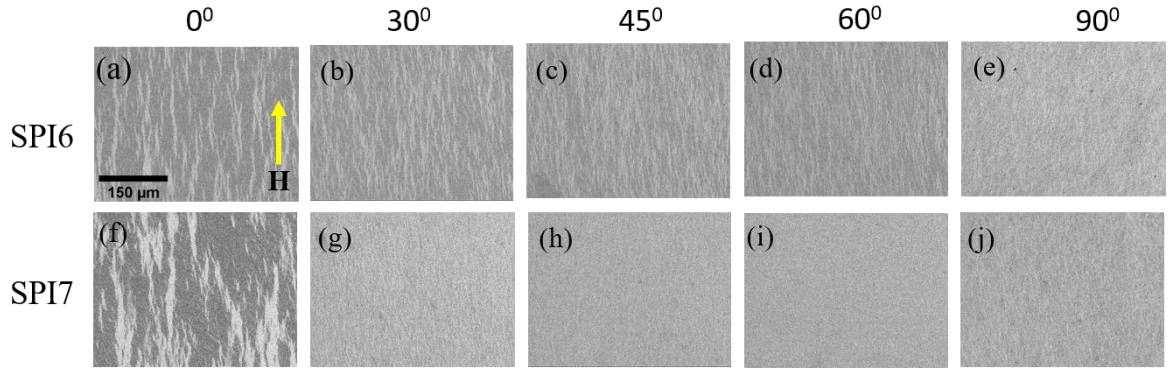

Figure 5.5: Domain images captured near H_C are shown in (a-e), and (f-j) for samples SPI6, and SPI7 respectively. The scale bar and the direction of applied field are shown in (a) and same for all the images.

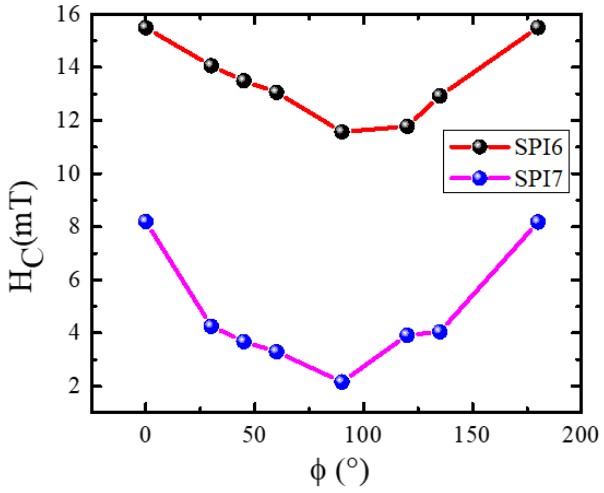

Figure 5.6: H_C vs ϕ plot for the samples. Black solid circles with red line represent SPI6 and blue solid circles with pink line represent SPI7.

Qualitatively the anisotropy can be obtained from the change in H_C between the EA and HA. Figure 5.6 shows the variation of H_C w.r.t ϕ for both the samples. It is observed that the difference in H_C between EA and HA for sample SPI7 (with Rubrene) is more than SPI6

(without Rubrene). This indicates that the anisotropy of bilayer Co/Rubrene is more than single layer Co thin film. Further, we have evaluated the effective anisotropy constant using SQUID magnetometry.

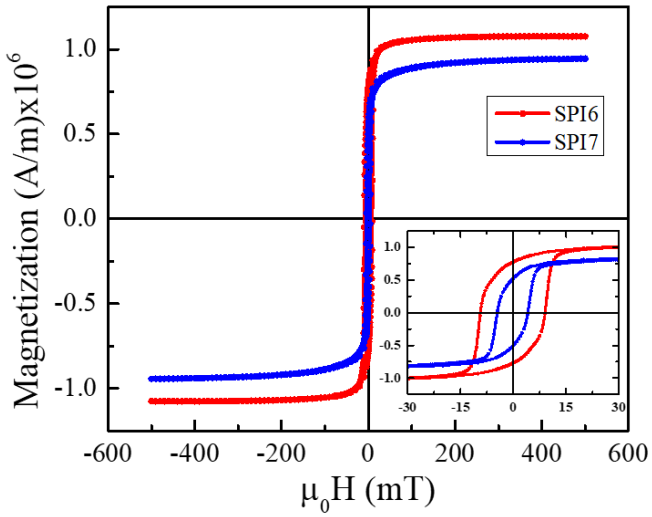

Figure 5.7: Hysteresis loops measured by SQUID magnetometer for sample SPI6 (red line) and SPI7 (blue line) at room temperature. During the measurement, magnetic field was applied along in-plane direction i.e., parallel to the sample surface. Inset figure show the zoomed view of the loops.

To evaluate the effective anisotropy (K_{eff}) of the system, we have performed field dependence of magnetization (*M-H*) measurement at room temperature using SQUID magnetometer in both in-plane (EA of the samples) and out-of-plane (HA of the samples) directions. Figure 5.7 show the magnetization vs field plots for both the samples when the magnetic field is applied parallel to the sample surface. M_S value for SPI6 and SPI7 are 1.07×10^6 and 0.94×10^6 A/m, respectively. It should be noted that M_S decreases for the bilayer sample (SPI7) in comparison to the single layer Co film (SPI6). The decrease in magnetization is probably due to the orbital hybridization which results the reduction of magnetic moment in the Co layer. This loss of magnetization is an indication of the presence of hybridization at the Co/Rubrene interface.

M-H loops measured along EA and HA of the samples are shown in figure 5.8 (a) and (b) for SPI6 and SPI7, respectively. It has been observed that for both the samples, higher field is

needed to saturated the sample when the field is applied perpendicular to sample plane, which indicates that the preferred magnetization direction of the sample is in-plane.

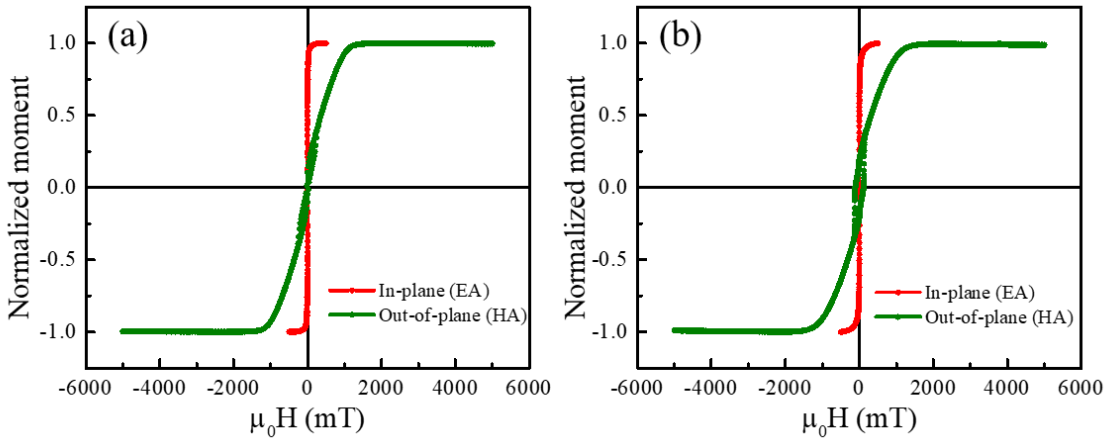

Figure 5.8: Hysteresis loops measured along both the in-plane and out-of-plane direction via SQUID magnetometer for samples SPI6 (a) and SPI7 (b) at room temperature. Red lines represent the hysteresis loops measured along in-plane direction and green line represent the hysteresis loops measured along out-of-plane direction i.e., magnetic field applied perpendicular to the sample surface.

We have calculated K_{eff} using the following equation:

$$K_{eff} = \frac{1}{2}\mu_0 H_K M_S \tag{5.1}$$

where, μ_0 is the free space permeability and H_K is the saturation field along HA.

The value of K_{eff} for SPI6 and SPI7 are 7.41×10^5 and 7.8×10^5 J/m^3, respectively. This suggests that the anisotropy is more for SPI7 as compared to SPI6, which we also observed form the change in H_C with ϕ. The enhancement in the anisotropy is possibly due to the formation of spinterface and orbital hybridization at Co/Rubrene interface. Spin polarized charge transfer from Co to Rubrene and the hybridization between the *d* orbital of Co atom and *p* orbital of C atom have been observed by Wang et al. [143]

In summary, we have observed that in Co/Rubrene system H_C decreases for the bilayer samples as compared to single layer Co thin film. Both the samples exhibit in-plane uniaxial anisotropy.

Further, we have calculated the effective anisotropy using SQUID magnetometry measurements and observed that anisotropy of the system increased introduction of a Rubrene layer. These results reveal that similar to Co/C_{60} system, in Co/Rubrene system also, one can enhance the anisotropy of a Co layer by inserting a Rubrene layer like C_{60}. However, in Co/Rubrene system, the spinterface properties i.e, the exact thickness of spinterface, induced magnetic moment need to be explored in future via polarized neutron reflectivity (PNR) measurement.

CHAPTER 6: Spinterface in perpendicularly magnetized Pt/Co/C_{60}/Pt and Pd/Co/C_{60}/Pd systems

In the previous chapters the effect of spinterface on the magnetic properties such as anisotropy, domains and damping in in-plane magnetized systems have been discussed. It is known that perpendicular magnetic anisotropic (PMA) systems are the most suitable candidates for data storage devices due to their high intrinsic anisotropy.[144] Due to high thermal stability and low energy consumption, PMA based devices have advantages over the in-plane ones. Magnetic moments are perpendicularly aligned to the film plane in PMA systems which enhances the spin-flipping efficiency and reduces the required current density which may be useful for spin-orbit torque (SOT) based devices.[144,145] It has been reported that the inserting a C_{60} layer can make a spin reorientation transition (SRT) from in-plane anisotropy to out-of-plane anisotropy.[36,64] There are a few reports where it has been observed that after inserting a OSC layer ($CoFe_3N$, C_{60}) the anisotropy of the system increases.[146,147] Therefore, it is quite appealing to study magnetic domains and magnetization relaxation in a PMA based FM-OSC systems. From application point of view, domain engineering via various approaches is appealing. It has been shown that the domain size was significantly reduced by making magnetic antidot lattice array (MAL) in a Pt/Co/Pt film.[148] However, the study the effect of spinterface on domains and magnetization relaxation in a perpendicularly magnetized films has not been reported yet. In this context, we have considered Pt/Co/C_{60}/Pt and Pd/Co/C_{60}/Pd systems which exhibit high PMA and investigate the effect of Co-C_{60} spinterface on global anisotropy, domain size and magnetization relaxation. This chapter is divided into two parts. First, we focus on the Pt/Co/C_{60}/Pt system and afterwards we will discuss the results of Pd/Co/C_{60}/Pd system.

6.1: Effect of C_{60} on anisotropy, domain size and magnetization relaxation in a perpendicularly magnetized Pt/Co/C_{60}/Pt system

Thickness of the FM layer is very crucial for PMA based system. Therefore, to achieve a high PMA based system we have prepared Pt/Co/Pt multilayer thin films by varying the Co layer thickness. To promote the growth of Pt (111) direction, a Ta layer has been used as a seed layer. We have rotated the substrate at 20 rpm during deposition to maintain the growth uniformity. A 4.5 nm thick Pt layer has been used as a capping layer to prevent from oxidation of the films. Ta, Pt and Co have been deposited using DC magnetron sputtering in the same UHV chamber. All the layers were deposited without breaking the vacuum to avoid surface contamination and oxidation. Hysteresis loops have been measured using MOKE based microscopy within ±50 mT magnetic field in polar mode. Figure 6.1.1 shows the hysteresis for different Co thicknesses.

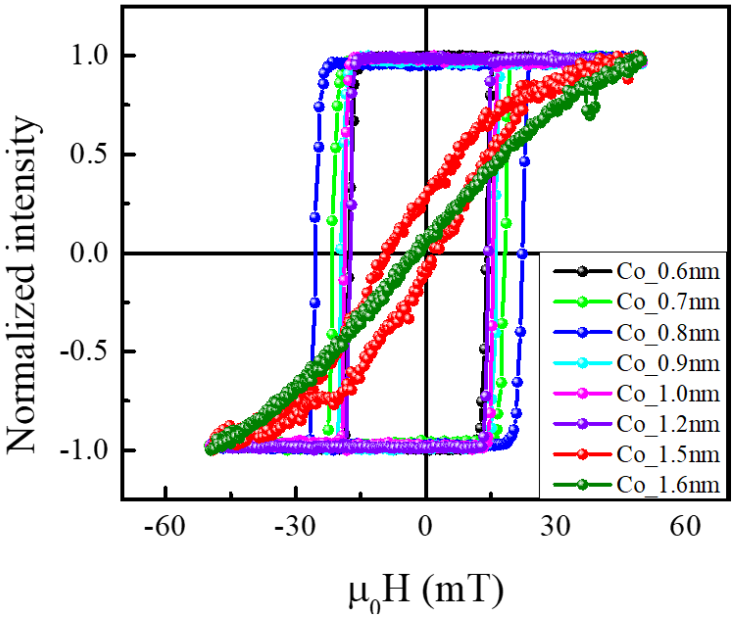

Figure 6.1.1: Hysteresis loop measured by MOKE based microscopy in polar mode for different Co layer thickness.

It has been observed that the system exhibits PMA below 1.5 nm Co thickness. Above 1.5 nm of Co thickness the system becomes in-plane isotropic. Therefore, the SRT for Pt/Co system occurs at ~1.5 nm of Co thickness. To study the effect of Co-C_{60} spinterface on anisotropy,

domain size and magnetization relaxations, we have considered Pt/Co/C_{60}/Pt system with Co thickness 0.8 nm which is well below the SRT and exhibits high PMA. C_{60} layer has been deposited using thermal evaporation technique. The sample structure of with and without C_{60} layers are the following:

Sample SPP1: Si/SiO2 (native oxide)/Ta (3 nm)/Pt (3.5 nm)/Co (0.8 nm)/Pt (4.5 nm)

Sample SPP2: Si/SiO2 (native oxide)/Ta (3 nm)/Pt (3.5 nm)/Co (0.8 nm)/C_{60} (0.5 nm)/Pt (4.5 nm)

Sample SPP3: Si/SiO2 (native oxide)/Ta (3 nm)/Pt (3.5 nm)/Co (0.8 nm)/C_{60} (1.6 nm)/Pt (4.5 nm)

Sample SPP4: Si/SiO2 (native oxide)/Ta (3 nm)/Pt (3.5 nm)/Co (0.8 nm)/C_{60} (3.2 nm)/Pt (4.5 nm)

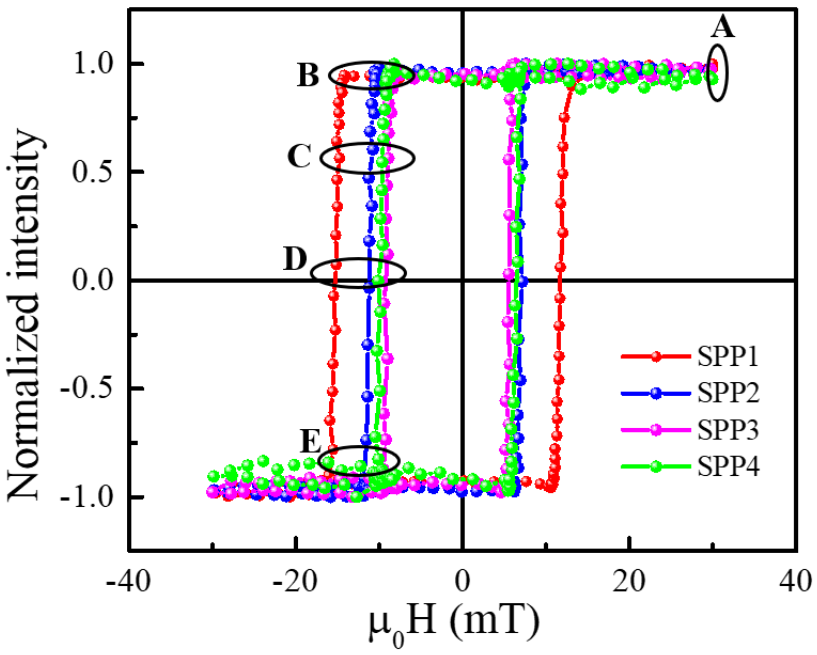

Figure 6.1.2: Hysteresis loops measured at room temperature using polar MOKE. The red, blue, pink and green solid circles with lines represent the sample SPP1, SPP2, SPP3 and SPP4, respectively.

Magnetic domain imaging and magnetization relaxation measurements have been performed using MOKE based microscopy in polar mode and within the field range of ±30 mT at room

temperature. Figure 6.1.2 shows the hysteresis loops for all the samples with and without C_{60} layers. The red, blue, pink and green solid circles with lines represent the hysteresis loops for samples SPP1, SPP2, SPP3 and SPP4, respectively. H_C for SPP1, SPP2, SPP3 and SPP4 are 13.5, 9.1, 7.5 and 8.0 mT, respectively. It has been observed that after inserting a thin C_{60} layer H_C decreases as compared to the reference one (SPP1). However, H_C of the samples having C_{60} layer are comparable and the change in H_C is nominal by varying the thickness of C_{60} from 0.5 to 3.2 nm. We have recorded the domain images at different field points (A-E) of the hysteresis loops which are marked in figure 6.1.2 and the domain images are shown in figure 6.1.3. A-E points represent positive saturation (+H_S), nucleation (H_N), in between H_N and H_C, at H_C and near negative saturation field (-H_S), respectively.

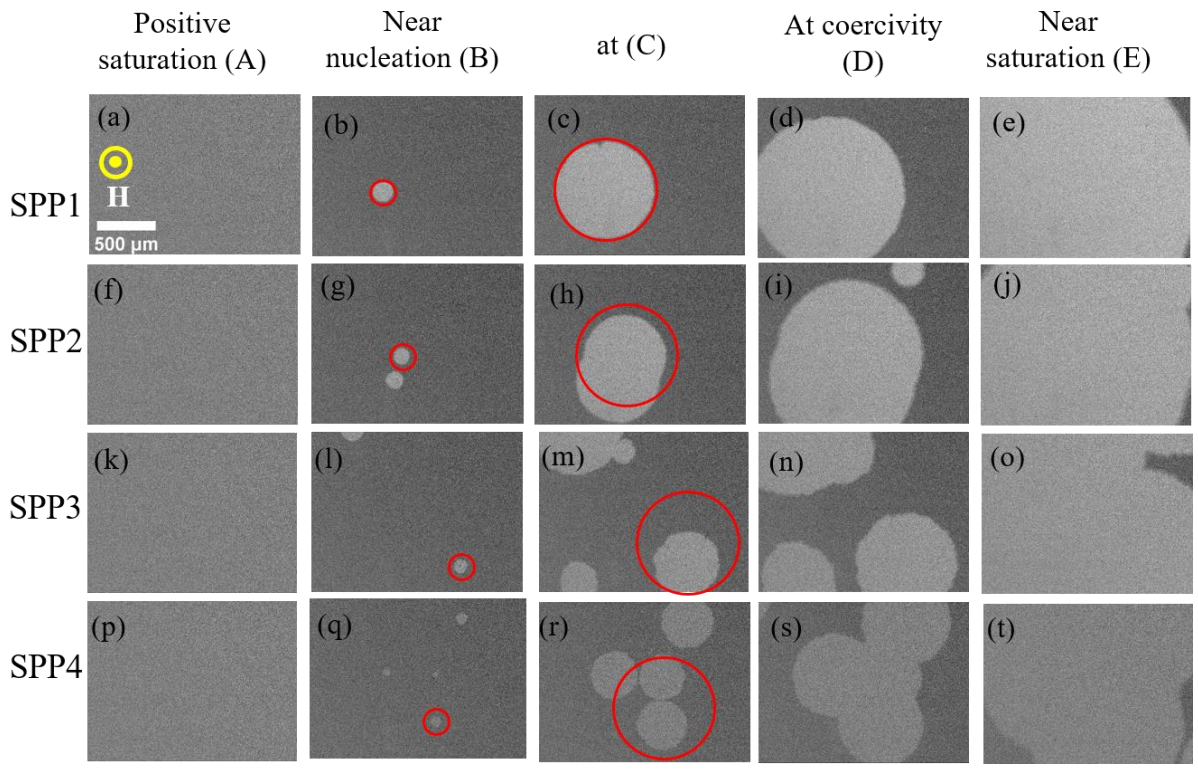

Figure 6.1.3: Domain images for samples SPP1 (a-e), SPP2 (f-j), SPP3 (k-o) and SPP4 (p-t). Domain images corresponding to A-E points of the hysteresis loops are shown in figure 6.1.2. Magnetic field direction and scale bar is shown in (a) and same for all the images.

Domain images for SPP1, SPP2, SPP3 and SPP4 are shown in figure 6.1.3 (a-e), (f-j), (k-o) and (p-t), respectively. Bubble domains start appearing beyond the nucleation field. Bubbles expand with increasing the magnetic field and near saturation field they merge to each other and complete the reversal. For all the samples, uniform bubble domains are observed as the anisotropy ratio, $Q = {K_U}/{K_d} \gg 1$, where K_U and K_d are perpendicular anisotropy and stray field energy densities, respectively.[53] It has been shown that the size of the domains become smaller after introducing a C_{60} layer (SPP2-SPP4) as compared to the reference sample SPP1. For better visualization, domains are marked in red circles with same diameter for (b, g, l, q) and (c, h, m, r) in figure 6.1.3. It should be noted that with increasing the thickness of the C_{60} layer domain size further decreases. The reason behind this decrease in domain size possibly due to the formation of spinterface at Co-C_{60} interface. In literature it has been shown that spinterface thickness of C_{60} is ~2 nm.[35,33,34] Further, we have prepared similar set of samples with a different Co thickness (0.6 nm). The samples are named as SPP5, SPP6, SPP7 and SPP8 for $t_{C_{60}}$= 0, 0.5, 1.6 and 3.2 nm, respectively. Hysteresis loops and corresponding domain images of the samples are shown in figure 6.1.4 and 6.1.5, respectively.

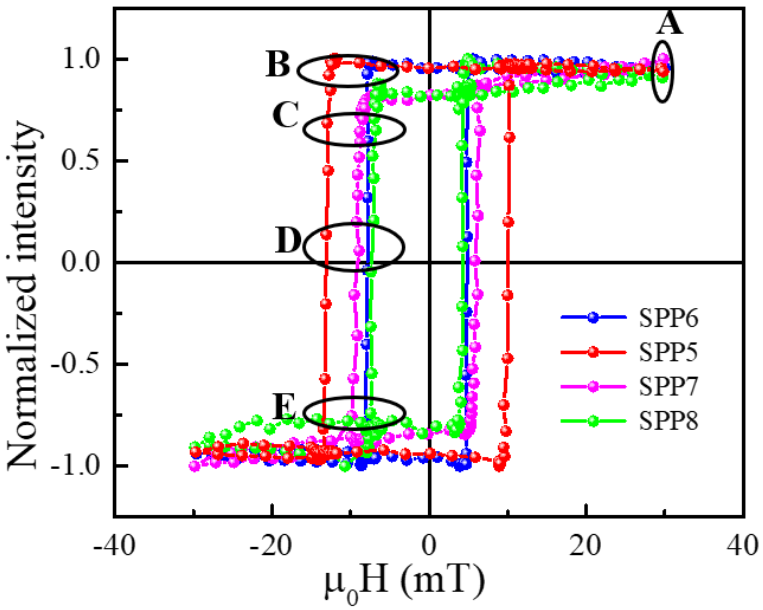

Figure 6.1.4: Hysteresis loops of the samples SPP5 (red), SPP6 (blue), SPP7 (pink) and SPP8 (green).

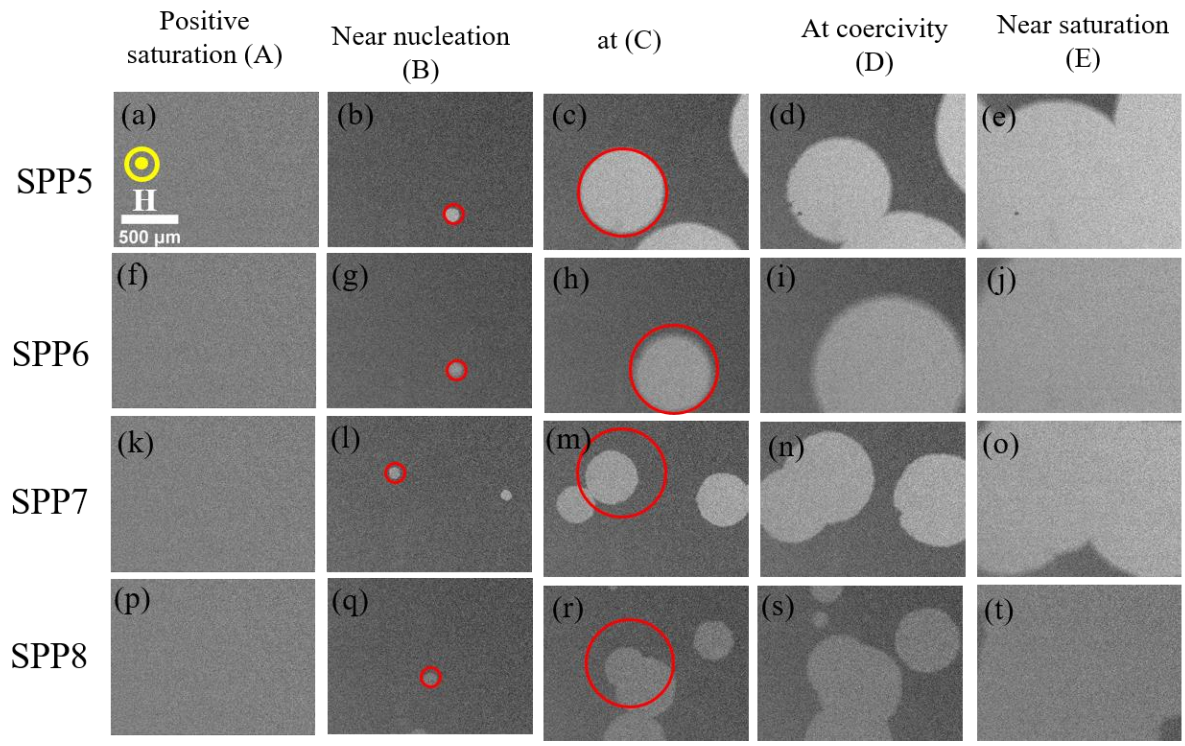

Figure 6.1.5: Domain images for samples SPP5 (a-e), SPP6 (f-j), SPP7 (k-o) and SPP8 (p-t). Domain images corresponding to A-E points of the hysteresis loops shown in figure 6.1.4. Magnetic field direction and scale bar is shown in (a) and same for all the images.

Here, also we have observed that coercivity and domain size decrease with increasing the thickness of C_{60} layer. The decrease in domain size can be explained in terms of anisotropy energy. To evaluate the magnetic anisotropy, field dependent magnetization (M – H) measurements have been performed via SQUID magnetometry along HA (i.e., in-plane) and EA (out-of-plane) of the samples. We have calculated K_{eff} using equation 5.1. Thickness ($t_{C_{60}}$) dependence plot for effective anisotropy (K_{eff}) , saturation magnetization (M_S) and HA saturation field ($\mu_0 H_K$) are shown in figure 6.1.6. M_S decreases with increasing the C_{60} thickness is probably due to the formation of spinterface Co-C_{60} interafce and hybridization between the d orbital of Co and π orbital of C atoms which leads to the reduction of magnetic moment in Co layer. Figure 6.1.6 shows that anisotropy increases with increasing the C_{60} layer thickness. As the anisotropy energy increases, more domain nucleation is happening which leads to

decrease of the size of the individual domains. Further, due to the symmetric structure, Pt/Co/Pt sample exhibits very negligible interfacial Dzyaloshinskii–Moriya interaction (iDMI). After introducing a C_{60} layer one Pt/Co interface is replaced by Co/C_{60}. Therefore, due to the broken inversion symmetry a finite amount of iDMI is expected in Pt/Co/C_{60}/Pt multilayer structure. This finite iDMI may also affect the domain size and anisotropy of the system.[149] The detailed investigation of the iDMI in such multilayer stack should be explored in future and is beyond the scope of this thesis.

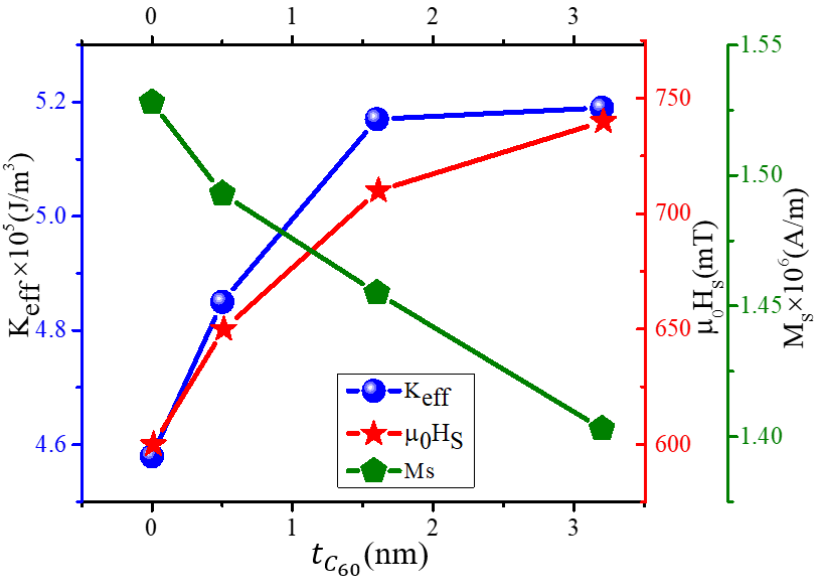

Figure 6.1.6: Thickness dependence ($t_{C_{60}}$) of effective anisotropy (K_{eff}) (red solid circles), HA saturation field ($\mu_0 H_K$) (green stars) and saturation magnetization (M_S) (blue pentagon).

Magnetization relaxation measurements have been performed using Kerr microscopy at room temperature to calculate the relaxation time of the systems. The relaxation measurement protocol is discussed below. First we have applied +30 mT field to saturate the sample and then reversed the magnetic field and kept the field constant to a sub-coercive field (0.93 H_C, 0.95 H_C etc.). This constant field is called measurent field (H_M). Here the magnetization relaxes with time under a constant Zeeman energy and complete the reversal process via domain nucleation and/or DW motion under the influence of thermal activation energy. During this process, domain images were recorded at a regular interval of time. Using ImageJ software we have

calculated the average normalized intensity and plotted it w.r.t time (t). The relaxation curves can be fitted using various models.[126,150–154] In this case, the experimental data have been fitted using compressed exponential function[155]:

$$I(t) = I_1 + I_2\left(1 - \exp\left(-\left(t/\tau\right)^{\beta}\right)\right) \tag{6.1.1}$$

where, $I(t)$ represents the Kerr intensity at time t, $I_1 + I_2$ is normalized Kerr intensity measured at saturation, τ is relaxation time constant and β is an exponent having value between 1 (reversal dominated by domain nucleation) and 3 (reversal dominated by DW motion).

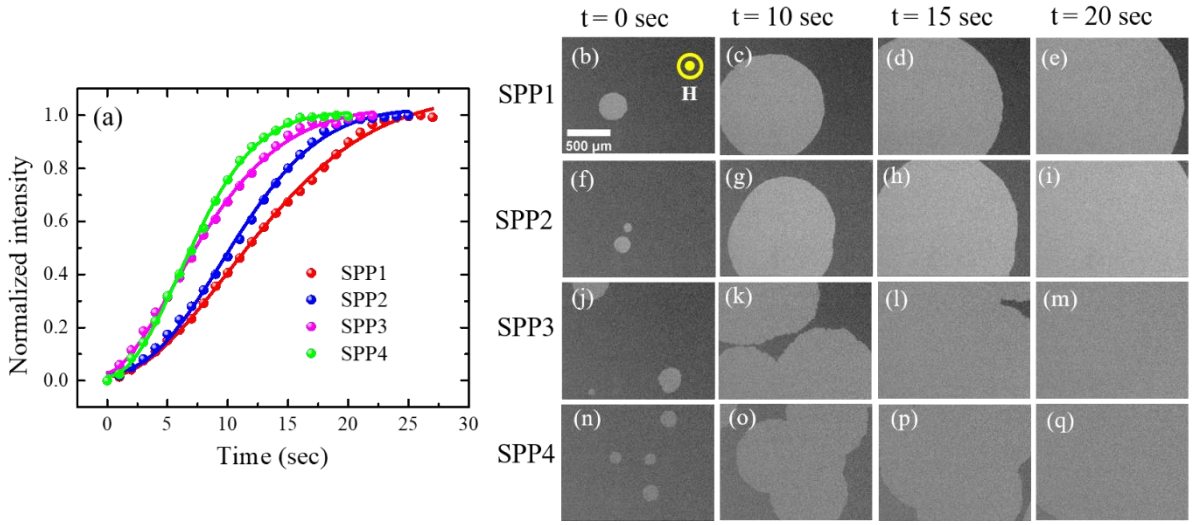

Figure 6.1.7: (a) Relaxation data for all the samples measured at H_M=0.93 H_C, where the red, blue, pink and green solid circles represent the raw data for SPP1, SPP2, SPP3 and SPP4, respectively, and solid lines are the best fits using equation (6.1.1). (b - e), (f - i), (j - m) and (n - q) show the domain images for the samples SPP1, SPP2, SPP3 and SPP4, captured at 0, 10, 15 and 20 seconds, respectively. Scale bar and the applied field direction are shown in (b) and same for all the images.

To compare the nature and speed of the relaxation with different Zeeman energy, we have performed the relaxation measurements at different sub-coercive fields (0.93, 0.95, 0.97 H_C). Figure 6.1.7 (a) shows the relaxation behaviour of the samples at H_M=0.93 H_C. (b - e), (f - i), (j - m) and (n - q) represent the domain images for the samples SPP1, SPP2, SPP3 and SPP4,

respectively, which have been captured at 0, 10, 15 and 20 seconds. Figure 6.1.7 (b), (f), (j) and (n) show the domain images which are captured at $t = 0$, i.e., just after applying H_M. Further, under the influence of thermal activation energy the domains are evolved with time.

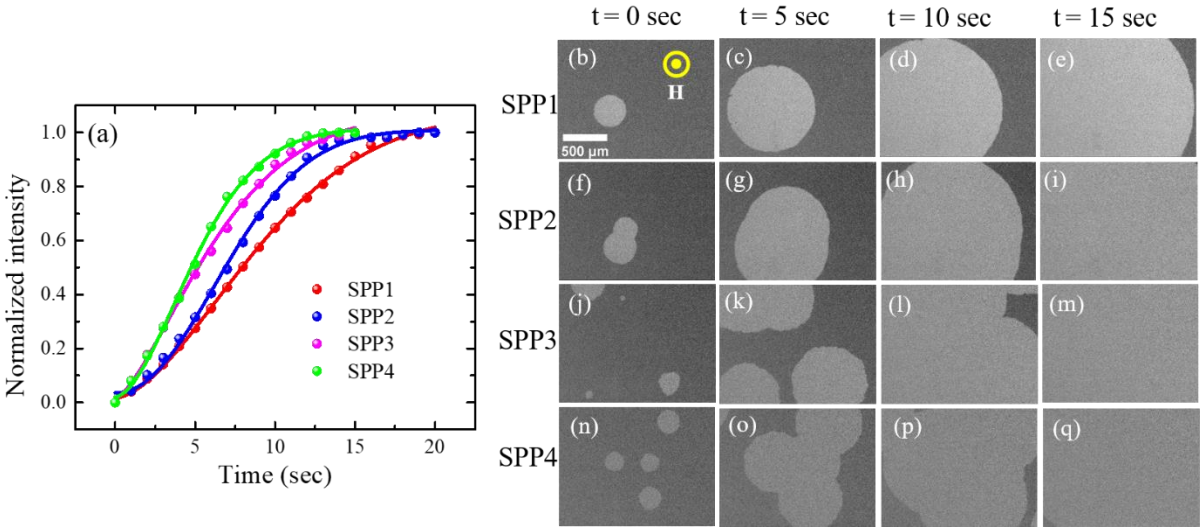

Figure 6.1.8: (a) Relaxation data for all the samples measured at H_M=0.95 H_C, where the red, blue, pink and green solid circles represent the raw data for SPP1, SPP2, SPP3 and SPP4, respectively, and solid lines are the best fits using equation (6.1.1). (b - e), (f - i), (j - m) and (n - q) show the domain images for the samples SPP1, SPP2, SPP3 and SPP4, respectively, which have been captured at 0, 5, 10 and 15 seconds. Scale bar and the applied field direction are shown in (b) and same for all the images.

Table 6.1.1: Parameters obtained from the best fits of the experimental data shown in figure 6.1.7, 6.1.8 and 6.1.9 using equation 6.1.1.

Sample name	$0.93H_C$		$0.95H_C$		$0.97H_C$	
	τ (sec)	β	τ (sec)	β	τ (sec)	β
SSP1	15.08±0.28	1.86±0.06	10.63±0.20	1.69±0.05	8.11±0.13	1.72±0.04
SSP2	12.54±0.07	2.20±0.08	8.46±0.13	2.09±0.09	5.28±0.07	2.16±0.10
SSP3	9.67±0.15	1.58±0.08	7.26±0.25	1.46±0.07	4.41±0.15	1.64±0.06
SSP4	8.57±0.08	1.97±0.05	6.04±0.10	1.74±0.07	4.60±0.08	1.92±0.08

The values of β from the fits of the experimental data using equation (6.1.1), are 1.72 $\pm$ 0.04, 2.16 $\pm$ 0.10, 1.64 $\pm$ 0.06 and 1.92 $\pm$ 0.08 for SPP1, SPP2, SPP3 and SPP4, respectively, which ensures that the magnetization reversal started via domain nucleation and subsequently proceeded via DW motion[148].

Similarly, figure 6.1.8 and 6.1.9 show the relaxation behaviour of the samples at H_M = 0.95 H_C and 0.97 H_C, respectively. The values of β and τ for all the samples are obtained from the best fits to equation (6.1.1) and shown in Table 6.1.1.

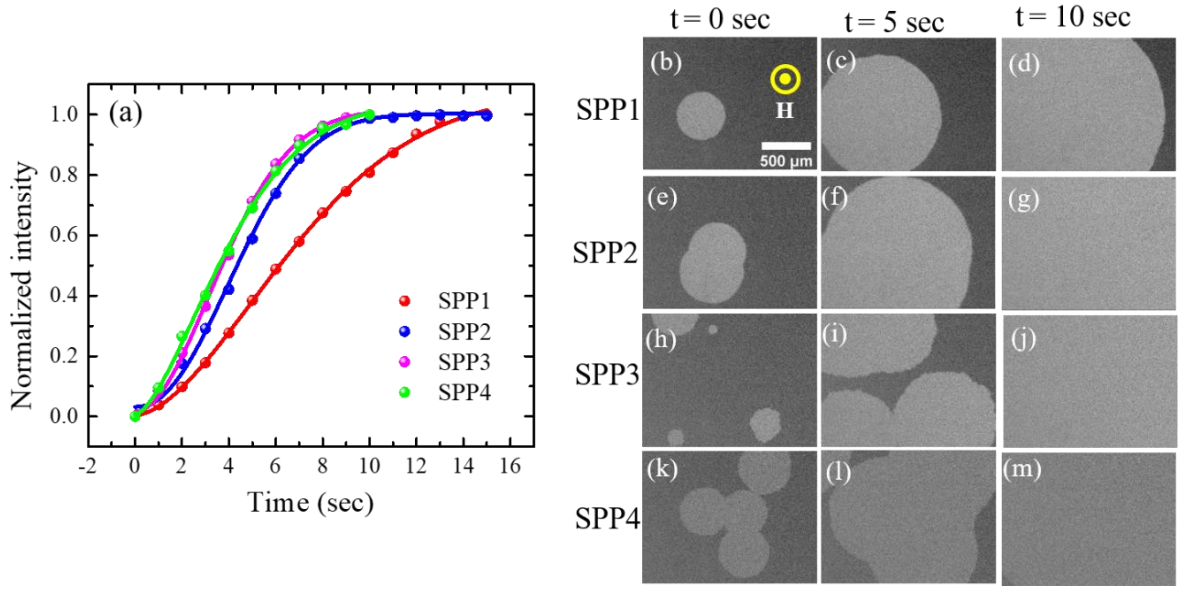

Figure 6.1.9: (a) Relaxation data for all the samples measured at H_M=0.97 H_C, where the red, blue, pink and green solid circles represent the raw data for SPP1, SPP2, SPP3 and SPP4, respectively, and solid lines are the best fits using equation (6.1.1). (b - d), (e - g), (h- j) and (k - m) show the domain images for the samples SPP1, SPP2, SPP3 and SPP4, respectively, which have been captured at 0, 5 and 10 seconds. Scale bar and the applied field direction are shown in (b) and same for all the images.

For all the samples relaxation becomes fast (i.e., τ decreases) as the amplitude of H_M is increased, which is expected. However, as compared to Pt/Co/Pt system (SPP1) the relaxation

process is fast for Pt/Co/C_{60}/Pt thin film (SPP2). Further, with increasing the C_{60} layer thickness τ decreases (SPP3 and SPP4). Therefore, it is inferred that by the introduction of a C_{60} layer one can tune the switching speed of a system which is very promising for device applications. Further, the nature of the Co-C_{60} spinterface has been explored through applying spin polarized density functional theory (DFT) calculations. The DFT results have been obtained in collaboration with Mr. Aritra Mukhopadhyaya and Dr. Ehesan Ali, from INST, Mohali, India We have considered two types of Co lattice (HCP-Co(0001) and FCC-Co(111)) as the exact morphology is not known. C_{60} is deposited on the Co slabs with two different adsorption geometry; Pentagonal and Pentagonal-hexagonal.[36,64,156] 3 layers of Co slab with a 4×4 inplane repetition is chosen to model the surface slab in conjunction with the experimental samples. We have analyzed the interfacial magnetic properties in terms of exchange interaction and magnetic anisotropy energies.

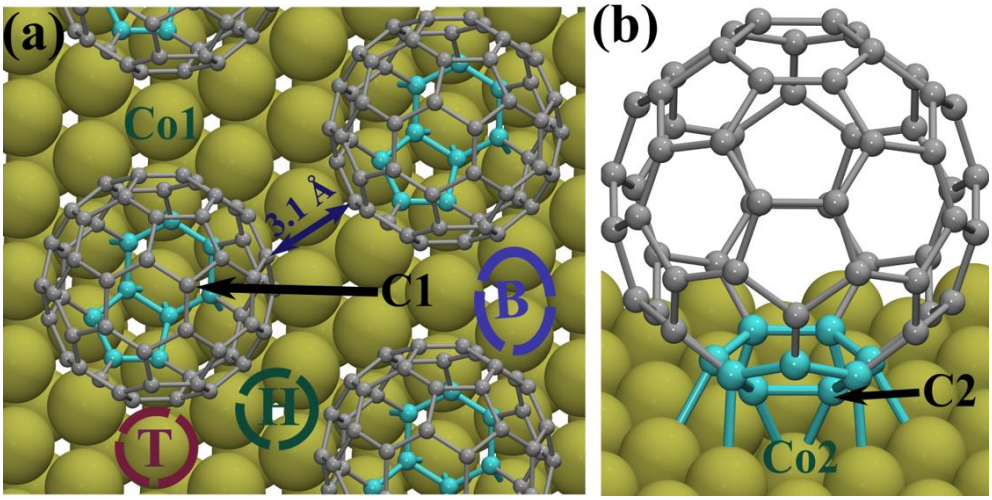

Figure 6.1.10: Chemisorption of C_{60} molecule with a pentagonal-hexagonal adsorption geometry on HCP-Co(0001) substrate. (a) The top view of extended simulation supercell. The circled areas on the Co layer surfce represent different adsorption sites where T, H and B stands for Top, Hollow and Bridged adsorption sites on the Co substrate. Co1 and C1 are the free Co and C atoms. (b) Formation of spinterface on a single C_{60} unit. The bigger tan-coloured balls and grey balls represent Co and C atoms, respectively. Cyan balls represent the C atoms

(lebelled as C2) which participate in chemical bond formation with the Co (lebelled as Co2) atoms.

To understand the atomistic details and the electronic structure of the spinterface, spin polarized DFT calculations were performed using Vienna Ab-initio Simulation Package (VASP).[157] In the calculations, the valence electronic states are expanded with a plane wave basis set, while the core electrons are treated with pseudopotential. The valence-core interaction was represented by full-potential Projected Augmented Wave (PAW) method[158]. The Generalized Gradient Approximations (GGA) is used to treat the exchange-correlation potentials with the Perdew, Bruke, and Ernzerof (PBE) functional[159]. A plane-wave cut-off of 500 eV was used to guarantee a good convergence of the total energy. The convergence tolerance for the self-consistent electronic minimization was set to 10^{-6} eV/cycle. For optimization, a Gaussian smearing parameter of 0.2 eV is used to smear the bands. A Monkhorst-Pack K-points grid is taken as (3x3x3) for getting the bulk unit cell parameters and (3x3x1) for the surface slabs and interface. All the structures were optimized with PBE functional. The Co 3*d* orbitals are treated with a U_{eff} = 3.0 eV for the calculation of magnetic anisotropy energy (MAE).

The optimized cell parameters are *a* =2.50 (2.51) Å and *c/a* =1.6 for HCP Co and *a* = 2.48 for FCC Co. Values within the parenthesis represent the parameters obtained from experiments.

Table 6.1.2: Parameters used to define the interface formation between different Co-slabs and C_{60}

System		**E_{ads}(kcal/mol)[a]**	**e^- -transferred[b]**	**Co-C bonds[c]**
HCP-Co(0001)	Penta- C_{60}	-94.89	1.50	9
	Penta-Hexa- C_{60}	-100.30	1.41	8
FCC-Co(111)	Penta- C_{60}	-83.15	1.45	7
	Penta-Hexa C_{60}	-95.10	1.39	8

[a] Adsorption Energy, $E_{ads}=E_{Co+C60}-(E_{Co}+E_{C60})$

[b] e^- -transferred from Co substrate to C_{60}=Bader population on C_{60} in Co+C_{60} – Bader population on C_{60}.

[c] Co-C bond distance Cut-off = 2.2 Å

A comparison of different spinterface related properties of the above mentioned systems is given in Table 6.1.2. Comparison of E_{ads} indicates a strong chemisorption of C_{60} with Co for all the configurations and Penta-Hexa adsorption of C_{60} leads to more stable configuration. The MAE of the systems is calculated accounting the spin-orbit couplings in the noncollinear magnetic calculations. Here, we have calculated MAE as MAE = E_{axis}-$E_{Z\text{-}axis}$. The magnetic EA is aligned out of plane i.e, perpendicular to Co layer surfaces. Table 6.1.3 shows the values of MAE w.r.t. to the EA anisotropy for pristine Co as well as for C_{60} adsorbed surface. The positive value of MAE indicates out of plane magnetic anisotropy.

The enhancement in MAE has been observed except for penta-C_{60} on HCP-Co which is a less favorable configuration. This enhancement is due to the adsorption of the C_{60} on the Co-layers. This indicates the hardening of the pinning of out-of-plane magnetization due to strong adsorption of C_{60} on Co-substrate.

Table 6.1.3: Out of plane MAE values for different Co substrate and adsorption energy in two in-plane direction.

System	**MAE(meV)**	
	X-axis	**Y-axis**
HCP-Co(0001)	8.25	8.26
HCP-Co(0001)+Penta-C_{60}	7.55	7.37
HCP-Co(0001)+Penta-Hexa-C_{60}	8.94	8.78
FCC-Co(111)	0.59	0.58
FCC-Co(111)+Penta-C_{60}	0.91	0.63
FCC-Co(111)+Penta-Hexa-C_{60}	2.00	1.98

6.2: Effect of C_{60} on domain size and magnetization relaxation in a perpendicularly magnetized Pd/Co/C_{60}/Pd system

Further, we have considered a different PMA based system Pd/Co/Pd and studied the effect of spinterface on magnetic domain and relaxation. It should be noted that Pd/Co/Pd system also shows PMA for Co thickness below ~1nm. The samples are named as SPP9 and SPP10 and the detailed sample structure is given below.

SPP9: Si/SiO2 (native oxide)/Ta (10 nm)/Pd (3.1 nm)/Co (0.5 nm)/Pd (1.5 nm)/Ta (3 nm)

SPP10: Si/SiO2 (native oxide)/Ta (3 nm)/Pt (3.1 nm)/Co (0.5 nm)/C_{60} (2 nm)/Pd (1.5 nm)/Ta (3 nm)

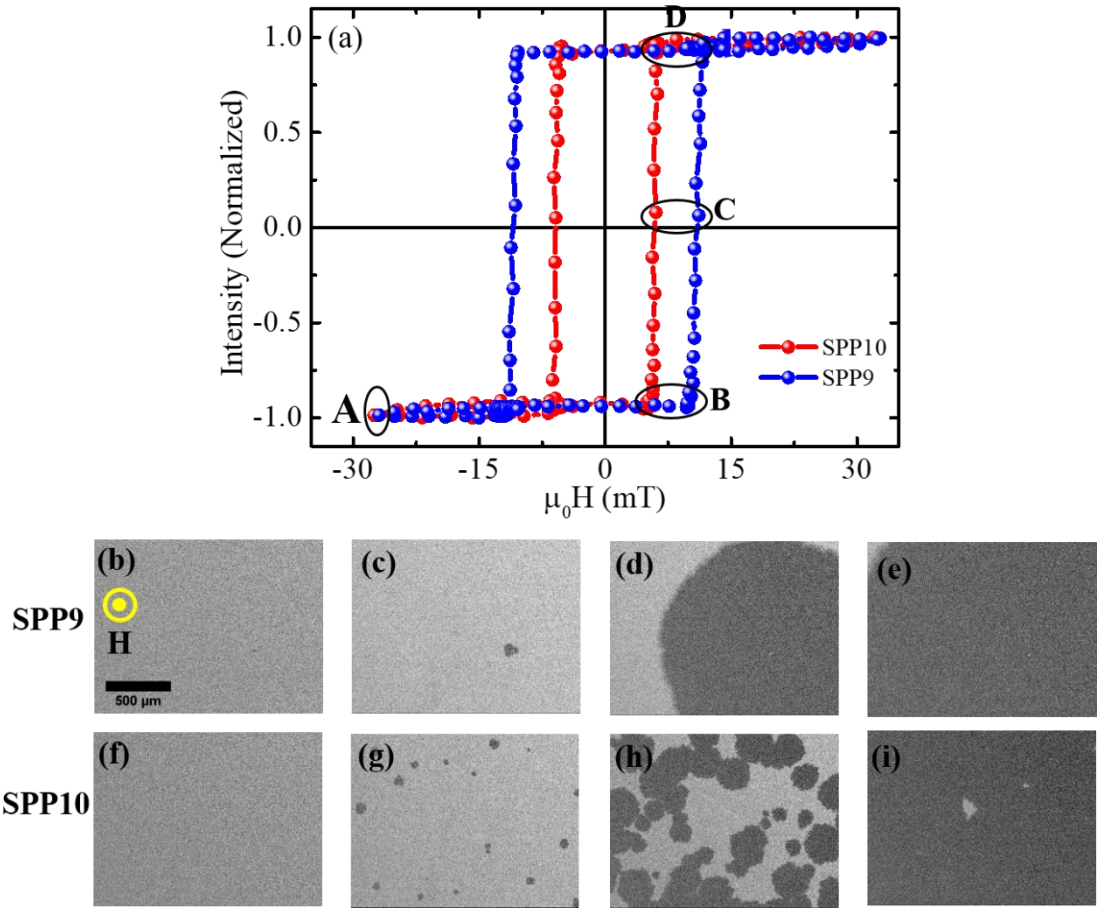

Figure 6.2.1: (a) Hysteresis loops of the samples SPP9 (blue) and SPP10 (red). (b-e) and (f-i) are the domain images for SPP9 and SPP10, respectively. Domain images corresponding to the points A-D of the hysteresis loops shown in (a). Scale bar and the applied field direction are shown in (b) and same for all the images.

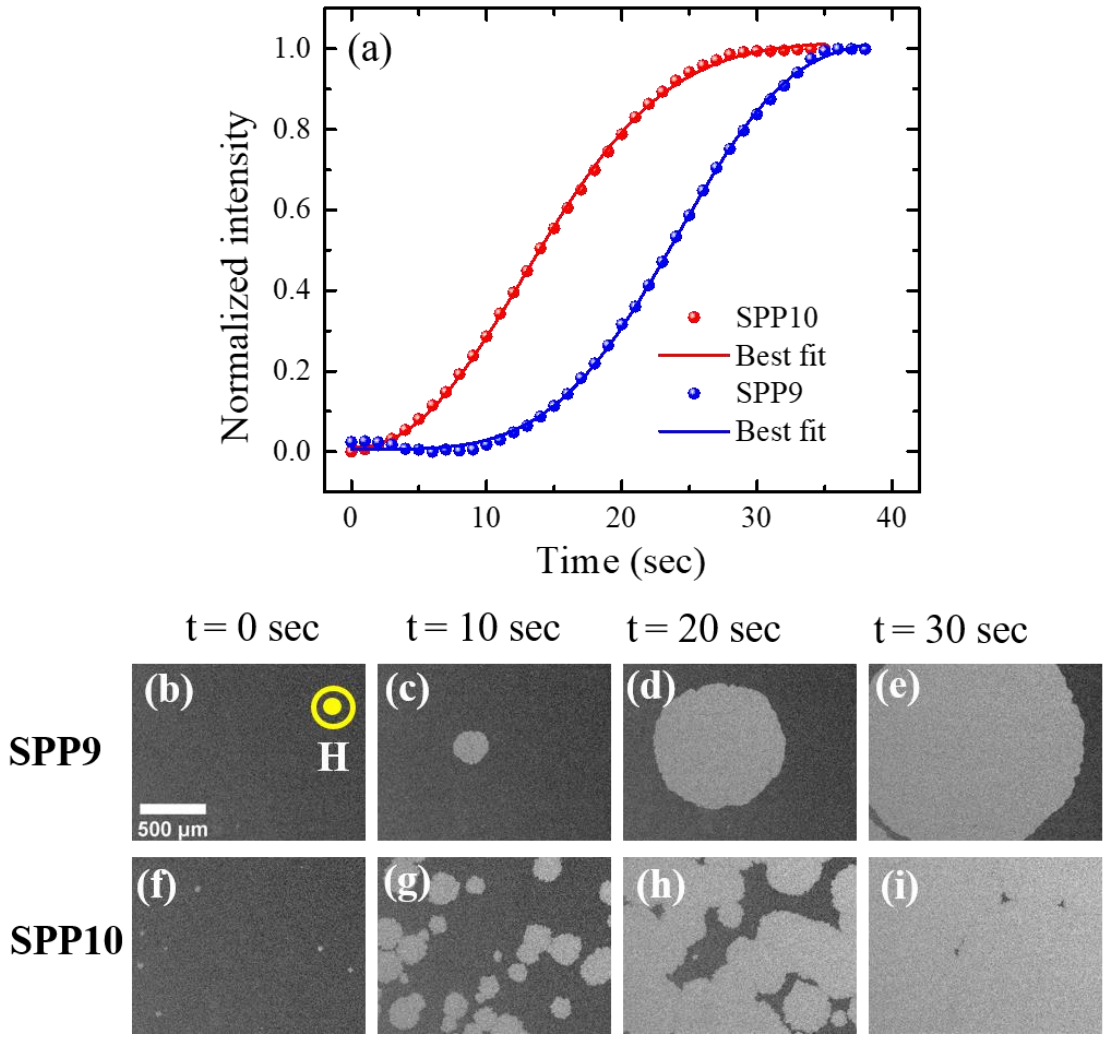

Figure 6.2.2: (a) Relaxation data for all the samples measured at H_M=0.97 H_C, where the blue and red solid circles represent the raw data for SPP9 and SPP10, respectively, and solid lines are the best fits using equation (6.1.1). (b - e) and (f - i) show the domain images for the samples SPP9 and SPP10, repectively, which have been captured at 0, 10, 20 and 30 seconds, respectively. Scale bar and the applied field direction are shown in (b) and same for all the images.

Pd, Co, Ta layers have been deposited using DC magnetron sputtering and C_{60} layer has been deposited using thermal evaporation technique. The hysteresis loops and corresponding domain images are measured using polar MOKE at room temperature. Figure 6.2.1 (a) shows the hysteresis loops of samples SPP9 (blue) and SPP10 (red). Figure 6.2.1 (b-e) and (f-i) show

the domain images corresponding to the points (A-D) marked in the hysteresis loop (a) for SPP9 and SPP10, respectively. Similar to Pt/Co/C_{60}/Pt system, in this case also we have observed reduction in H_C as well as the domain size for the Pd/Co/C_{60}/Pd sample as compared to the Pd/Co/Pd reference sample.

In order to study effect of spinterface on the relaxation time, magnetization relaxation measurements have been performed on SPP9 and SPP10 samples. The similar measurement protocol has been followed. Figure 6.2.2 (a) shows the relaxation behaviour of SPP9 (blue) and SPP10 (red) at $H_M = 0.97\ H_C$, (b – e) and (f - i) show the domain images for SPP9 and SPP10, respectively, which are captured at 0, 10, 20 and 30 sec, respectively. Solid circles represent the experimental data whereas the solid lines are the best fits using the compressed exponential function (equation 6.1.1). The extracted values of τ and β are listed in table 6.2.1. It has been observed that relaxation become faster after inserting a C_{60} layer, as shown in Pt/Co/C_{60}/Pt system. These results show that the effect of spinterface has significant effect on the domain size and relaxation.

Table 6.2.1: Parameters obtained from the best fits of the experimental data shown in figure 6.2.2 using equation 6.1.1.

Sample name	$0.97\ H_C$	
	τ (sec)	β
SPP9	26.04 ± 0.10	2.94 ± 0.05
SPP10	16.68 ± 0.08	2.24 ± 0.03

In summary, the effect of C_{60} on anisotropy, domain size and magnetization relaxation in perpendicular magnetic anisotropic systems (Pt/Co/C_{60}/Pt and Pd/Co/C_{60}/Pd) have been discussed. It has been shown that spinterface can lead to domain engneering. Size of the bubble domains reduces after inserting a C_{60} layer in both Pt/Co/Pt and Pd/Co/Pd thin films. DFT

calculations indicate a strong chemisorption of C_{60} molecules with Co layers. Therefore, at the absorption site (Co-C_{60} interface) the magnetic environment is different from the rest of the Co layer. This modified magnetic environment regulates the nature of magnetic domains which have a C_{60} layer. The spinterface of Co-C_{60} not only reduces the magnetic domain size, it also enhances the magnetic anisotropy of the system as compared to the reference one. The engineering in domain size and tuning the anisotropy are advantageous for memory storage application point of view. Similarly, the speed of magnetic relaxation become faster for the system having C_{60} layer. This fast switching has a remarkable impact in device application. Further, due to the broken inversion symmetry Pt/Co/C_{60}/Pt multilayer structure exhibits a finite amount of iDMI. To explore the possibility of tuning the iDMI to host any chiral magnetic structures, the quantification of iDMI may be performed in future.

CHAPTER 7: Spin pumping and Inverse spin Hall effect (ISHE) at CoFeB/C_{60} interface

Pure spin current has an important role in fabricating power efficient spintronics devices.[68] The generation of pure spin current in FM/NM system by microwave excitation is known as spin pumping. For efficient spin to charge current conversion, high SOC material is needed. Due to the spin dependent scattering, the spin current can be converted into a transverse voltage by inverse spin Hall effect (ISHE).[67,160,161] Spin life time and spin diffusion length (λ_{sd}) are less for heavy metals (HM) as compared to OSCs.[162,163] Due to low SOC and HFI, and large λ_{sd}, OSCs are good for spintronic applications.[19,108,164,165] However, the low value of SOC limits the OSCs for efficient spin to charge conversion. Recently, there is a report on curvature enhanced SOC in C_{60}.[24,166] The strength of SOC consists of intrinsic, Rashba and curvature related terms and can be expressed as: $\zeta = \zeta_{in} + \zeta_{Rashba} + \zeta_{curv}$.[167] The contribution of Rashba term is negligible for C_{60} as it is related to broken inversion symmetry. Therefore, ζ_{curv} may have significant contribution in enhancing the SOC strength of C_{60}. Generation and manipulation of pure spin current in FM/OSC system has not been explored much.[167–171] Conductivity mismatch can be reduced between YIG and Pt by introducing a C_{60} layer.[169,171] Further it also enhances the spin mixing conductance across YIG/C_{60}/Pt interfaces.[169,171] ISHE response in a variety of OSCs have been studied by D. Sun *et al.*,).[168] Using this pulsed FMR technique one can generate two to three orders of larger magnitude of ISHE signal in comparison to simple microwave excitation in a CPW. Sun et al., have observed that among all OSCs, C_{60} shows larger spin current signal and the evaluated θ_{SH} for NiFe/C_{60} system is 0.014.[168] Further, spin pumping in NiFe/C_{60}/Pt system has been reported by Liu *et al.,* .[167,170] In all above-mentioned cases, a Pt layer has been used (which has high SOC) to detect the spin current signal. Here, we have used CPW based FMR set-up to investigate the spin pumping and ISHE in a bilayer CoFeB/C_{60} system without having any HM layer.

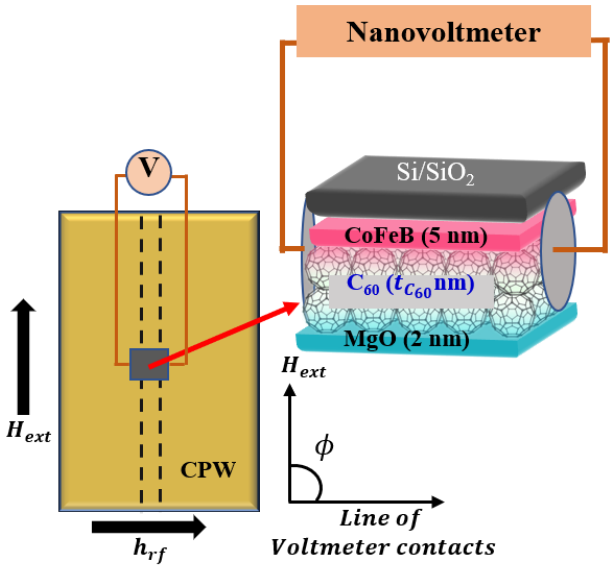

Figure 7.1: Schematic of FMR and ISHE set-up and the sample structure. During the measurement we kept the sample upside down on top of CPW .

The sample structure is shown in figure 7.1 and listed in Table 7.1.

Table 7.1: Detail of the sample structure

Sample name	Sample structure
SPI1	Si/SiO2(native oxide)/CoFeB(5 nm)/MgO (2 nm)
SPI2	Si/SiO2(native oxide)/CoFeB(5 nm)/C_{60}(1.1 nm)MgO (2 nm)
SPI3	Si/SiO2(native oxide)/CoFeB(5 nm)/C_{60}(2 nm)MgO (2 nm)
SPI4	Si/SiO2(native oxide)/CoFeB(5 nm)/C_{60}(5.02 nm)MgO (2 nm)
SPI5	Si/SiO2(native oxide)/CoFeB(5 nm)/C_{60}(15 nm)MgO (2 nm)

Structural characterization and the damping properties of the samples have been discussed in chapter 4. It has been observed that damping increases with increasing the thickness ($t_{C_{60}}$) of C_{60} layer. This increase in α as compared to single layer CoFeB is an indirect indication of spin pumping at CoFeB/C_{60} interface.

The effective spin mixing conductance ($g_{eff}^{\uparrow\downarrow}$) is playing an important role in spin transport phenomenon in FM/NM interface. We have calculated $g_{eff}^{\uparrow\downarrow}$ using the below equation[68].

$$g_{eff}^{\uparrow\downarrow} = \frac{\Delta\alpha 4\pi M_S t_{FM}}{g\mu_B} \tag{7.1}$$

Where $\Delta\alpha$, μ_B, g and t_{FM}, are the change in α due to spin pumping, Bohr magneton, Lande g-factor, and the thickness of CoFeB layer, respectively. The value of M_S for all the samples have been calculated from *M-H* loops measured using SQUID magnetometry. The values of α, $\Delta\alpha$, M_S, g and $g_{eff}^{\uparrow\downarrow}$ are listed in Table 7.2. It has been observed that M_S decreases with C_{60} layer thickness which may be due to the reduction of magnetic moment in CoFeB layer as discussed earlier. It should be noted that $g_{eff}^{\uparrow\downarrow}$ increases with increasing $t_{C_{60}}$. The enhancement of $g_{eff}^{\uparrow\downarrow}$ may be due to the enhanced hybridization in higher $t_{C_{60}}$ with spinterface and/or the reduction in interface roughness by the well growth of C_{60}.

Table 7.2: The values of α, $\Delta\alpha$, M_S, g and $g_{eff}^{\uparrow\downarrow}$ for all the samples

Sample	α	$\Delta\alpha$	g	M_S (emu/cc)	$g_{eff}^{\uparrow\downarrow}$ (m^{-2})
SPI1	0.0095±0.0001	-	2.499±0.009	1015	-
SPI2	0.0106±0.0002	0.0012	2.496±0.014	990	3.55×10^{18}
SPI3	0.0110±0.0002	0.0016	2.503±0.020	970	4.62×10^{18}
SPI4	0.0124±0.0003	0.003	2.596±0.020	960	8.27×10^{18}
SPI5	0.0169±0.0006	0.0072	2.745 ±0.011	945	1.89×10^{19}

In order to study the spin pumping, angle dependent ISHE measurements have been performed at a fixed frequency of 7 GHz and 11 mW power. To measure the ISHE voltage, contacts have been made at the opposite edges of the sample using silver paste. We have measured the voltage using nanovoltmeter (Keithley 2182A). The measurement geometry is shown in figure 7.1 and the detailed methodology has been discussed in chapter 2.

Field dependence ISHE voltage (V_{meas}) and FMR signal for SPI1 is shown in figure 7.2. The red solid circles with line and blue solid circles represent the FMR data and measured ISHE

voltage, respectively. It should be noted that for single layer CoFeB layer, we have not observed any ISHE signal.

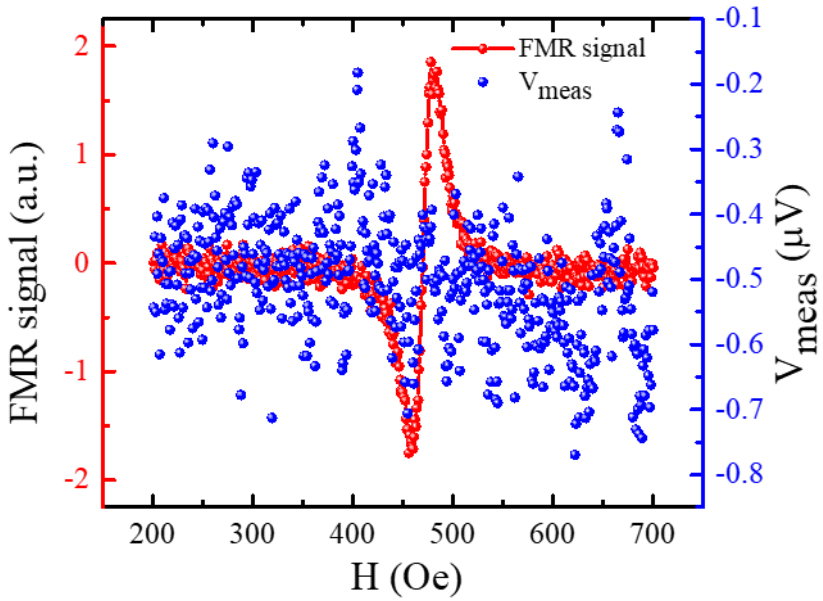

Figure 7.2: FMR signal (red circles with line) and V_{meas} (blue solid circles) vs applied DC magnetic field (H) plot for SPI1 (single layer CoFeB).

Figure 7.3 shows angle dependent ISHE voltage (V_{meas}) and FMR signal vs applied magnetic field (H) plots for SPI2 at $\phi = 0^0$ (a), 30^0 (b), 90^0 (c) and 180^0 (d). Here ϕ is the angle between H and the line of nanovoltmeter contact (shown in figure 7.1). Since, $\boldsymbol{V_{meas} \propto (H \times \sigma)}$, where $\boldsymbol{\sigma}$ is the direction of spin polarization. Therefore, upon changing the direction of $\boldsymbol{H}$, $\boldsymbol{V_{meas}}$ also changes. From figure 7.3 (a) and (d), it has been seen that ISHE signal changes its polarity from 0^0 to 180^0 angle, as the direction of H is reversed. This indicates that the primary signal arises due to the spin pumping at CoFeB/C_{60} interface.

V_{meas} consists of both the symmetric (V_{sym}) and anti-symmetric (V_{asym}) components. To separate the V_{sym} and V_{asym}, we have fitted the experimental data using the following Lorentzian equation[172]:

$$V_{meas} = V_{sym}\frac{(\Delta H)^2}{(H - H_r)^2 + (\Delta H)^2} + V_{asym}\frac{(\Delta H)(H - H_r)}{(H - H_r)^2 + (\Delta H)^2} \qquad (7.2)$$

where, H_r and ΔH are the resonance field and the linewidth, respectively.

In figure 7.3 the red solid lines are the best fits to the equation (7.2), while the red open squares and green open circles represent the V_{sym} and V_{asym} contributions, respectively.

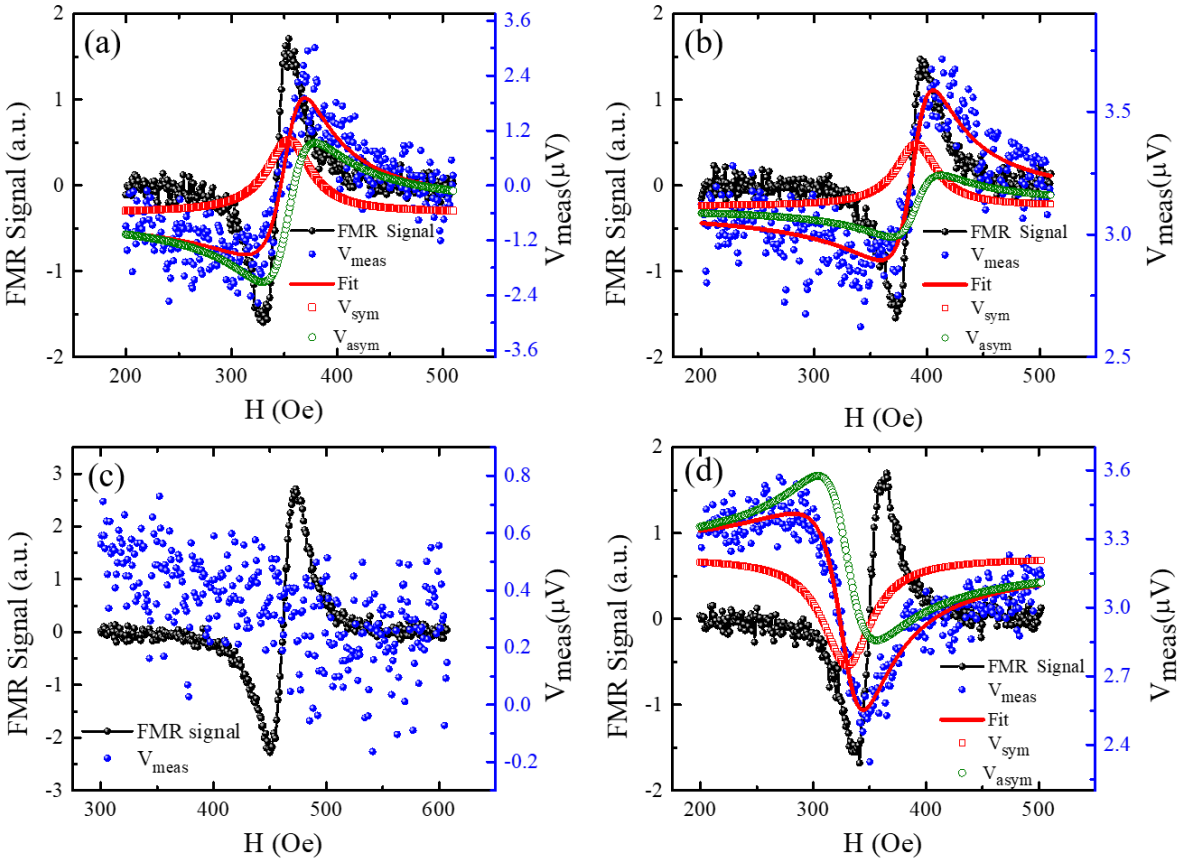

Figure 7.3: FMR signal (black circles with line) and V_{meas} (blue solid circles) vs applied DC magnetic field (H) for the sample SPI2 at (a) 0°, (b) 30°, (c) 90° and (d) 180° angles. Red solid line is the best fit to the equation, while red open squares and green open circles are the V_{sym} and V_{asym} contributions, respectively.

The V_{sym} component majorly contribute in spin pumping and has some minor contributions in anomalous Hall effect (AHE), and anisotropic magnetoresistance (AMR). On the other hand, V_{asym} component has major contribution in AHE and AMR. To quantify the spin pumping voltage (V_{SP}) and the other rectification effects such as AMR perpendicular ($V_{AMR}^{\perp}$), AMR parallel ($V_{AMR}^{\parallel}$), AHE voltage (V_{AHE}), in-plane angle dependent ISHE measurements have been performed by varying ϕ in 5° intervals.

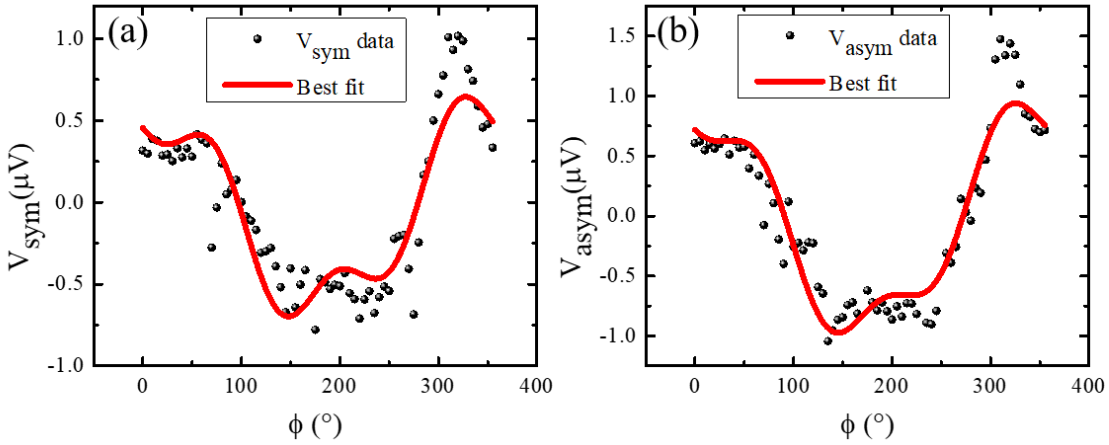

Figure 7.4: Angle dependence of V_{sym} (a) and V_{asym} (b) for samples SPI2. Black solid circles are the experimental data and red solid lines are the best fits using equations 7.3 and 7.4.

Figure 7.4 show the V_{sym} vs ϕ (a) and V_{asym} vs ϕ (b) plots for SPI2. Black solid circles represent the experimental data and red solid lines are the best fits. The symmetric and anti-symmetric parts are fitted using the following equation[173]:

$$V_{sym} = V_{SP}\cos^3(\phi) + V_{AHE}\cos(\phi)\cos(\Phi) + V_{sym}^{AMR\perp}\cos(2\phi)\cos(\phi) + V_{sym}^{AMR\parallel}\sin(2\phi)\cos(\phi) \quad (7.3)$$

$$V_{asym} = V_{AHE}\cos(\phi)\sin(\Phi) + V_{asym}^{AMR\perp}\cos(2\phi)\sin(\phi) + V_{asym}^{AMR\parallel}\sin(2\phi)\cos(\phi) \quad (7.4)$$

where, Φ is defined as the relative phase between the microwave electric and magnetic fields in the medium and here, $\Phi = 90°$.

All the bilayer samples (with C_{60}) show clear ISHE signal. Figure 7.5, 7.7 and 7.9 show H dependence on V_{meas} at different ϕ for the samples SPI3, SPI4 and SPI5, respectively. Angle dependence of V_{sym} (a) and V_{asym} (b) components for SPI3, SPI4 and SPI5 have been shown in figure 7.6, 7.8 and 7.10, respectively. In all the samples, we have observed negligible ISHE signal at $\phi = 90°$ and from 0^0 to 180^0, the signal changes its polarity. The values of V_{SP}, V_{AHE}, $V_{AMR}^{\perp}$, $V_{AMR}^{\parallel}$ obtained from the fitting of the experimental data using equations 7.3 and 7.4 are listed in table 7.3. It has been observed that V_{SP} increases with C_{60} thickness.

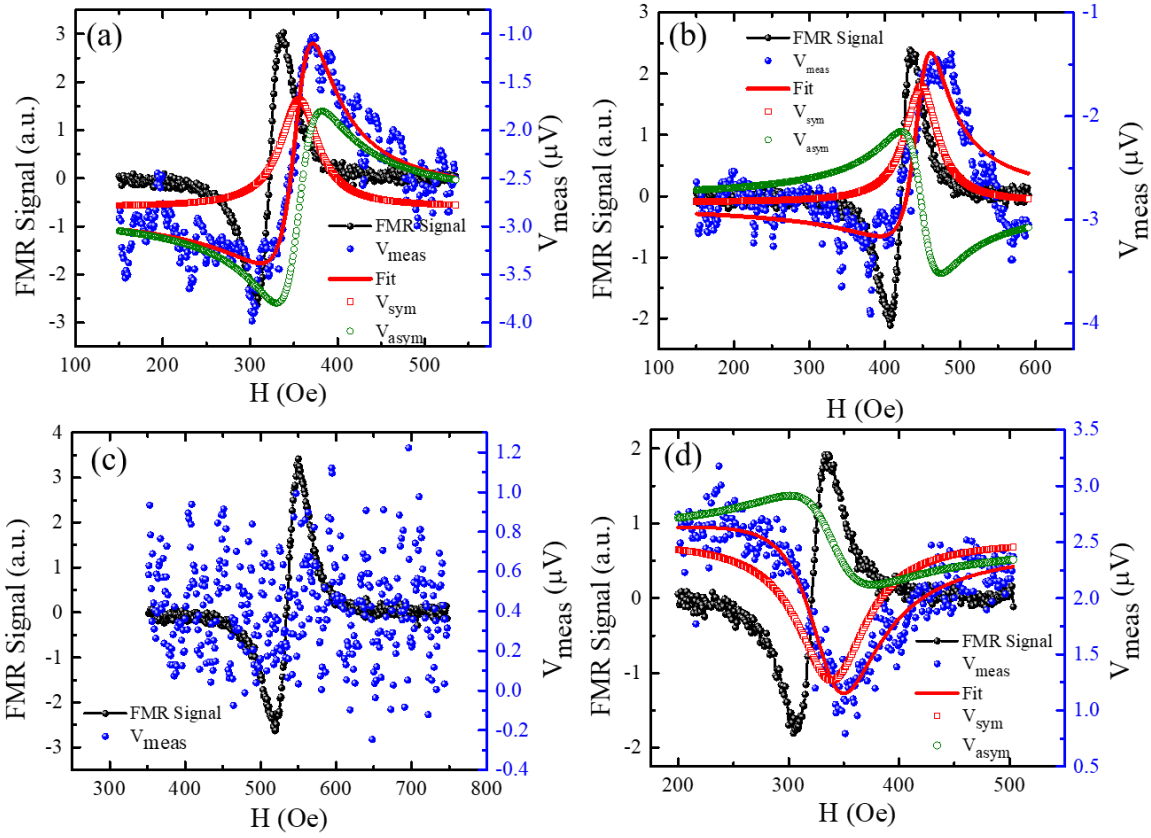

Figure 7.5: FMR signal (black circles with line) and V_{meas} (blue solid circles) vs applied DC magnetic field (H) for the sample SPI3 at (a) 0°, (b) 30°, (c) 90° and (d) 180° angles. Solid red line is the best fit to the equation, while red open square and green open circle are the V_{sym} and V_{asym} contributions, respectively.

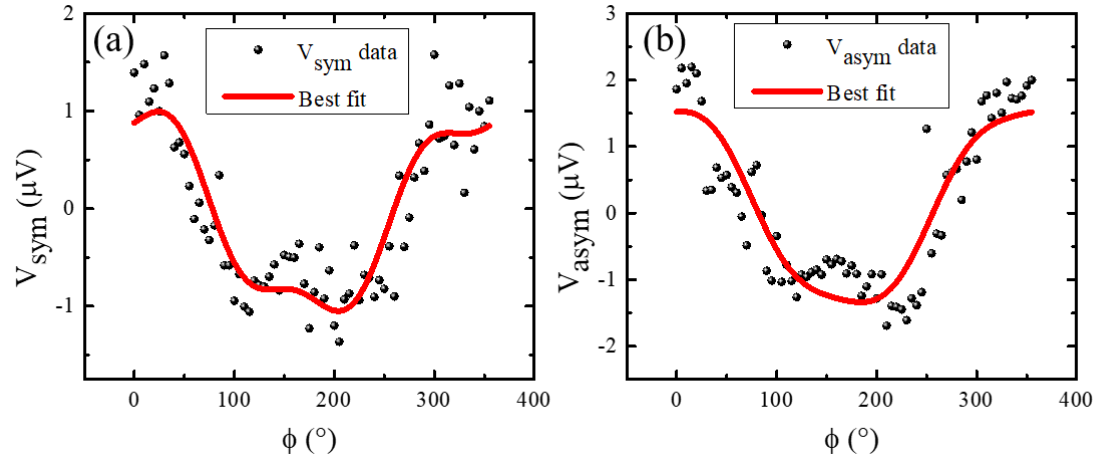

Figure 7.6: Angle dependent V_{sym} (a) and V_{asym} (b) components for samples SPI3. Black solid circles are the experimental data, while the red solid lines are the best fits using equations 7.3 and 7.4.

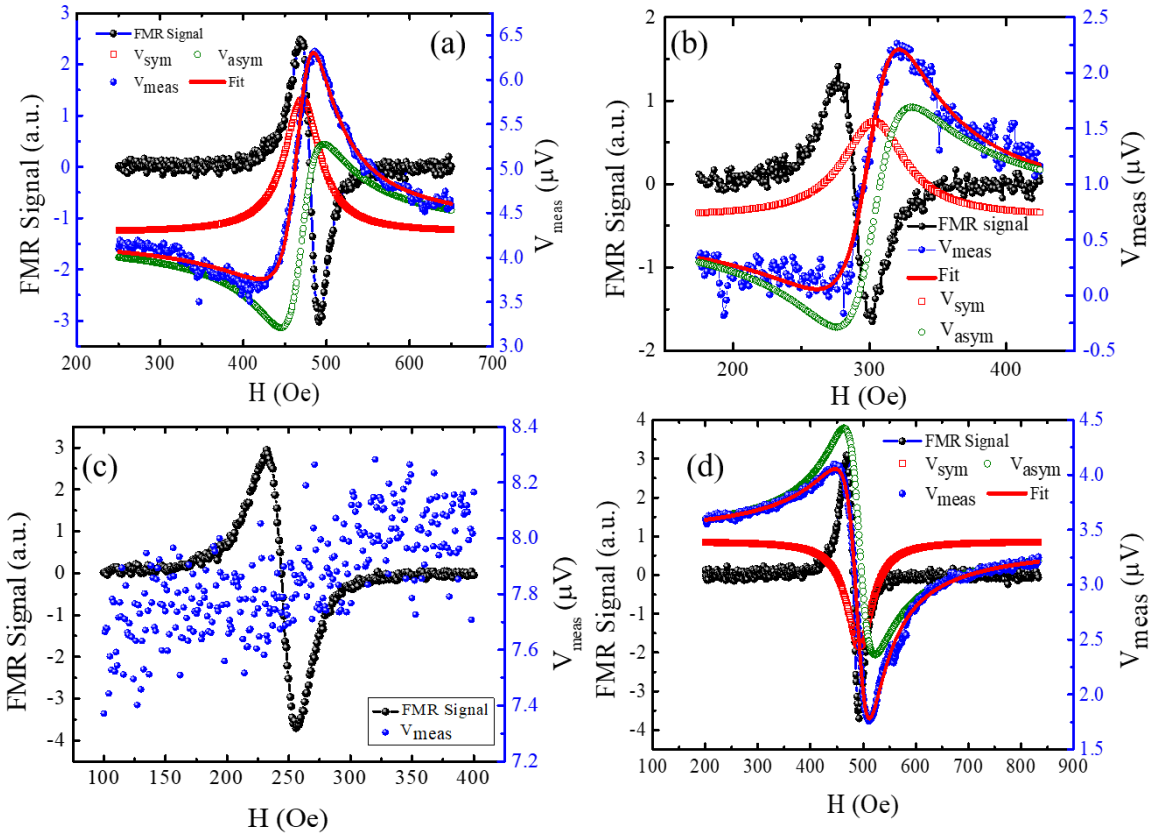

Figure 7.7: FMR signal (black circles with line) and V_{meas} (blue solid circles) vs applied DC magnetic field (*H*) for the sample SPI4 at (a) 0°, (b) 30°, (c) 90° and (d) 180° angles. Solid red line is the best fit to the equation, while red open squares and green open circles are the V_{sym} and V_{asym} contributions, respectively.

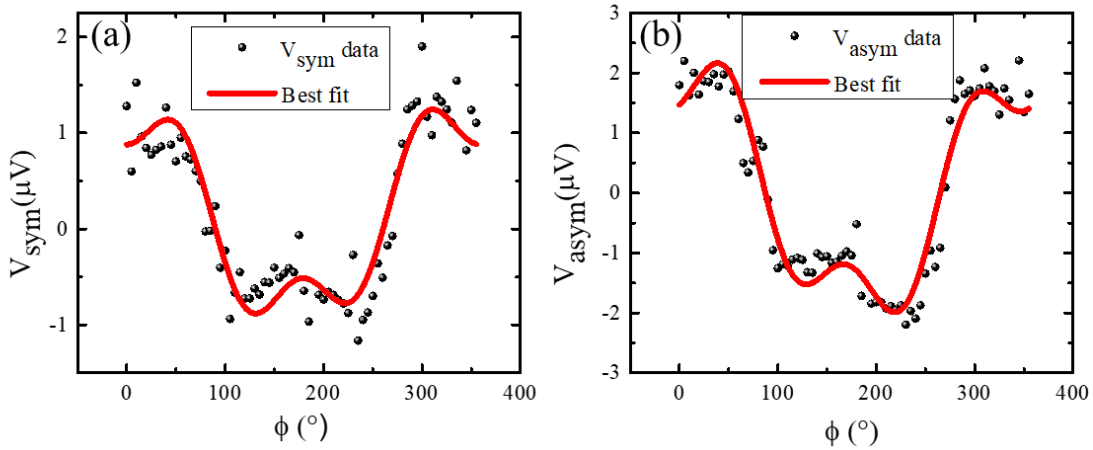

Figure 7.8: Angle dependent V_{sym} (a) and V_{asym} (b) components for sample SPI4. Black solid circles are the experimental data, while the red solid lines are the best fits using equations 7.3 and 7.4.

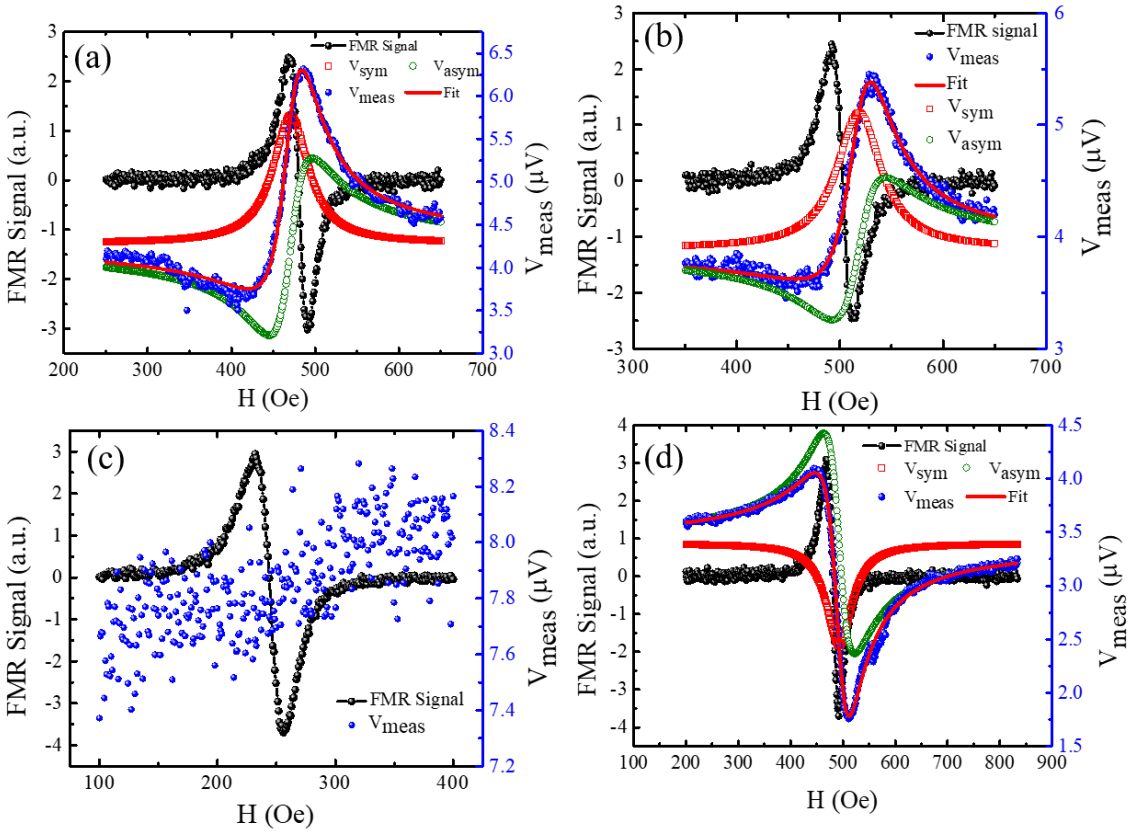

Figure 7.9: FMR signal (black circles with line) and V_{meas} (blue solid circles) vs applied DC magnetic field (H) for the sample SPI5 at (a) 0°, (b) 30°, (c) 90° and (d) 180° angles. Solid red line is the best fit to the equation, while red open squares and green open circles are the V_{sym} and V_{asym} contributions, respectively.

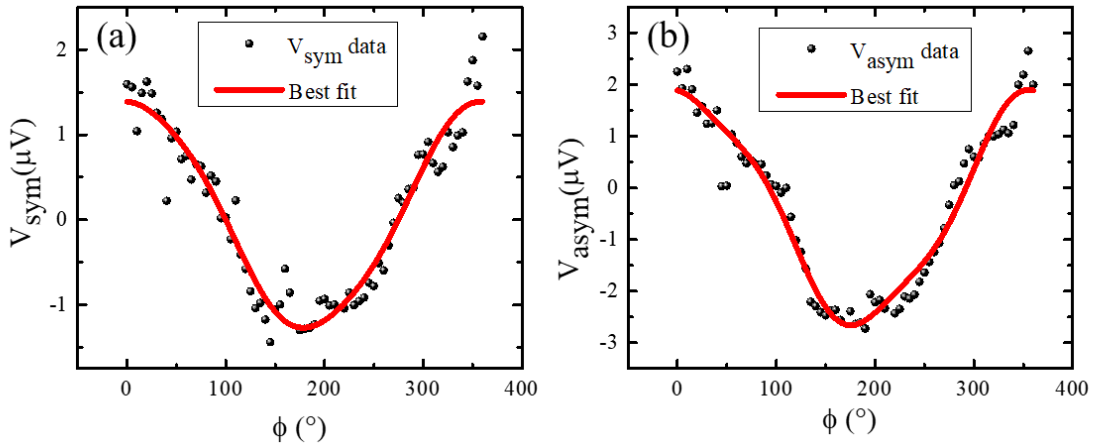

Figure 7.10: Angle dependent V_{sym} (a) and V_{asym} (b) components for sample SPI5. Black solid circles are the experimental data, while the red solid lines are the best fits using equations 7.3 and 7.4.

Table 7.3: Fitted parameters from angle dependent ISHE measurements for all the samples

Sample	V_{SP} (mV)	$V_{Sym}^{AMR\perp}$(μV)	$V_{Sym}^{AMR\parallel}$(μV)	V_{AHE}^{asym} (μV)	$V_{Asym}^{AMR\perp}$(μV)	$V_{Asym}^{AMR\parallel}$(μV)
SPI2	2.34±0.11	-1.52±0.08	0.16±0.05	1.11±0.06	-0.38±0.08	-0.20±0.06
SPI3	2.66±0.20	-1.74±0.21	0.14±0.08	1.65±0.12	-0.25±0.17	-0.14±0.08
SPI4	2.68±0.13	-1.06±0.14	0.10±0.08	2.18±0.21	-1.27±0.25	-0.32±0.25
SPI5	2.85±0.15	-1.46±0.12	0.10±0.08	2.24±0.09	-0.10±0.06	-0.39±0.11

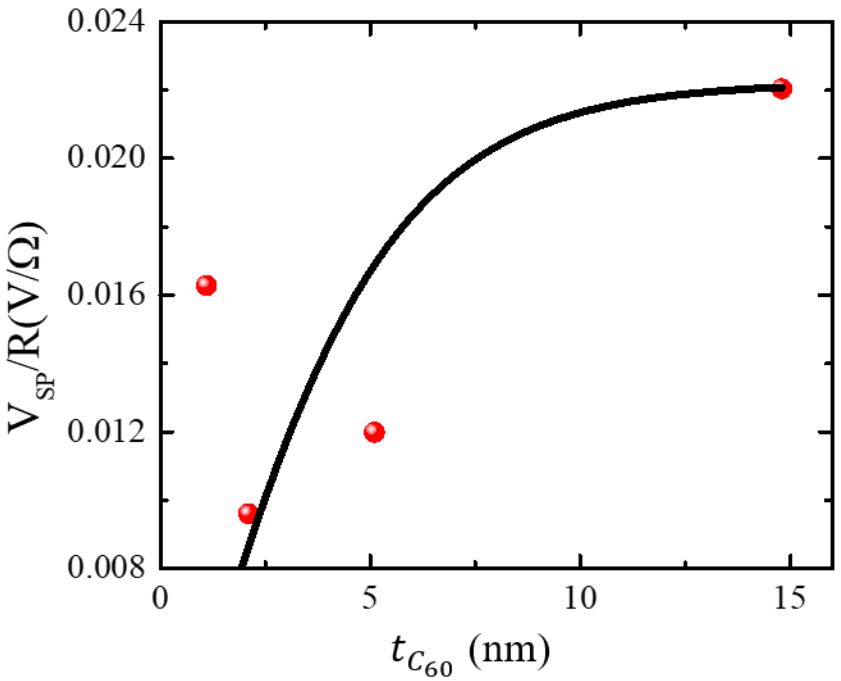

Figure 7.11: $t_{C_{60}}$ vs normalized spin pumping voltage V_{SP}/R plot. Red solid circles are the experimental data and black solid line is the best fit using equation 7.5.

Further, we have calculated the θ_{SH} and $\lambda_{C_{60}}$ for C_{60} using a spin diffusion model which is given below.[68,174,175]

$$\frac{V_{SP}}{R} = (w) \times \theta_{SH}\lambda_{C_{60}} \tanh\left(\frac{t_{C_{60}}}{2\lambda_{C_{60}}}\right)|\vec{J_S}| \qquad (7.5)$$

where,

$$|\overrightarrow{J_S}| \approx \left(\frac{\hbar g_{eff}^{\uparrow\downarrow}}{8\pi}\right)\left(\frac{\mu_0 h_{rf}\gamma}{\alpha}\right)^2 \times \left[\frac{\mu_0 M_S\gamma+\sqrt{(\mu_0 M_S\gamma)^2+16(\pi f)^2}}{(\mu_0 M_S\gamma)^2+16(\pi f)^2}\right]\left(\frac{2e}{\hbar}\right) \quad (7.6)$$

Here, γ, μ_0, $\hbar$, f and e denote the gyromagnetic ratio, free space permeability, reduced Planck's constant, resonance frequency and charge of an electron, respectively.

The resistance (R) of the samples have been measured using the four-probe method. The values of the CPW transmission line width (w) and RF field ($\mu_0 h_{rf}$) are 200 mm and 0.05 mT, respectively. Thickness ($t_{C_{60}}$) dependence of $\frac{V_{SP}}{R}$ is shown in figure 7.11. The red solid circles are the experimental data and black solid line is the best fit using equation (7.5). We found that the value of $\lambda_{C_{60}}$ for CoFeB/C_{60} system is ~ 2.5 nm. The obtained value of $\theta_{SH} g_{eff}^{\uparrow\downarrow}$= $1.04 \times 10^{18}\, m^{-2}$. The value of θ_{SH} is found to be ~ 0.055. However, due to less numbers of samples, the fitting of $\frac{V_{SP}}{R}$ vs $t_{C_{60}}$ is not so good. Further studies are needed to evaluate the $\lambda_{C_{60}}$ and θ_{SH}.

In summary, we have studied spin pumping and ISHE in CoFeB/C_{60} bilayer systems by varying the C_{60} thickness. ISHE measurements have been performed using simple microwave excitation in a CPW. To disentangle the spin rectification effect such as AMR, AHE etc. angle dependent ISHE measurements have been performed. The possible reason behind the spin pumping at CoFeB/C_{60} interface is may be due to curvature enhanced SOC in C_{60}[166]. Damping, spin pumping voltage and effective spin mixing conductance monotonically increase with C_{60} thickness. The obtained spin Hall angle for CoFeB/C_{60} bilayer system is ~ 0.055. Future research is needed to understand the underline mechanism of the curvature enhanced SOC and spin pumping effect at FM/OSC interface.

CHAPTER 8: Summary and Conclusion

The main focus of this thesis is to study the spinterface physics in metal (M)/ organic semiconductor (OSC) heterostructures where the metal is a non-ferromagnetic or ferromagnetic (FM) material. Our aim is to control the magnetic properties of such heterostructures by formation of spinterface. We have prepared high quality multilayer thin films and studied their magnetic properties e.g., magnetic anisotropy, domain structure, damping etc. The samples have been prepared using magnetron sputtering (DC, RF), thermal evaporation and e-beam evaporation techniques. To characterize the growth of the thin films high resolution transmission electron microscopy (HRTEM) and X-ray reflectivity (XRR) measurements have been performed. We have performed hysteresis loop measurements along with domain images using magneto-optic Kerr effect (MOKE) based microscopy to study the effect of spinterface on magnetization reversal, magnetic domains and magnetization relaxation. Field dependent magnetization measurements have been performed using superconducting quantum interference device (SQUID) magnetometer at different temperature to calculate the saturation magnetization of the samples. Further, magnetic anisotropy, magnetic damping has been calculated using coplanar waveguide (CPW) based ferromagnetic resonance (FMR) measurements. To study the spin pumping and inverse spin Hall effect (ISHE) at FM/OSC interface we have performed angle dependent ISHE measurements using the same FMR set up. First, we have focused on non-FM/OSC system. It has been observed that ferromagnetism can be induced in a non-FM/OSC system e.g., Cu/C_{60}. Due to the charge transfer and interface reconstruction at the Cu – C_{60} interface, the density of states (DOS) of the Cu layer has been modified which leads to induced magnetism in Cu. To quantify the element specific magnetic moment X-ray magnetic circular dichroism (XMCD) measurements have been performed which revealed ~ 0.01 μ_B/atom magnetic moment in Cu at the Cu/C_{60} interface.

Next, we move to the FM/OSC heterostructures in which the spinterface is very much crucial to inject the spin into the OSC layer. We considered in-plane CoFeB/C_{60} and Co/Rubrene systems and studied the effect of spinterface on the global anisotropy, magnetic domains and damping. In case of CoFeB/C_{60} in-plane magnetized system, it has been observed that the magnetic anisotropy is more for CoFeB/C_{60} bilayer samples as compared to the reference CoFeB film. It further increases with increase in the thickness of the C_{60} layer. Similarly, damping of the system is also enhanced after introduction of a C_{60} layer and increases with the C_{60} thickness. However, there is almost no change in the magnetization reversal and domain structure in the bilayer CoFeB/C_{60} samples as compared to the reference CoFeB film. The domains in CoFeB/C_{60} are different to Co/C_{60} and Fe/C_{60} systems.[33–35] Afterwards, we have observed that the anisotropy as well as domain size increases in bilayer Co/Rubrene samples as compared to single layer Co film, which is very similar to in-plane Co/C_{60} system. Further, we have focused on the perpendicular magnetic anisotropy (PMA) based Pt/Co/C_{60}/Pt and Pd/Co/C_{60}/Pd systems. In both cases, it has been observed that domain size got reduced after inserting a C_{60} layer. However, the shape of the domain remains same and bubble domains have been observed for all the systems. To study the relaxation dynamics, we have performed magnetization relaxation measurements at sub-coercive fields. It has been observed that relaxation time decreases (i.e., faster relaxation) after introduction of a C_{60} layer and it further decreases with C_{60} thickness. The effective anisotropy increases in Pt/Co/C_{60}/Pt systems as compared to Pt/Co/Pt system which is further confirmed using density functional theory (DFT) calculations. The possible reason behind this enhancement in anisotropy might be due to the hybridization and formation of interface at Co-C_{60} interface. This increase in anisotropy is responsible for the decrease in domain size and faster relaxation. The nature of the spinterface has been explored applying DFT calculations. Charge (e^-) transfer is happening from top layer of Co to C atoms, which are bonded to substrate Co atoms. There is a decrease in magnetic

moments (1.3 - 1.5 μ_B) for the bonded Co-atoms. The $p_\pi - d_\pi$ interaction between the chemisorbed C_{60} and the Co atoms modify the magnetic environments which affect the anisotropy, domain size and relaxation time of the system having C_{60} layer.

Although C_{60} is expected to exhibit low spin-orbit coupling (SOC), the curvature of C_{60} may enhance the SOC[166]. The best way to check the SOC is to study the spin pumping via inverse spin Hall effect (ISHE) experiments. In this regard, we have performed detailed ISHE experiments in CoFeB/C_{60} systems and have observed the spin pumping at CoFeB/C_{60} interface which is indirect evidence that C_{60} exhibits reasonable SOC. This shows the usefulness of OSC for future spin-to-charge conversion based spintronic devices.

The results explained in this thesis show that spinterface in M/OSC heterostructures exhibits novel physics and main messages of this thesis are expressed in the following:

1. Ferromagnetism has been observed in non-magnetic Cu/C_{60} systems and XMCD measurements reveal that Cu exhibits ~ 0.01 μ_B/atom magnetic moment at the Cu/C_{60} interface.
2. In both the in-plane and out-of-plane magnetized systems, spinterface can enhance the global anisotropy of the system.
3. Similar to polycrystalline Co/C_{60}, domain size increases in Co/Rubrene system. However, in amorphous CoFeB/C_{60} nominal changes in domain structure have been observed as compared to single layer CoFeB system.
4. Relaxation becomes fast for Pt/Co/C_{60}/Pt and Pd/Co/C_{60}/Pd systems as compared to the reference Pt/Co/Pt and Pd/Co/Pd systems, respectively. A strong chemosorption between C_{60} and Co atoms is responsible for this fast relaxation. This fast switching has a remarkable impact in device application.

5. Curvature enhanced SOC in C_{60} has been reported in literature. In this context, the results on angle dependent ISHE measurements at CoFeB/C_{60} bilayers clearly evidence that C_{60} exhibits reasonable SOC.

In future, theory work is needed to understand the exact mechanism behind the change or no change of domains due to the spinterface in amorphous ferromagnetic systems. In order to evaluate the spinterface thickness and induced magnetic moment, polarized neutron reflectometry measurement should be performed on CoFeB/C_{60} systems. Future studies are required to understand the underlying mechanism of the curvature enhanced SOC and spin pumping at FM/OSC interface. Further in Pt/Co/C_{60}/Pt and Pd/Co/C_{60}/Pd multilayer structures it is expected to have a finite amount of interfacial Dzyaloshinskii-Moriya interaction (iDMI). The quantification of iDMI is needed to be performed to explore the possibility of tuning of iDMI to host any chiral magnetic structures.

References:

[1] M. Julliere, Phys. Lett. **54**, 2 (1975).

[2] M.N. Baibich, J.M. Broto, A. Fert, F.N.V. Dau, F. Petroff, P. Etienne, G. Creuzet, A. Friederich, and J. Chazelas, Phys. Rev. Lett. **61**, 4 (1988).

[3] G. Binasch, P. Grünberg, F. Saurenbach, and W. Zinn, Phys. Rev. B **39**, 4828 (1989).

[4] S.A. Wolf, D.D. Awschalom, R.A. Buhrman, J.M. Daughton, M.L. Roukes, A.Y. Chtchelkanova, and D.M. Treger, **294**, 9 (2001).

[5] S.D. Sarma, Rev Mod Phys **76**, 88 (2004).

[6] C.N.R. Rao and A.K. Cheetham, Science **272**, 369 (1996).

[7] W.J.M. Naber, S. Faez, and W.G. van der Wiel, J. Phys. Appl. Phys. **40**, R205 (2007).

[8] V. Dediu, M. Murgia, F.C. Matacotta, C. Taliani, and S. Barbanera, Solid State Commun. 4 (2002).

[9] Z.H. Xiong, D. Wu, Z.V. Vardeny, and J. Shi, **427**, 4 (2004).

[10] X. Lou, C. Adelmann, S.A. Crooker, E.S. Garlid, J. Zhang, K.S.M. Reddy, S.D. Flexner, C.J. Palmstrøm, and P.A. Crowell, **3**, 6 (2007).

[11] J. Devkota, R. Geng, R.C. Subedi, and T.D. Nguyen, Adv. Funct. Mater. **26**, 3881 (2016).

[12] C.W. Tang, Appl. Phys. Lett. **48**, 183 (1986).

[13] A.J. Heeger, Adv. Mater. **26**, 10 (2014).

[14] A. Tsumura, H. Koezuka, and T. Ando, Appl. Phys. Lett. **49**, 1210 (1986).

[15] C. d. Dimitrakopoulos and P. r. l. Malenfant, Adv. Mater. **14**, 99 (2002).

[16] C.W. Tang and S.A. VanSlyke, Appl. Phys. Lett. **51**, 913 (1987).

[17] B.W. D'Andrade and S.R. Forrest, Adv. Mater. **16**, 1585 (2004).

[18] S. Reineke, M. Thomschke, B. Lüssem, and K. Leo, Rev. Mod. Phys. **85**, 1245 (2013).

[19] V.A. Dediu, L.E. Hueso, I. Bergenti, and C. Taliani, Nat. Mater. **8**, 707 (2009).

[20] T.D. Nguyen, E. Ehrenfreund, and Z.V. Vardeny, Science **337**, 204 (2012).

[21] C. Barraud, P. Seneor, R. Mattana, S. Fusil, K. Bouzehouane, C. Deranlot, P. Graziosi, L. Hueso, I. Bergenti, V. Dediu, F. Petroff, and A. Fert, Nat. Phys. **6**, 615 (2010).

[22] W. Yang, Q. Shi, T. Miao, Q. Li, P. Cai, H. Liu, H. Lin, Y. Bai, Y. Zhu, Y. Yu, L. Deng, W. Wang, L. Yin, D. Sun, X.-G. Zhang, and J. Shen, Nat. Commun. **10**, 3877 (2019).

[23] X. Zhang, Q. Ma, K. Suzuki, A. Sugihara, G. Qin, T. Miyazaki, and S. Mizukami, ACS Appl. Mater. Interfaces **7**, 4685 (2015).

[24] M. Gobbi, F. Golmar, R. Llopis, F. Casanova, and L.E. Hueso, Adv. Mater. **23**, 1609 (2011).

[25] S.W. Jiang, P. Wang, S.C. Jiang, B.B. Chen, M. Wang, Z.S. Jiang, and D. Wu, SPIN **04**, 1440008 (2014).

[26] A. Ozbay, E.R. Nowak, Z.G. Yu, W. Chu, Y. Shi, S. Krishnamurthy, Z. Tang, and N. Newman, Appl. Phys. Lett. **95**, 232507 (2009).

[27] J.-W. Yoo, C.-Y. Chen, H.W. Jang, C.W. Bark, V.N. Prigodin, C.B. Eom, and A.J. Epstein, Nat. Mater. **9**, 638 (2010).

[28] V.N. Prigodin, J.W. Yoo, H.W. Jang, C. Kao, C.B. Eom, and A.J. Epstein, J. Phys. Conf. Ser. **292**, 012001 (2011).

[29] B. Li, C.-Y. Kao, J.-W. Yoo, V.N. Prigodin, and A.J. Epstein, Adv. Mater. **23**, 3382 (2011).

[30] S. Sanvito, Nat. Phys. **6**, 562 (2010).

[31] T. Moorsom, M. Wheeler, T. Mohd Khan, F. Al Ma'Mari, C. Kinane, S. Langridge, D. Ciudad, A. Bedoya-Pinto, L. Hueso, G. Teobaldi, V.K. Lazarov, D. Gilks, G. Burnell, B.J. Hickey, and O. Cespedes, Phys. Rev. B **90**, 125311 (2014).

[32] T.L.A. Tran, P.K.J. Wong, M.P. de Jong, W.G. van der Wiel, Y.Q. Zhan, and M. Fahlman, Appl. Phys. Lett. **98**, 222505 (2011).

[33] S. Mallik, S. Mattauch, M.K. Dalai, T. Brückel, and S. Bedanta, Sci. Rep. **8**, 5515 (2018).

[34] S. Mallik, A.S. Mohd., A. Koutsioubas, S. Mattauch, B. Satpati, T. Br uckel, and S. Bedanta, Nanotechnology **30**, 435705 (2019).

[35] S. Mallik, P. Sharangi, B. Sahoo, S. Mattauch, T. Brückel, and S. Bedanta, Appl. Phys. Lett. **115**, 242405 (2019).

[36] K. Bairagi, A. Bellec, V. Repain, C. Chacon, Y. Girard, Y. Garreau, J. Lagoute, S. Rousset, R. Breitwieser, Y.-C. Hu, Y.C. Chao, W.W. Pai, D. Li, A. Smogunov, and C. Barreteau, Phys. Rev. Lett. **114**, 247203 (2015).

[37] F.A. Ma'Mari, T. Moorsom, G. Teobaldi, W. Deacon, T. Prokscha, H. Luetkens, S. Lee, G.E. Sterbinsky, D.A. Arena, D.A. MacLaren, M. Flokstra, M. Ali, M.C. Wheeler, G. Burnell, B.J. Hickey, and O. Cespedes, Nature **524**, 69 (2015).

[38] F. Al Ma'Mari, M. Rogers, S. Alghamdi, T. Moorsom, S. Lee, T. Prokscha, H. Luetkens, M. Valvidares, G. Teobaldi, M. Flokstra, R. Stewart, P. Gargiani, M. Ali, G. Burnell, B.J. Hickey, and O. Cespedes, Proc. Natl. Acad. Sci. **114**, 5583 (2017).

[39] S. Liang, R. Geng, B. Yang, W. Zhao, R. Chandra Subedi, X. Li, X. Han, and T.D. Nguyen, Sci. Rep. **6**, 19461 (2016).

[40] B.B. Singh, S.K. Jena, M. Samanta, K. Biswas, B. Satpati, and S. Bedanta, Phys. Status Solidi RRL - Rapid Res. Lett. **13**, 1800492 (2019).

[41] P. Gupta, B.B. Singh, K. Roy, A. Sarkar, M. Waschk, T. Brueckel, and S. Bedanta, Nanoscale **13**, 2714 (2021).

[42] K. Roy, A. Mishra, P. Gupta, S. Mohanty, B.B. Singh, and S. Bedanta, J. Phys. D: Appl. Phys. (2021).

[43] T.D. Nguyen, F. Wang, X.-G. Li, E. Ehrenfreund, and Z.V. Vardeny, Phys. Rev. B **87**, 075205 (2013).

[44] E.C. Stoner, Proc. R. Soc. Lond. Ser. Math. Phys. Sci. **165**, 372 (1938).

[45] E.C. Stoner, Proc. R. Soc. Lond. Ser. Math. Phys. Sci. **169**, 339 (1939).

[46] M. Getzlaff, *Fundamentals of Magnetism* (Springer, Berlin ; New York, 2008).

[47] B.D. Cullity and C.D. Graham, *Introduction to Magnetic Materials*, 2nd ed (IEEE/Wiley, Hoboken, N.J, 2009).

[48] D. Sander, J. Phys. Condens. Matter **16**, R603 (2004).

[49] I.-G. Baek, H.G. Lee, H.-J. Kim, and E. Vescovo, Phys. Rev. B **67**, 075401 (2003).

[50] R. Zdyb and E. Bauer, Phys. Rev. B **67**, 134420 (2003).

[51] P. Sharma, H. Kimura, A. Inoue, E. Arenholz, and J.-H. Guo, Phys. Rev. B **73**, 052401 (2006).

[52] P. Weiss, J. Phys. Théorique Appliquée **6**, 661 (1907).

[53] A. Hubert and R. Schäfer, *Magnetic Domains: The Analysis of Magnetic Microstructures* (Springer, Berlin ; New York, 1998).

[54] K.J. Sixtus and L. Tonks, Phys. Rev. **37**, 930 (1931).

[55] S. Mallik, N. Chowdhury, and S. Bedanta, AIP Adv. **4**, 097118 (2014).

[56] S. Mallick, S. Mallik, B.B. Singh, N. Chowdhury, R. Gieniusz, A. Maziewski, and S. Bedanta, J. Phys. Appl. Phys. **51**, 275003 (2018).

[57] N. Chowdhury, W. Kleemann, O. Petracic, F. Kronast, A. Doran, A. Scholl, S. Cardoso, P. Freitas, and S. Bedanta, Phys. Rev. B **98**, 134440 (2018).

[58] Y. Wang, C. Nelson, A. Melville, B. Winchester, S. Shang, Z.-K. Liu, D.G. Schlom, X. Pan, and L.-Q. Chen, Phys. Rev. Lett. **110**, 267601 (2013).

[59] P. Sigmund, Phys. Rev. **184**, 383 (1969).

[60] T.L. Gilbert, Phys Rev **100**, 1243 (1955).

[61] J. Olmsted and G.M. Williams, *Chemistry: The Molecular Science* (Jones & Bartlett Learning, 1997).

[62] J. Stöhr and H.C. Siegmann, *Magnetism: From Fundamentals to Nanoscale Dynamics* (Springer, Berlin ; New York, 2006).

[63] K.V. Raman, Appl. Phys. Rev. **1**, 031101 (2014).

[64] K. Bairagi, A. Bellec, V. Repain, C. Fourmental, C. Chacon, Y. Girard, J. Lagoute, S. Rousset, L. Le Laurent, A. Smogunov, and C. Barreteau, Phys. Rev. B **98**, 085432 (2018).

[65] Shen, Shun-Qing. "Spintronics and spin current." *AAPPS Bulletin* 18.5 (2008): 29.

[66] P. Barla, V.K. Joshi, and S. Bhat, J. Comput. Electron. **20**, 805 (2021).

[67] Y. Tserkovnyak, A. Brataas, and G.E.W. Bauer, Phys. Rev. B **66**, 224403 (2002).

[68] Y. Tserkovnyak, A. Brataas, G.E.W. Bauer, and B.I. Halperin, Rev Mod Phys **77**, 47 (2005).

[69] M.V. Costache, S.M. Watts, C.H. van der Wal, and B.J. van Wees, Phys. Rev. B **78**, 064423 (2008).

[70] Y.K. Kato, Science **306**, 1910 (2004).

[71] E. Saitoh, M. Ueda, H. Miyajima, and G. Tatara, Appl. Phys. Lett. **88**, 182509 (2006).

[72] D. Depla, S. Mahieu, and J.E. Greene, 44 (n.d.).

[73] P.J. Kelly and R.D. Arnell, Vacuum **56**, 159 (2000).

[74] S. Swann, Phys. Technol. **19**, 67 (1988).

[75] K.S. Harsha, *Principles of Vapor Deposition of Thin Films* (Elsevier, 2005).

[76] M. Yasaka, Rigaku J. **26**, 1 (2010).

[77] T.P. Russell, Mater. Sci. Rep. **5**, 171 (1990).

[78] I.W. Hamley and J.S. Pedersen, J. Appl. Crystallogr. **27**, 29 (1994).

[79] L.G. Parratt, Phys. Rev. **95**, 359 (1954).

[80] S.K. Sinha, E.B. Sirota, S. Garoff, and H.B. Stanley, Phys. Rev. B **38**, 2297 (1988).

[81] M. Björck and G. Andersson, J. Appl. Crystallogr. **40**, 1174 (2007).

[82] J. Bardeen, L.N. Cooper, and J.R. Schrieffer, Phys. Rev. **108**, 1175 (1957).

[83] B.D. Josephson, Phys. Lett. **1**, 251 (1962).

[84] S. Bedanta, Supermagnetism in Magnetic Nanoparticle Systems, 2006.

[85] J. Kerr, Lond. Edinb. Dublin Philos. Mag. J. Sci. **3**, 321 (1877).

[86] R. Schäfer, in *Handb. Magn. Adv. Magn. Mater.*, edited by H. Kronmüller and S. Parkin (John Wiley & Sons, Ltd, Chichester, UK, 2007), p. hmm310.

[87] J. McCord, J. Phys. Appl. Phys. **48**, 333001 (2015).

[88] Qiu, Z. Q., and Samuel D. Bader. "Surface magneto-optic Kerr effect." *Review of Scientific Instruments* 71.3 (2000): 1243-1255.

[89] E.A. Stern, D.E. Sayers, and F.W. Lytle, Phys. Rev. B **11**, 4836 (1975).

[90] J. Vogel and M. Sacchi, J. Electron Spectrosc. Relat. Phenom. **67**, 181 (1994).

[91] R. Nakajima, J. Stöhr, and Y.U. Idzerda, Phys. Rev. B **59**, 6421 (1999).

[92] J. Stöhr, J. Magn. Magn. Mater. **200**, 470 (1999).

[93] B.T. Thole, P. Carra, F. Sette, and G. van der Laan, Phys. Rev. Lett. **68**, 1943 (1992).

[94] C.T. Chen, Y.U. Idzerda, H.-J. Lin, N.V. Smith, G. Meigs, E. Chaban, G.H. Ho, E. Pellegrin, and F. Sette, Phys. Rev. Lett. **75**, 152 (1995).

[95] B.T. Thole, G. van der Laan, J.C. Fuggle, G.A. Sawatzky, R.C. Karnatak, and J.-M. Esteva, Phys. Rev. B **32**, 5107 (1985).

[96] A. Barla, J. Nicolás, D. Cocco, S.M. Valvidares, J. Herrero-Martín, P. Gargiani, J. Moldes, C. Ruget, E. Pellegrin, and S. Ferrer, J. Synchrotron Radiat. **23**, 1507 (2016).

[97] C. Kittel, Phys. Rev. **71**, 270 (1947).

[98] C. Kittel, Phys. Rev. **73**, 155 (1948).

[99] B.B. Singh, S.K. Jena, and S. Bedanta, J. Phys. Appl. Phys. **50**, 345001 (2017).

[100] B. Heinrich, J.F. Cochran, and R. Hasegawa, J. Appl. Phys. **57**, 3690 (1985).

[101] T.-C. Tseng, C. Urban, Y. Wang, R. Otero, S.L. Tait, M. Alcamí, D. Écija, M. Trelka, J.M. Gallego, N. Lin, M. Konuma, U. Starke, A. Nefedov, A. Langner, C. Wöll, M.Á. Herranz, F. Martín, N. Martín, K. Kern, and R. Miranda, Nat. Chem. **2**, 374 (2010).

[102] T. John, J. Hare, and H. Kroto, 4 (n.d.).

[103] V.H. Damle, M. Sinwani, H. Aviv, and Y.R. Tischler, Sensors **20**, 1470 (2020).

[104] S.W. Cho, Y. Yi, J.H. Seo, C.Y. Kim, M. Noh, K.-H. Yoo, K. Jeong, and C.-N. Whang, Synth. Met. **157**, 160 (2007).

[105] S. Mattauch, A. Koutsioubas, U. Rücker, D. Korolkov, V. Fracassi, J. Daemen, R. Schmitz, K. Bussmann, F. Suxdorf, M. Wagener, P. Kämmerling, H. Kleines, L. Fleischhauer-Fuß, M. Bednareck, V. Ossoviy, A. Nebel, P. Stronciwilk, S. Staringer, M. Gödel, A. Richter, H. Kusche, T. Kohnke, A. Ioffe, E. Babcock, Z. Salhi, and T. Bruckel, J. Appl. Crystallogr. **51**, 646 (2018).

[106] P. Carra, B.T. Thole, M. Altarelli, and X. Wang, Phys. Rev. Lett. **70**, 694 (1993).

[107] C.T. Chen, Y.U. Idzerda, H.-J. Lin, N.V. Smith, G. Meigs, E. Chaban, G.H. Ho, E. Pellegrin, and F. Sette, Phys. Rev. Lett. **75**, 152 (1995).

[108] N. Atodiresei, J. Brede, P. Lazić, V. Caciuc, G. Hoffmann, R. Wiesendanger, and S. Blügel, Phys. Rev. Lett. **105**, 066601 (2010).

[109] R. Felici, M. Pedio, F. Borgatti, S. Iannotta, M. Capozi, G. Ciullo, and A. Stierle, Nat. Mater. **4**, 688 (2005).

[110] M. Stengel, A.D. Vita, and A. Baldereschi, Phys. Rev. Lett. **91**, 166101 (2003).

[111] W.W. Pai and C.-L. Hsu, Phys. Rev. B **68**, 121403 (2003).

[112] H.I. Li, K. Pussi, K.J. Hanna, L.-L. Wang, D.D. Johnson, H.-P. Cheng, H. Shin, S. Curtarolo, W. Moritz, J.A. Smerdon, R. McGrath, and R.D. Diehl, Phys. Rev. Lett. **103**, 056101 (2009).

[113] W.W. Pai, C.-L. Hsu, M.C. Lin, K.C. Lin, and T.B. Tang, Phys. Rev. B **69**, 125405 (2004).

[114] W.W. Pai, H.T. Jeng, C.-M. Cheng, C.-H. Lin, X. Xiao, A. Zhao, X. Zhang, G. Xu, X.Q. Shi, M.A. Van Hove, C.-S. Hsue, and K.-D. Tsuei, Phys. Rev. Lett. **104**, 036103 (2010).

[115] Z.-H. Yang, R. Pang, and X.-Q. Shi, J. Phys. Chem. C **119**, 10532 (2015).

[116] K.-D. Tsuei, J.-Y. Yuh, C.-T. Tzeng, R.-Y. Chu, S.-C. Chung, and K.-L. Tsang, Phys. Rev. B **56**, 15412 (1997).

[117] L.-L. Wang and H.-P. Cheng, Phys. Rev. B **69**, 045404 (2004).

[118] A. Tamai, A.P. Seitsonen, F. Baumberger, M. Hengsberger, Z.-X. Shen, T. Greber, and J. Osterwalder, Phys. Rev. B **77**, 075134 (2008).

[119] K.V. Raman and J.S. Moodera, Nature **524**, 42 (2015).

[120] J. Okabayashi, T. Koyama, M. Suzuki, M. Tsujikawa, M. Shirai, and D. Chiba, Sci. Rep. **7**, 46132 (2017).

[121] H. Ebert and S. Man'kovsky, Phys. Rev. Lett. **90**, 077404 (2003).

[122] A. Yaouanc, P.D. de Réotier, and G. van der Laan, Phys. Rev. Lett. **93**, 019701 (2004).

[123] S. Mallik, A.S. Mohd, A. Koutsioubas, S. Mattauch, B. Satpati, T. Brückel, and S. Bedanta, Nanotechnology **30**, 435705 (2019).

[124] D.O. Smith, M.S. Cohen, and G.P. Weiss, J. Appl. Phys. **31**, 1755 (1960).

[125] J.-L. Bubendorff, S. Zabrocki, G. Garreau, S. Hajjar, R. Jaafar, D. Berling, A. Mehdaoui, C. Pirri, and G. Gewinner, EPL Europhys. Lett. **75**, 119 (2006).

[126] N. Chowdhury, S. Mallick, S. Mallik, and S. Bedanta, Thin Solid Films **616**, 328 (2016).

[127] S. Mallick, S. Mallik, B.B. Singh, N. Chowdhury, R. Gieniusz, A. Maziewski, and S. Bedanta, J. Phys. Appl. Phys. **51**, 275003 (2018).

[128] S. Mallik and S. Bedanta, J. Magn. Magn. Mater. **446**, 270 (2018).

[129] S. Mallik, S. Mallick, and S. Bedanta, J. Magn. Magn. Mater. **428**, 50 (2017).

[130] S. Nayak, B.B. Singh, S. Mallick, and S. Bedanta, J. Phys. Appl. Phys. **52**, 305301 (2019).

[131] B.B. Singh, S.K. Jena, and S. Bedanta, J. Phys. Appl. Phys. **50**, 345001 (2017).

[132] A. Conca, S. Keller, L. Mihalceanu, T. Kehagias, G.P. Dimitrakopulos, B. Hillebrands, and E.T. Papaioannou, Phys. Rev. B **93**, 134405 (2016).

[133] S. Pan, T. Seki, K. Takanashi, and A. Barman, Phys. Rev. Appl. **7**, 064012 (2017).

[134] T. Hasegawa and J. Takeya, Sci. Technol. Adv. Mater. (2009).

[135] Z.G. Yu, Phys. Rev. Lett. **106**, 106602 (2011).

[136] V. Podzorov, MRS Bull. **38**, 15 (2013).

[137] I. Biaggio and P. Irkhin, Appl. Phys. Lett. **103**, 243_1 (2013).

[138] B. Verreet, P. Heremans, A. Stesmans, and B.P. Rand, Adv. Mater. **25**, 5504 (2013).

[139] R. Lin, F. Wang, J. Rybicki, M. Wohlgenannt, and K.A. Hutchinson, Phys. Rev. B **81**, 195214 (2010).

[140] *Spectroscopy* **33**, 12 (2018).

[141] O. Idigoras, A.K. Suszka, P. Vavassori, P. Landeros, J.M. Porro, and A. Berger, Phys. Rev. B **84**, 132403 (2011).

[142] N. Chowdhury and S. Bedanta, AIP Adv. **4**, 027104 (2014).

[143] C. Wang, D. Niu, Y. Nie, L. Li, B. Liu, S. Wang, H. Xie, and Y. Gao, J. Phys. Chem. C **125**, 20697 (2021).

[144] N. Nishimura, T. Hirai, A. Koganei, T. Ikeda, K. Okano, Y. Sekiguchi, and Y. Osada, J. Appl. Phys. **91**, 5246 (2002).

[145] S. Mangin, D. Ravelosona, J.A. Katine, M.J. Carey, B.D. Terris, and E.E. Fullerton, Nat. Mater. **5**, 210 (2006).

[146] R. Pang, X. Shi, and M.A. Van Hove, J. Am. Chem. Soc. **138**, 4029 (2016).

[147] Z. Li, W. Mi, and H. Bai, ACS Appl. Mater. Interfaces **10**, 16674 (2018).

[148] S. Mallick, S.S. Mishra, and S. Bedanta, Sci. Rep. **8**, 11648 (2018).

[149] D.A. Dugato, J. Brandão, R.L. Seeger, F. Béron, J.C. Cezar, L.S. Dorneles, and T.J.A. Mori, Appl. Phys. Lett. **115**, 182408 (2019).

[150] E. Fatuzzo, Phys. Rev. **127**, 1999 (1962).

[151] M. Labrune, S. Andrieu, F. Rio, and P. Bernstein, J. Magn. Magn. Mater. **80**, 211 (1989).

[152] A. Adanlété Adjanoh, R. Belhi, J. Vogel, M. Ayadi, and K. Abdelmoula, J. Magn. Magn. Mater. **323**, 504 (2011).

[153] S. Mallick, S. Mallik, and S. Bedanta, J. Appl. Phys. **118**, 083904 (2015).

[154] S. Mallick and S. Bedanta, J. Magn. Magn. Mater. **382**, 158 (2015).

[155] S. Mallick, S.S. Mishra, and S. Bedanta, Sci. Rep. **8**, 11648 (2018).

[156] T. Moorsom, M. Wheeler, T. Mohd Khan, F. Al Ma'Mari, C. Kinane, S. Langridge, D. Ciudad, A. Bedoya-Pinto, L. Hueso, G. Teobaldi, V.K. Lazarov, D. Gilks, G. Burnell, B.J. Hickey, and O. Cespedes, Phys. Rev. B **90**, 125311 (2014).

[157] G. Kresse and J. Furthmüller, Phys. Rev. B **54**, 11169 (1996).

[158] G. Kresse and D. Joubert, Phys. Rev. B **59**, 1758 (1999).

[159] J.P. Perdew, K. Burke, and M. Ernzerhof, Phys. Rev. Lett. **77**, 3865 (1996).

[160] J.E. Hirsch, Phys. Rev. Lett. **83**, 1834 (1999).

[161] S.O. Valenzuela and M. Tinkham, Nature **442**, 176 (2006).

[162] S.A. Wolf, Science **294**, 1488 (2001).

[163] I. Žutić, J. Fabian, and S.D. Sarma, Rev. Mod. Phys. **76**, 323 (2004).

[164] D. Sun, E. Ehrenfreund, and Z. Valy Vardeny, Chem Commun **50**, 1781 (2014).

[165] C. Barraud, P. Seneor, R. Mattana, S. Fusil, K. Bouzehouane, C. Deranlot, P. Graziosi, L. Hueso, I. Bergenti, V. Dediu, F. Petroff, and A. Fert, Nat. Phys. **6**, 615 (2010).

[166] S. Liang, R. Geng, B. Yang, W. Zhao, R. Chandra Subedi, X. Li, X. Han, and T.D. Nguyen, Sci. Rep. **6**, 19461 (2016).

[167] H. Liu, J. Wang, M. Groesbeck, X. Pan, C. Zhang, and Z.V. Vardeny, J. Mater. Chem. C **6**, 3621 (2018).

[168] D. Sun, K.J. van Schooten, M. Kavand, H. Malissa, C. Zhang, M. Groesbeck, C. Boehme, and Z. Valy Vardeny, Nat. Mater. **15**, 863 (2016).

[169] R. Das, V. Kalappattil, R. Geng, H. Luong, M. Pham, T. Nguyen, T. Liu, M. Wu, M.H. Phan, and H. Srikanth, AIP Adv. **8**, 055906 (2018).

[170] H. Liu, J. Wang, A. Chanana, and Z.V. Vardeny, J. Appl. Phys. **125**, 142908 (2019).

[171] V. Kalappattil, R. Geng, R. Das, M. Pham, H. Luong, T. Nguyen, A. Popescu, L.M. Woods, M. Kläui, and H. Srikanth, Mater. Horiz. **7**, 1413 (2020).

[172] R. Iguchi and E. Saitoh, J. Phys. Soc. Jpn. **86**, 011003 (2017).

[173] A. Conca, B. Heinz, M.R. Schweizer, S. Keller, E.Th. Papaioannou, and B. Hillebrands, Phys. Rev. B **95**, 174426 (2017).

[174] K. Ando, S. Takahashi, J. Ieda, Y. Kajiwara, H. Nakayama, T. Yoshino, K. Harii, Y. Fujikawa, M. Matsuo, and S. Maekawa, J. Appl. Phys. **109**, 103913 (2011).

[175] B.B. Singh, S.K. Jena, M. Samanta, K. Biswas, and S. Bedanta, ACS Appl. Mater. Interfaces **12**, 53409 (2020).